Summer 2023

Mitigation of Aeroacoustic Noise of a Fixed Wing Using Passive Flow Control

Cameron L. Perry

MITIGATION OF AEROACOUSTIC NOISE OF A FIXED WING USING PASSIVE FLOW CONTROL

by

CAMERON PERRY

(Under the Direction of Marcel Ilie)

ABSTRACT

As the world becomes more environmentally conscious, noise pollution is of increasing concern. In this study, shallow dimples are applied to a NACA 0012 airfoil at multiple angles of attack (AoA) with the intent of reducing aeroacoustic noise emissions. Both Reynolds Averaged Navier-Stokes (RANS) and Large Eddy Simulation (LES) models are used for aerodynamic and aeroacoustic investigations, respectively, at a fixed Reynolds number of 4.8×10^5. Altering the dimple depth to diameter ratio (d/D) from 2.5% to 15% is first investigated, with a d/D of 5% or lower resulting in the least aerodynamic impact. The transition from shallow dimples to dimpled vortex generators is also found to occur at a 7.5% d/D, as defined by differing flow structures. An aeroacoustic analysis shows a 3.3% d/D ratio is optimal for a 5.71 dB Overall Averaged Sound Pressure Level (OASPL) reduction with a 2.66% average drag increase. A staggered array of dimples with this depth covering the latter 20%, 33% and 50% X/c is then investigated. Far-field noise characteristics are reduced up to 7 dB, with broadband noises below 3000 Hz showing the most improvement. The shallow dimpled array application is found to break up the spanwise coherence, shifting the generated noise towards higher frequencies where it can be more easily dissipated. As such, the application of shallow dimples on the latter portion of an airfoil can be considered a potential candidate for passive noise reduction.

INDEX WORDS: Computational fluid dynamics, Large eddy simulation, Reynolds averaged navier-stokes, Aeroacoustics, Shallow dimples, Passive flow control, Noise reduction methods

MITIGATION OF AEROACOUSTIC NOISE OF A FIXED WING USING PASSIVE FLOW CONTROL

by

CAMERON PERRY

B.S., Georgia Southern University, 2021

M.S., Georgia Southern University, 2023

A Thesis Submitted to the Graduate Faculty of Georgia Southern University

in Partial Fulfillment of the Requirements for the Degree

MASTER OF SCIENCE

ALLEN E. PAULSON COLLEGE OF ENGINEERING AND COMPUTING

MITIGATION OF AEROACOUSTIC NOISE OF A FIXED WING USING PASSIVE FLOW CONTROL

by

CAMERON PERRY

Major Professor:	Marcel Ilie
Committee:	Mosfequr Rahman
	Valentin Soloiu

Electronic Version Approved:

July 2023

DEDICATION

I wish to dedicate this thesis to my parents, Mark, and Patsy Perry, as well as my sister Chelsea Perry for their continued love and support throughout the years.

ACKNOWLEDGMENTS

The research in this thesis was supported by the Department of Mechanical Engineering at Georgia Southern University. I would like to express my sincere appreciation to my research advisor, Dr. Marcel Ilie for the guidance, suggestions, and assistance during my undergraduate and graduate career. Additionally, I would like to thank Dr. Rahman and Dr. Soloiu for their assistance within the laboratory and with the composition of this thesis.

I would also like to thank my fellow graduate students, Eric Pernell, Austin Robbins, John Crowe, Whitney Curwin, David Obando and Charles R Fricks for their support and assistance both in class and in the laboratory.

TABLE OF CONTENTS

Page

LIST OF TABLES

Page

LIST OF FIGURES

Page

NOMENCLATURE

SYMBOLS

c	Chord length (m)
C_d	Drag Coefficient
C_f	Skin Friction Coefficient
C_l	Lift Coefficient
C_p	Pressure Coefficient
c_s	Speed of Sound (m/s)
D	Dimple Diameter (m)
d	Dimple Depth (m)
D_n	Nominal Dimple Diameter (m)
f	Frequency (Hz)
F_r	Froude Number
H	Shape Factor
k	Turbulent Kinetic Energy (J/kg)
L_x	Longitudinal Dimple Distance
L_z	Lateral Dimple Distance
Ma	Mach Number
p	Pressure (Pa)
p_{ref}	Reference Pressure (Pa)
R	Dimple Radius (m)
Re	Chord Reynolds Number
Re_D	Dimple Reynolds Number
U_o	Freestream Velocity (m/s)
v	Kinematic Viscosity (m^2/s)

y	Distance from Wall (m)
δ	Boundary Layer Thickness (m)
δ^*	Displacement Thickness (m)
θ	Momentum Thickness (m)
λ	Wavelength (m)
ρ	Density (kg/m^3)
ω	Turbulent Dissipation Rate (m^2/s^3)

ACRONYMS

AoA	Angle of Attack
AR	Aspect Ratio
BLT	Boundary Layer Trip
CAA	Computations Aeroacoustics
CFD	Computational Fluid Dynamics
DIM	Dimple
DNS	Direct Numerical Simulation
EPA	Environmental Protection Agency
FAA	Federal Aircraft Administration
FW-H	Ffowcs Williams-Hawkings
LES	Large Eddy Simulation
LSB	Laminar Separation Bubble
NACA	National Advisory Committee for Aeronautics
OASPL	Overall Averaged Sound Pressure Level
RANS	Reynolds Averaged Navier-Stokes
RSS	Root-Square-Sum
SPL	Sound Pressure Level
TE	Trailing Edge
TS	Tollmien–Schlichting
UAV	Unmanned Aerial Vehicle
VG	Vortex Generator
WALE	Wall-Adapting Local Eddy

CHAPTER 1

INTRODUCTION

1.1 Purpose of the Study

This study seeks to improve the aeroacoustic characteristics of an airfoil travelling at a low chord Reynolds number while minimizing the aerodynamic impact of said solution. Aeroacoustics is defined as noise generated by turbulent fluids and aerodynamic forces. As both cases are expected to occur during flight, airframe noise must be considered.

Regulation of noise pollution is becoming stricter, preventing residential land use near airports. The Federal Aviation Administration (FAA) requires less than 65 dB for residential and commercial zoning near airports (FAA 2023). Those currently residing near an airport are subjected to continuous noise from the aircraft traveling overhead. Reducing the noise emitted from these aircraft can improve the quality of life for not only those residing near airports, but the passengers onboard. The surrounding environment is also affected, as noise pollution can impact animal behavior, mating, and communication (Kight and Swaddle 2011). As such, the Environmental Protection Agency (EPA) requires less than 52 dB for onshore wind turbine deployment, depending on the emitted frequency and land use (EPA 2020). Thus, a mitigation method is required to reduce noise output for aerospace and wind energy applications.

The impact of low-speed flight characteristics is also a key factor in this study. If an aircraft can produce more lift during takeoff, then it can either take off in a shorter distance or take off with more weight. Reduction in takeoff and landing distances can allow an aircraft to reach a wider range of airports whose runway may otherwise not be suitable for such a large aircraft. Conversely, the ability to fly with a larger payload can increase revenue per flight. A reduction in lift generated, or an increase in drag, will only serve to dissuade the usage of any solution developed to improve the acoustic emissions. An increase in drag requires an increase in engine thrust, which subsequently increases fuel usage and noise emission. Therefore, any developed solution should have minimal negative aerodynamic impact, or ideally improve

both lift and drag. Various devices and methods have been studied to modify boundary layer flow and can be placed into two categories, active and passive (Moghaddam and Neishabouri 2017; Xie et al. 2022). Active devices typically require external energy, reactionary activation, and space within the wing that fuel would otherwise occupy (Fouatih et al. 2016). This reduces vehicle compatibility while increasing costs for development, implementation, and maintenance. Passive devices, on the other hand, are specifically optimized for a particular flight regime and do not require activation.

Dimpled vortex generators are an example of such a device. By creating turbulence, energy from the freestream is pulled into the lower energy boundary layer. As boundary layer flow around airfoils is typically associated with low momentum, the additional energy allows for said flow to stay attached to the surface of the airfoil until the trailing edge. This turbulence, however, increases friction between the air and the surface of the wing, reducing the performance during phases of flight where speeds are higher, and no flow separation is expected. Additionally, this increase in turbulence negatively impacts the aeroacoustics of the aircraft as fluctuations in pressure are created.

1.2 How This Study Is Original

Vortex generators have been extensively studied and have traditionally consisted of triangular or rectangular plates protruding from the surface of the airfoil. This has been shown to increase drag at moderate angles of attack (AoA) and during higher speeds, such as when the aircraft is in level flight or landing (Serdar Genç et al. 2020; Fouatih et al. 2016). Lacking the ability to be turned off, these plate vortex generators have fallen out of favor as a means of increasing a wing's performance. This permanence, however, is precisely why safety is increased with their usage, as the pilot or ground crew are unable to accidentally tamper with the device without the other's knowledge. Dimpled vortex generators maintain this permanence and have been shown to have reducing effects as velocity increases (Xie et al. 2022). This allows for them to be optimized to significantly impact the aeroacoustic performance of the wing during portions of low-speed flight, such as takeoff and landing, while mitigating performance losses during cruise.

Additionally, most commercial aircraft make use of airfoils specifically designed for transonic flights, sacrificing performance at lower speeds. Flaps and slats are typically employed to counter this reduction in performance; however, slats are the main contributor to aeroacoustic noise (Chen et al. 2022; Choudhari and Lockard 2015). Any noise reduction of a wing could later be applied to potentially reduce the noise emissions of these devices.

The more traditional plate vortex generators have seen mild interest in aeroacoustics in recent years; however, these studies have shown contradictory results (Kolkman et al. 2018; Gang, Zhengtao, and Pingguo 2019; Ye et al. 2020). Shallow dimples have been an area of increased focus due to their potential drag reduction (van Campenhout et al. 2018). Shallow dimples have been shown to decrease drag with modest increase in turbulent flow structures due to a steady-state flow pattern over the dimples (Etter 2007; P. R. Spalart et al. 2019). Additionally, little investigation has been conducted at Reynolds numbers above 40,000 for shallow dimples. Being mostly studied on flat plates, their impact at multiple AoAs on airfoils has also been neglected (Panda and Warrior 2021). To the author's knowledge, only one study has been conducted with shallow dimples on an airfoil, as most work has been undertaken to explain their drag reduction mechanism on a flat plate. When applied to an airfoil, however, a drag increase of 1.9% was found (Ananthan et al. 2022). This study was only conducted at an AoA = 0°, however, and with one dimple geometry. There is also very little literature with regard to their aeroacoustic impacts, with (Ananthan et al. 2022) again being the only example found. Due to this, the need to investigate the aerodynamic and aeroacoustic impact of shallow dimples at multiple AoAs and geometries persists.

1.3 Hypothesis and Criteria for Success

If an array of shallow dimples is implemented on the latter portion of an airfoil, then the aeroacoustic emissions of said airfoil can be improved due to the break-up of larger eddies in the turbulent boundary layer. As such, the lower frequencies are theorized to have the greatest reduction. A reduction in acoustics must be economically viable and as such restrictions on a solution must be placed. For the present

case, any increase in drag over 5% will not be considered. The increased engine power required to overcome this drag is inherently counterintuitive to a reduction of noise. This increase in drag also serves as to dissuade any application of shallow dimples, regardless of their noise reduction properties, due to increased fuel usage. Ideally drag should be reduced, as this provides further economic incentive and viability of a shallow dimple solution. A reduction in drag would not only reduce engine noise, but also fuel consumption. Drag, however, is not the primary criteria of success for this thesis. Achieving an Overall Averaged Sound Pressure Level (OASPL) reduction of at least 5 dB is considered for success.

CHAPTER 2

LITERATURE REVIEW

2.1 Influence of Boundary Layer

Flight at low Reynolds numbers is generally defined as a Re < 500,000 and is typically associated with prevailing viscous effects (Perry and Mueller 1987). The operating Reynolds number can be reduced by decreasing chord length, lowering freestream velocity, or reducing fluid density (Perry and Mueller 1986). Low Reynolds number regimes include, but is not limited to, Unmanned Arial Vehicles (UAVs), General Aviation Aircraft, Gliders and Wind Turbines (Xie et al. 2022). Inboard sections of helicopter rotors, propellors or turbine blades may also be subjected to low Reynolds number flow (Perry and Mueller 1986). This viscosity creates a boundary layer around the airfoil, which has a major influence over the aerodynamic performance of said airfoil. As the Reynolds number increases, the viscous effects are less present, and the effects of the boundary layer are less.

Aerodynamic efficiency at a low Reynolds number is critically dependent on maintaining an attached boundary layer. Boundary layer separation phenomena has been predicted to reduce fuel consumption by up to 8%, assuming transition phenomena can be delayed by 50% (Serdar Genç et al. 2020). Separation of the boundary layer occurs in flow that slows down with pressure increasing (J.D. Anderson 2016). This flow against the increasing pressure creates an adverse pressure gradient which can be seen in Figure 2.1.1. Flow separation occurs when the velocity in the boundary layer has reversed direction with respect to the surface of the airfoil (J.D. Anderson 2016; Bappa 2015). As a pressure differential has been created, the higher-pressure air moves towards the lower-pressure air closer to the surface of the airfoil creating turbulence. This creates a pocket or ‘bubble’ of low pressure, low velocity and highly turbulent air known as a Laminar Separation Bubble (LSB). As this air is highly turbulent, the acoustic emissions are increased due to fluctuating pressure. In the LSB, the fluid exerts a constant pressure on the surface, instead of the continually increasing pressure expected of an attached flow (J. Anderson

2017). Flow separation results in a significant increase in pressure drag due to the difference of pressure between the front and rear of the airfoil. In addition to the reduction of aerodynamic performance, reduction in control surface effectiveness and buffeting are also associated with flow separation (Neves et al. 2020). This buffeting can create unwanted vibrations of the structure as well as noise. Additional factors can influence the formation of a LSB, such as wingtip vortices. Ideally a case where the upper and lower flow over an airfoil can only meet at the leading and trailing edges is desired, but such a 2D case is impractical to be implemented.

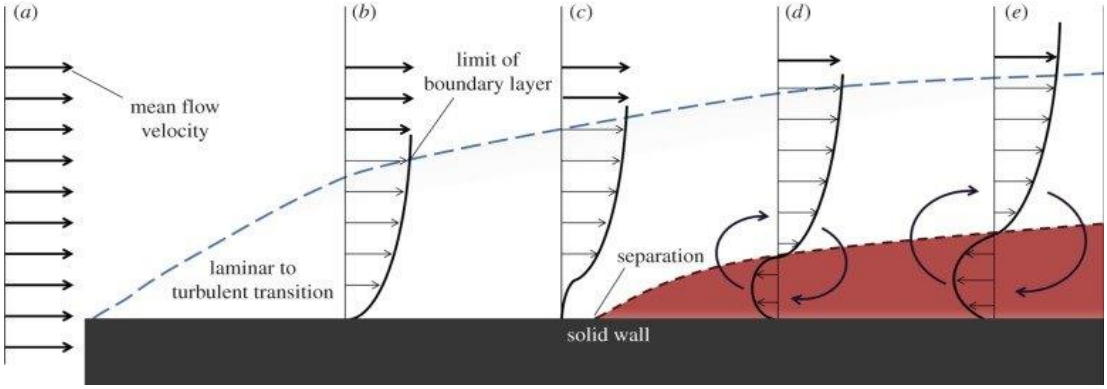

Figure 2.1.1: Stages of Boundary Layer Development on a Flat Plate (Fletcher et al. 2014)

2.1 Types of Flow Control

Control of the boundary layer, or flow control, can be accomplished through a variety of means, each categorized into active and passive flow control. These methods are used primarily to achieve transition delay, drag reduction, lift enhancement, turbulence management, separation postponement, and noise suppression (Jahanmiri 2010). Flow control originated in 1904 with the discovery of the boundary layer by Prandtl and has been studied extensively since the Second World War (Panaras and Lu 2015; Prandtl 1928). Significant emphasis has been placed on active flow control in past years, in which energy is introduced into the boundary layer from an external source (Tousi, Bergadà, and Mellibovsky 2022; Tousi et al. 2021). This requires energy input to an actuator and is continuously adjusted based on some

form of measurement or sensor (Jahanmiri 2010). This necessitates complex solutions reducing vehicle compatibility and device reliability. Although the devices can be turned off when not necessary, such as during a low AoA flight regime, the reduction in usable internal wing volume, mechanical or electrical complexity and safety criteria has led to a resurgence in passive flow control techniques.

Passive flow control devices, by contrast, are the least expensive, least complex, and quickest devices to design and manufacture (Fouatih et al. 2016). Devices of this nature do not require external energy input, allowing for a wider range of compatible vehicles. The effectiveness of passive flow control devices must be specifically tailored to a particular fluid flow condition, however, and if exposed to unexpected conditions a passive flow control device will induce drag penalties (Zhu et al. 2022). Therefore, design optimization has been of critical concern in recent years to widen the operational Reynolds number range such devices can operate at (Serdar GenÇ, Koca, and AÇIkel 2019).

2.2 Vortex Generators

The primary and most common form of passive flow control is conducted by Vortex Generators (VGs). These are traditionally small rectangular or triangular plates arranged perpendicular to the surface of the airfoil and immersed within the boundary layer (Lu et al. 2011; De Tavernier et al. 2021). The geometry of VGs has been extensively studied and culminated in arrangements like that seen in Figure 2.2.1. These plates are placed upstream or at the separation point for optimal efficacy (Fouatih et al. 2016). Pairs of VGs are placed in spanwise rows and given a yaw angle (β) with respect to the oncoming flow. The authors in (Mai et al. 2008) assumed that these vortex generators created chordwise vortices that disrupted the formation of larger stall vortices. Another subsequent study of leading-edge plate vortex generators confirmed this assumption (Heine et al. 2009). Similarly, the authors in (Daniel Baldacchino et al. 2018) concluded that by pulling energy from the freestream, these chordwise vortices re-energize the boundary layer allowing for a delayed flow separation. This, however, results in VGs performing differently in various flow conditions, and a design must be optimized for where flow separation is likely to occur at a

given flight regime (Zhu et al. 2019). Typically, this consists of a yaw angle of $10° < \beta < 15°$, and a height determined by the thickness of the boundary layer. Consequently, the increase in frictional drag at low AoAs, caused by the induced vortices, has resulted in VGs reducing in height from the thickness of the boundary layer to only a portion of it (Fouatih et al. 2016).

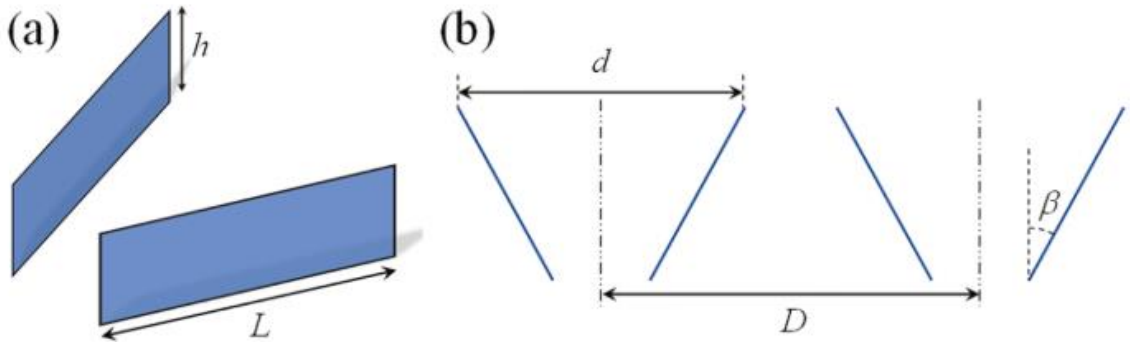

Figure 2.2.1: Geometry of a Rectangular Plate Type Vortex Generator (Zhu et al. 2022)

2.3 Dimpled Vortex Generators

Without the constraint of retrofitting existing aircraft or structures, a dimpled vortex generator like that seen in Figure 2.3.1 could be considered. Like that of a golf ball and plate VGs, a dimpled vortex generator disturbs the boundary layer by transferring energy from the freestream to the surface. The resultant turbulence delays flow separation, and decreases pressure drag (Ramprasadh and Devanandh 2015). When given the same initial velocity, a dimpled golf ball will fly further than a smooth ball for this reason (Soundharya et al. 2016). Implementation of multiple dimples along the upper and lower surfaces was investigated, which yielded similar lift regardless of the number of dimples (Soundharya et al. 2016). The authors in (D'Alessandro et al. 2019) demonstrated that the implementation of dimples produces a reduction of the LSB extension if the dimples are placed before or inside the LSB. When placed after the separation bubble, only reattachment was affected (D'Alessandro et al. 2019). A drag reduction of up to 43% and a lift-to-drag ratio improvement of up to 337% can be achieved when implementing an 8% chord

diameter dimple at 25% of the chord (Xie et al. 2022). Dimpled VGs also have reduced drag at higher Reynolds numbers when compared to traditional plate VGs as the reduced viscous effects cause flow separation over the dimple (Xie et al. 2022). As the flow does not effectively enter the dimple, counter-rotating vortices are unable to form within it, and little energy is transferred from the freestream into the boundary layer. As such, the Reynolds number is an important criteria for dimple VG design.

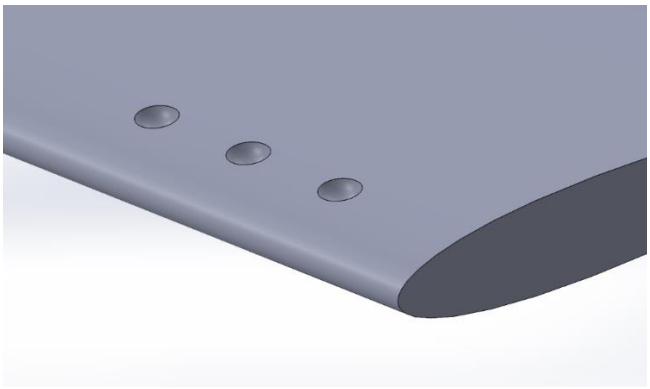

Figure 2.3.1: Leading Edge Dimpled Vortex Generators on a NACA 0012 Airfoil

2.4 Shallow Dimples

Shallow dimples refer to a dimple with a depth to diameter (d/D) ratio less than 10% in accordance with the suggestions of Veldhuis and Vervoort (Veldhuis and Vervoort 2009). Applications with shallow dimples have been successfully shown to reduce drag, with the converge/diverge, visualized in Figure *2.4.1*, effect being the most cited cause (van Nesselrooij et al. 2016; P. R. Spalart et al. 2019; C.M. Tay 2011; C.M.J. Tay, Khoo, and Chew 2015). When continuing the work from previous studies, the authors in (C.M. Tay 2011) described 6 flow structures for spherical dimples of different depths. Deeper dimples, d/D > 20%, were prone to Tornado-like vortices, both symmetric and asymmetric, and counter-rotating vortices which did not result in a drag reduction. Similarly, a d/D > 10% showed counter-rotating vortices within the dimple (C.M.J. Tay, Khoo, and Chew 2015). This difference in flow structure, converge/diverge versus vorticity formation, is what defines the difference between shallow dimples and dimpled vortex generators (C.M. Tay 2011).

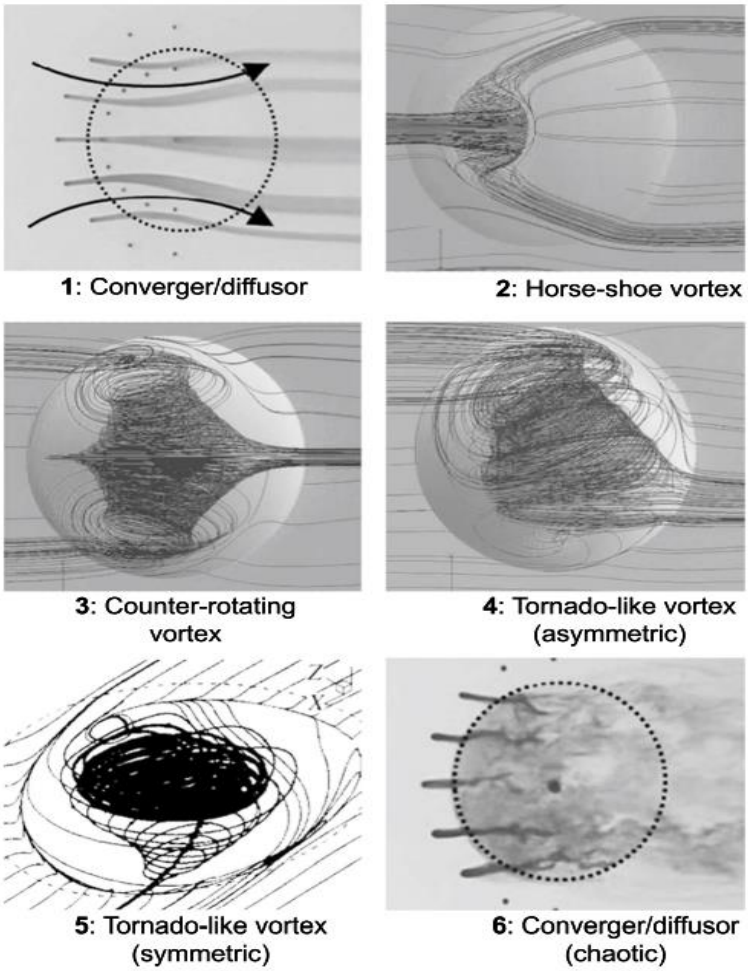

Figure 2.4.1: Comparison of Flow Structures Across Dimples (van Nesselrooij et al. 2016)

Most notably, the authors in (van Nesselrooij et al. 2016) showed a drag reduction with shallow dimples for aerodynamic purposes, with the premise of inducing a spanwise shear force in the near-wall flow. This is typically accomplished through oscillating the wall itself, electromagnetic fluid or using microscopic riblets (Du, Symeonidis, and Karniadakis 2002; Yakeno, Hasegawa, and Kasagi 2014). The primary benefits cited for shallow dimples when compared to these other methods is a smooth surface not prone to wear and dirt accumulation, resulting in an elegant solution for turbulent drag reduction (Dean and Bhushan 2010; Panda and Warrior 2021; van Campenhout et al. 2018). The underlying mechanism, however, for drag reduction is not fully understood, and as such several studies fail to achieve drag reduction (Lienhart, Breuer, and Köksoy 2008; P. R. Spalart et al. 2019; van Campenhout et al. 2018).

Increasing the surface coverage of the dimples, however, has been shown to improve drag (C.M. Tay 2011; C.M.J. Tay, Khoo, and Chew 2015). Additionally, an aligned and staggered array was found to reduce drag by 2.5% and 5%, respectively (Veldhuis and Vervoort 2009). This has culminated in the geometry seen in Figure 2.4.2 which has been extensively studied for heat transfer purposes.

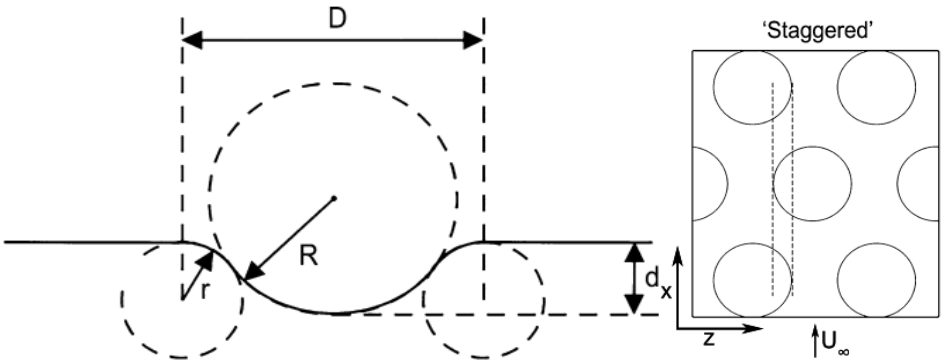

Figure 2.4.2: Cross-sectional and Streamwise Geometry of Shallow Spherical Dimples (Silvani 2021)

From Figure 2.4.2, an empirical relation can be established for important parameters such as:

$$R = \frac{d}{2} + \frac{D_n^2}{8d} \qquad 2.4.1$$

where D_n is the nominal diameter dimple (Silvani 2021). This measures the distance between the two points where the sphere intersects the horizontal plane, i.e., how 'wide' the dimple is. Conversely, the following relation is also of importance:

$$\frac{D}{2} = \sqrt{d(2R + 2r - d)} \qquad 2.4.2$$

where *D* is the dimple diameter, *d* is the dimple depth, and *r* is the dimple fillet radius (Silvani 2021).

Following these relations, a drag reduction of 4% on a flat plate was found when shallow dimples were implemented (van Nesselrooij et al. 2016). A follow up paper by the same group could not replicate these results, however, when attempting to observe the flow structure of the dimple (van Campenhout et al. 2018). This was reasoned to be due to the negative pressure gradient suppressing the growth of coherent structures and rendering the drag reduction mechanism ineffective (van Campenhout et al. 2018). Spanwise

oscillations were still observed as high as $\frac{y}{\delta} = 20\%$, supporting the spanwise shear drag reduction theory previously mentioned. In addition to this, the authors in (C.M.J. Tay, Khoo, and Chew 2015) independently proposed a similar spanwise shear drag reduction theory, though the underlying drag reduction mechanism is still debated. A validation study was also attempted to replicate the drag reduction, both experimentally and numerically (P. R. Spalart et al. 2019; van Nesselrooij et al. 2016). A drag increase of 1% was reported in both cases, without explanation for the contradiction after no flaws were identified between the two works (P. R. Spalart et al. 2019). Furthermore, applying shallow dimples to a symmetric NACA 0012 airfoil was shown to increase drag by 1.8%, though this application was only on the latter 18% of the chord (Ananthan et al. 2022). As such, there is little literature for the application of shallow dimples for aerospace purposes, and explanations for their potential drag reduction mechanisms on an airfoil.

2.5 Numerical Simulation of Passive Flow Control

Simulations are commonly used to investigate passive flow control and typically employ the Reynolds Averaged Navier-Stokes (RANS) method (D Baldacchino et al. 2016). Some numerical studies have been based on the more computationally expensive Direct Numerical Simulation (DNS) and Large Eddy Simulation (LES) methods (P.R. Spalart et al. 2015; Chan and Chin 2021). Several studies have proven the effectiveness of a RANS method, however, as a means to reduce computational expense (Manolesos, Papadakis, and Voutsinas 2020). Therefore, RANS simulations are most commonly used in predicting flow involving passive flow control (Zhu et al. 2019). It is of note, however, that RANS methods require a very fine mesh of the boundary layer to maintain accuracy (Zhu et al. 2021). RANS was effective even when including blade vortex interaction of a rotating wind turbine (Zhu et al. 2021). Alternatively, the Bender-Anderson-Yagle (BAY) model may be used, though the weaker streamwise vortices reduce the benefits of the lower computational requirements (Manolesos, Papadakis, and Voutsinas 2020). Therefore, due to computational requirements, RANS simulations remain the standard for passive flow control simulation.

2.6 Aeroacoustic Effects of Airfoils

Tonal noise is the dominant component of the noise spectra generated by an airfoil while subjected to fluid flow (Arcondoulis et al. 2019). This is commonly associated with low Reynolds number flows, below Re = 500,000, and must be considered due to human ears being highly sensitive to tonal noise (Cao et al. 2022; Schumacher, Doolan, and Kelso 2014). As the viscous effects are prevalent at these low Reynolds number, the acoustic frequency can be assumed proportional to the boundary layer thickness using Equation 2.6.1:

$$f = \frac{U_o}{\lambda} \qquad 2.6.1$$

where the acoustic wavelength of the turbulent boundary layer is roughly proportional to the boundary layer thickness, $\lambda \sim \delta$, and U_o is the freestream velocity (Kolkman et al. 2018).

In addition to the Reynolds number, AoA and airfoil profile contribute significantly to tonal noise generation (Cao et al. 2022). A correlation between the laminar separation bubble and Tollmien-Schlichting (TS) waves was demonstrated by the authors in (Lowson, Fiddes, and Nash 1994), seen in Figure 2.6.1. In the region where tonal noise was detected, though there was no conclusion on the generation mechanism of the tonal waves (Lowson, Fiddes, and Nash 1994). TS waves are a common method by which laminar boundary layers transition to turbulence. Initiated by a disturbance, typically leading-edge roughness these waves grow while still laminar resulting in three-dimensional velocity and pressure fluctuations (Gersten 1985). Commonly, a boundary layer trip (BLT) is used to force a disturbance, and transition from laminar to turbulent flow (Nagy, Delfs, and Bennett 2022). This develops into three-dimensional unstable waves which begin to break down. Intense local turbulent fluctuations then occur, furthering the transition to a turbulent boundary layer (Reed 1981).

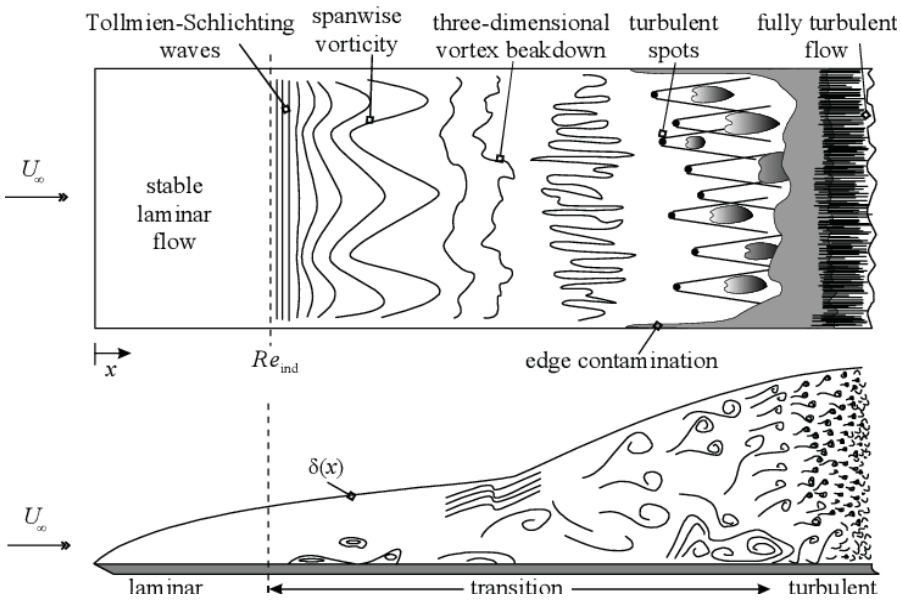

Figure 2.6.1: Tollmien-Schlichting Wave Formation for a Turbulent Boundary Layer (Simon 2017)

The formation of TS waves was found to occur at a lower Reynolds number than the appearance of tonal noise, indicating an instable boundary layer is not sufficient for tonal noise to occur (Lowson, Fiddes, and Nash 1994). This study observed no tonal noise when a reversed flow region is present, further confirming the lack of correlation between boundary layer stability and tonal noise generation (Nash, Lowso, and McAlpine 1999). Conversely the authors in (Paterson et al. 1973) proposed vortices at the trailing edge were the cause of tonal noise. It was determined that laminar flow was needed on the pressure side of the airfoil for tonal noise to occur. A Particle Image Velocimetry (PIV) concluded the frequency of vortex shedding is consistent with the frequency of the dominant tonal noise while discrete noise was associated with periodic amplitude modulation (Pröbsting, Serpieri, and Scarano 2014). This confirms Paterson's suspicions on the formation of the dominant trailing edge acoustic waves resulting in Equation 2.6.2 for acoustic wave generation:

$$f_s = \frac{0.011{U_o}^{3/2}}{(cv)^{1/2}} \qquad 2.6.2$$

where c is the chord length, v is the kinematic viscosity, and U_o is freestream velocity (Paterson et al. 1973). Tam suggested a feedback loop which causes multiple high amplitude tones (Tam 1974). This was by (Arbey and Bataile 1983), suggesting that acoustic waves were generated near the trailing edge and propagated upstream towards the TS wave formation location (Arbey and Bataile 1983). If the two waves became aligned and in phase, the TS waves would be amplified, which would amplify the acoustic waves.

Interest in aeroacoustics has shifted to finite length airfoils to better represent a realistic application. One such study was concerned with a NACA 0012 airfoil with aspect ratios (ratio of span width to cord length) of 1, 1.33, 2, 3, and 6 (Brooks and Marcolini 1986). It is important to note that in this study the tips were rounded. By applying a rough grit on the airfoil surface, the turbulent boundary layer transition was forced and tonal noise was eliminated (Brooks and Marcolini 1986). A numerical and experimental analysis of a squared tip wing with an aspect ratio of 3.33 was also conducted with no BLT, allowing tonal noise to be generated (Mathias, Pye, and Cantwell 1998). It was not until the authors in (D.J. Moreau et al. 2014) that an extensive wall mounted finite airfoil was extensively studied for tonal noise. A NACA 0012 airfoil with aspect ratios between 0.2 and 2 were evaluated with no tip rounding. It was observed that the finite length significantly affects the formation of tonal noise due to the wall junction and tip vortices (D.J. Moreau et al. 2014). A similar study on a Clark-Y airfoil was also conducted, concluding that the rounding of the tip has a significant impact on the tonal noise frequency (Klei, Buffo, and Stumf 2014). In a follow up study, it was determined that the camber of an airfoil shifts the tonal noise production due to delayed flow separation (D. Moreau et al. 2017; D.J. Moreau and Doolan 2016). As airfoil aspect ratio increases, its behavior begins to resemble that of an infinite airfoil, or 2D airfoil. The thickness of an airfoil is also of concern due to earlier flow separation, and has a strong impact on the characteristics and generation of tonal noise (Geyer and Moreau 2021).

The turbulent length scale for trailing edge noise is equal to the boundary layer displacement thickness (Oerlemans et al. 2009). As such, the ratio of freestream velocity to wavelength is roughly equal to the frequency at which disturbances occur. If the eddies are larger than the chord then the airfoil is considered compact, while eddies smaller than the chord result in a non-compact airfoil. When the airfoil

acoustically compacts the eddies, a fluctuating force on the complete airfoil results in low frequency emission (Oerlemans et al. 2009). For non-compact airfoils, sound production is proportionate to Ma^2 which causes an increase in acoustic efficiency at higher frequencies (Blake 2017). The directivity pattern for this is seen in Figure 2.6.2 on the right, where the maximum acoustic emission is upstream of the airfoil. For trailing edge noise, the transition from compact to non-compact occurs at low subsonic speeds as the turbulent length scale is in the order of the displacement thickness (Blake 2017). Displacement thickness is significantly smaller than the chord, causing trailing edge behavior to be both compact and non-compact.

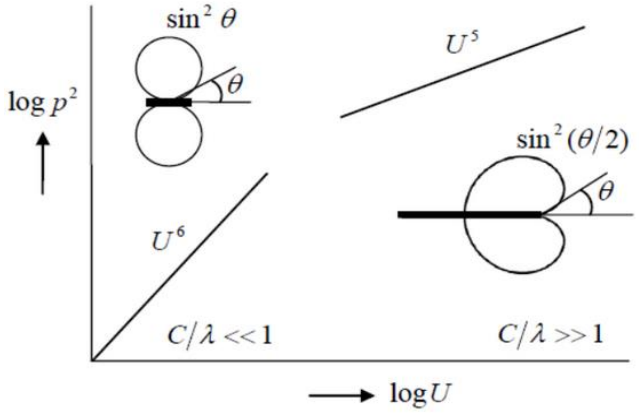

Figure 2.6.2: Directivity Pattern for Airfoil Noise (Blake 2017)

2.7 Aeroacoustic Effects of Flow Control Devices

The aforementioned studies were primarily concerned with the aeroacoustic effects of clean symmetrical airfoils, NACA 0012 and NACA 0018, due to their well-known aerodynamic characteristics. In practice, these airfoils are typically augmented with high lift or flow control devices which contribute significantly to airframe noise along with extended landing gear (Chen et al. 2022; Fink and Bailey 1980). Understanding the impact these devices have on aeroacoustics is of equal importance. The primary contributor to airframe noise on commercial aircraft has been identified as slats (Dobrzynski 2010). A three element 30P30N airfoil was studied, which found pressure amplitude fluctuations scaled well with freestream dynamic pressure (Pascioni and Cattafesta 2014). These fluctuations were propagated as four

prominent frequency peaks, suggesting there are more appropriate scaling parameters. The amplitude of these peaks decreased as the AoA increased. This study, however, assumed an idealized geometry which neglected the slat tracks connecting the slats to the main wing. This was remedied in an acoustic field study, where the slat track was shown to have an amplification effect on the high-pressure fluctuation, increasing low frequency broadband noise (Chen et al. 2022). A spiral vortex pair between the slat and main wing was determined as the most critical flow structure, as it influences the main wing.

From 1975 onwards, serrated edge extensions have been extensively studied as a method to reduce airframe noise (Fink and Bailey 1980). One of the first studies concerned with trailing edge noise found that noise scales with velocity raised between the fourth and fifth power (Powell 1964). The development of a numerical prediction for the noise reduction caused by trailing edge serrations was undertaken by the authors in (Mayer et al. 2019), where the accuracy of the simulation was highly dependent on the boundary layer information provided to the solver. The authors in (Cao et al. 2020) assumed that the vortex promoted sufficient mixing of the converging fluid from the pressure and suction sides of the airfoil. These counter-rotating vortices were caused by the trailing edge serrations and reduced low to mid frequency noises (Cao et al. 2020).

Porous materials have also been studied as a method of mitigating acoustic propagation. Covering a cylinder in a porous material was shown to reduce noise by up to 17 dB (Li et al. 2020). Porous inserts were installed on the trailing edge of a NACA 0018 by yielding an 11 dB noise attenuation (Rubio Carpio et al. 2019). A similar study applied porosity across the leading edge of an airfoil, downstream of the leading edge and across the entire chord (Chaitanya et al. 2020). Porous leading edges were shown to reduce noise, though a similar effect was achieved using a spanwise row of holes downstream of the leading edge. These porous materials, however, can be easily clogged with dirt or ice which mitigates their noise reduction effects (Panda and Warrior 2021).

Aeroacoustic effects of vortex generators, however, has received little attention. Wind turbines is susceptible to flow separation, and conversely noise, as thicker airfoils are used to increase structural strength. VGs, however, significantly increase radiated noise by as much as 10 dB (Kolkman et al. 2018).

It was determined that in frequencies below 4,000 Hz, the trailing edge noise was dominant (Kolkman et al. 2018). At frequencies above 6,350 Hz, the prominent noise source is the vortex generators, with the transition between the two sources occurring between the two respective frequencies (Kolkman et al. 2018). Another study, however, found a decrease, 24 dB, in maximum noise when VGs were implemented (Gang, Zhengtao, and Pingguo 2019). In the range of highest sensitivity for human hearing, 2,000-5,000 Hz, sound pressure drops by almost 20 dB. This was reasoned to be caused by VGs promoting mass and energy exchange between the freestream and boundary layer which delays flow separation (Gang, Zhengtao, and Pingguo 2019). This reduces trailing edge turbulence and subsequently the trailing edge noise. Another study simulated and compared full-scale two blade wind turbine to experimental results with good agreement (Ye et al. 2020). When VGs were installed, however, trivial difference was found in the noise levels when compared to no VGs (Ye et al. 2020). Vortex generators have also been studied in other instances of noise reduction. The installation of VGs on the suction side of a flap has also been investigated, which reduced flap side-edge noise by 1.5 dB (Murayama et al. 2017). This shows that a flow control device can be implemented to reduce the noise emission of another flow control device.

From these studies, it can be concluded that the aeroacoustic effects of VGs on an airfoil are not well understood as contradictory results are published. The aeroacoustic effects of dimpled VGs have been neglected as well, with little literature on the subject. Subsequently, little literature is available for shallow dimples and their acoustics. One study has been conducted by the authors in (Ananthan et al. 2022), where shallow dimples were applied on the latter 18% of a NACA 0012. Although drag was increased by 1.8%, the trailing edge noise emissions were reduced by 5.5 dB. Upstream, however, an increase of 3.5 dB was observed. This case was only conducted at an AoA = 0° with a single dimple array. As such, the varying of dimple geometry is theorized to have significant alteration to the noise emission characteristics.

CHAPTER 3

METHODOLOGY

To assess the impact of shallow dimples, a combined numerical approach is used. A Computational Fluid Dynamics (CFD) solver is used to initially determine aerodynamic effects of certain geometry, which is later assessed with Computational Aeroacoustics (CAA). This approach reduces the expense of conducting physical experiments. The software used for CFD is ANSYS Fluent, with meshing conducted in ANSYS Meshing and all modelling done in SolidWorks and ANSYS Design Modeler. Aeroacoustic data is not able to be measured experimentally due to a lack of an experimental anechoic chamber. In wind tunnels that are not acoustically treated, the test section background noise is typically dominated by broadband fan noise in addition to tonal noise sources consisting of: fan blade passing frequency, fan blade/stator-interaction, electromagnetic motor noise, vortex shedding noise from flow over probes or support wires, self-noise from flow over perforated metal on collector flaps, and low frequency resonance associated with flow interactions of an open jet nozzle, collector, and the wind tunnel circuit (Duell et al. 2004). The current location of the wind tunnel at Georgia Southern University is not well suited to acoustic tests, nor are the physical restrictions of said wind tunnel conducive to acoustic modification. Typically, large wind tunnels are desired for aeroacoustic research (Duell et al. 2002). Also, the inability to match the Reynolds number of experimental and numerical testing would limit the effectiveness of an experimental validation study. Due to this, a purely numerical study is conducted, with validation conducted against literature ensuring the accuracy of the data gathered.

3.1 Non-Dimensional Parameters

In aerodynamic and aeroacoustic research, non-dimensional parameters are a useful tool in analyzing and comparing results. Of primary importance is the Reynolds number, which compares the similarity of two flows via the ratio of inertial forces over viscous forces. At lower Reynolds numbers, the

viscous forces dominate resulting in a laminar flow. Conversely, the viscous effects will become reduced as the Reynolds number is increased, resulting in a turbulent flow regime. The formulation for chord Reynolds number of an airfoil, assuming negligible compressibility, can be written as:

$$Re = \frac{U_0 l}{v} \qquad 3.1.1$$

where U_0 is the freestream velocity, l is the chord length of the airfoil and v is the kinematic viscosity of the fluid. Reynolds numbers for the dimples are also of importance as this can be used as a normalized term for describing fluid flow across them. This is written in a similar form with only the length being changed to dimple diameter (D):

$$Re_D = \frac{U_0 D}{v} \qquad 3.1.2$$

Mach number is important for characterizing compressible flow and is expressed as the ratio of local velocity to the speed of sound as follows:

$$Ma = \frac{u}{c_s} \qquad 3.1.3$$

Lastly, the y^+ value is a non-dimensional distance based on the local cell fluid velocity and is associated with the resolution of a mesh. As such it is a representation of the dimensionless distance from the surface of a wall to the first node in the mesh. This value can be estimated by:

$$y^+ = \frac{u_* y}{v} \qquad 3.1.4$$

where u_* is the friction velocity at the wall and y is the distance from the wall to the nearest node.

3.2 Conservation Equations

All CFD and CAA equations are obtained directly from the ANSYS Fluent Theory Guide (ANSYS 2011). As aeroacoustic noise requires a fluid-structure interaction, the turbulent boundary layer and subsequent aerodynamic forces should be accurately modeled. As such, the boundary layer around an airfoil should be highly resolved to accurately solve velocity and pressure on and around the surface. Various methods of CFD have been used to predict these gradients, but the two prominent standouts, and the two of current interest, are RANS and LES. The RANS simulations are used for preliminary investigation and aerodynamic investigation as they require significantly less computational resources than a comparable LES investigation (Tousi et al. 2021). These initial results can then be used to initialize the subsequent LES simulations to further reduce computational demands. For both LES and RANS, the governing equations for mass, momentum and energy are used (ANSYS 2011). The equation for conservation of mass can be written as:

$$\frac{\partial \rho}{\partial t} + \nabla \cdot (\rho \vec{v}) = S_m \qquad 3.2.1$$

and is valid for incompressible and compressible flows. The source term S_m is the mass added to the continuity, typically due to vaporization or user-defined sources (ANSYS 2011). Conservation of momentum is also described as follows:

$$\frac{\partial}{\partial t}(\rho \vec{v}) + \nabla \cdot (\rho \vec{v} \vec{v}) = -\nabla p + \rho \vec{g} + \vec{F} \qquad 3.2.2$$

where p is the local static pressure and $\rho\ \vec{g}$ and $\vec{F}$ are body forces (ANSYS 2011). Finally, the conservation of energy is described as the following:

$$\frac{\partial}{\partial t}(\rho E) + \nabla \cdot \left(\vec{v}(\rho E + p)\right) = -\nabla \cdot \left(\sum_j h_j J_j\right) + S_h \qquad 3.2.3$$

with $\bar{\bar{\tau}}$ being the shear stress tensor (ANSYS 2011). For compressible flows, the same continuity and momentum equations are used. The energy equation solved by Fluent incorporates the coupling between

flow velocity and temperature (ANSYS 2011). Compressible flows are typically characterized by the total pressure and temperature and as such the following ideal gas law can be used:

$$\rho = \frac{p_{op} + p}{\frac{R}{M_W T}} \qquad 3.2.4$$

where p_{op} is the operating pressure as defined by the user, R is the universal gas constant and M_W is the molecular weight (ANSYS 2011). From this the temperature, T, can be solved by using the energy equation.

3.3 Steady-State Computational Fluid Dynamics

Time averaged flow is based on the RANS equations, and there is a variety of different turbulence models available in ANSYS Fluent. Two-equation turbulence models are exceedingly popular, with k-ε and k-ω being the most popular where k is the turbulent kinetic energy, ε is the turbulent dissipation and ω is the turbulence dissipation rate. The k-ω SST model employed by ANSYS Fluent was developed in 1994 and combines the near-wall robust and accurate k-ω formulation with the superior freestream independence of the k-ε model (Menter 1994; ANSYS 2011). While having a similar form to the standard k-ω model, the k-ω SST model can be expressed by the following two equations:

$$\frac{\partial}{\partial t}(\rho k) + \frac{\partial}{\partial x_j}(\rho k u_j) = \frac{\partial}{\partial x_j}\left(\Gamma_k \frac{\partial k}{\partial x_j}\right) + G_k - Y_k + S_k \qquad 3.3.1$$

$$\frac{\partial}{\partial t}(\rho \omega) + \frac{\partial}{\partial x_j}(\rho \omega u_j) = \frac{\partial}{\partial x_j}\left(\Gamma_\omega \frac{\partial \omega}{\partial x_j}\right) + G_\omega - Y_\omega + D_\omega + S_\omega \qquad 3.3.2$$

where G_k and G_ω is the generation of k and ω in a manner consistent with the Boussinesq hypothesis as described in the standard k-ω model, Y_k and Y_ω represent the dissipation of k and ω due to turbulence, S_k and S_ω are user-defined source terms, and D_ω is the cross-diffusion term (ANSYS 2011). S is the mean rate-of-strain tensor described in the same way as the $k - \varepsilon$ model:

$$G_k = \mu_t S^2 \qquad 3.3.3$$

$$G_\omega = \alpha \frac{\omega}{k} G_k \quad 3.3.4$$

$$S = \sqrt{2 S_{ij} S_{ij}} \quad 3.3.5$$

and Γ_ω and Γ_k is the effective diffusivity of ω and *k* respectively and are given by:

$$\Gamma_\omega = \mu + \frac{\mu_t}{\sigma_\omega} \quad 3.3.6$$

$$\Gamma_k = \mu + \frac{\mu_t}{\sigma_k} \quad 3.3.7$$

where the turbulent viscosity μ_t can be found by (ANSYS 2011):

$$\mu_t = \frac{\rho k}{\omega} \frac{1}{\max\left[\frac{1}{a^*}, \frac{S F_2}{a_\omega}\right]} \quad 3.3.8$$

The turbulent Prandtl numbers for *k* and ω can be computed by the following:

$$\sigma_k = \frac{1}{F_1/\sigma_{\omega,1} + (1 - F_1)/\sigma_{\omega,2}} \quad 3.3.9$$

$$\sigma_\omega = \frac{1}{F_1/\sigma_{\omega,1} + (1 - F_1)/\sigma_{\omega,2}} \quad 3.3.10$$

which can be further broken down into the blending functions F_1 and F_2:

$$F_1 = \tanh\left(\Phi_1{}^4\right) \quad 3.3.11$$

$$\Phi_1 = \min\left[\max\left(\frac{\sqrt{k}}{0.09\omega y}, \frac{500\mu}{\rho y^2 \omega}\right), \frac{4\rho k}{\sigma_{\omega,2} D_\omega^+ y^2}\right] \quad 3.3.12$$

$$D_\omega^+ = \max\left[2\rho \frac{1}{\sigma_{\omega,2}} \frac{1}{\omega} \frac{\partial k}{\partial x_j} \frac{\partial \omega}{\partial x_j}, 10^{-10}\right] \quad 3.3.13$$

$$F_2 = \tanh\left(\Phi_2{}^2\right) \quad 3.3.14$$

$$\Phi_2 = \max\left[\left(\frac{\sqrt{k}}{0.09\omega y}, \frac{500\mu}{\rho y^2 \omega}\right)\right] \quad 3.3.15$$

where *y* is the distance to the next surface and D_{ω}^{+} is the positive portion of the cross-diffusion term (ANSYS 2011).

3.4 Transient Computational Fluid Dynamics

Turbulent flow can have eddies with a wide range of length and time scales. Directly solving these is called Direct Numerical Simulation (DNS) and is not computationally practical as the range of eddies scales is proportional with the cube of the Reynolds number (ANSYS 2011). This necessitates a drastic increase in element count as the Reynolds number is increased, limiting the practical implementation of DNS. In cases where a high Reynolds number flow is expected, the larger eddies can be directly resolved while eddies of a smaller scale than the mesh grid are modeled. Larger eddies are more dependent on the flow conditions and geometry, often greatly influencing the flow by transporting most of the mass, momentum, and energy (ANSYS 2011). Smaller eddies are less dependent on flow conditions and as such are more isotropic. Neglecting to directly solve for them can reduce computational requirements and LES filters out these smaller eddies. The requirement for a finer mesh persists when compared to RANS, though not to the same extent as DNS (Hattori, Umehara, and Nagano 2013). Additionally, longer simulation run times are required to allow the flow to fully develop.

The filtering results in subgrid-scale stresses, which should be accounted for (ANSYS 2011). For this, the Boussinesq hypothesis is used, computing the deviatoric term of the subgrid-scale turbulent stresses for compressible fluids from the following:

$$\tau_{ij} - \frac{1}{3}\tau_{kk}\delta_{ij} = -2\mu_t \bar{S}_{ij} = -2\mu_t \left(S_{ij} - \frac{1}{3}S_{kk}\delta_{ij}\right) \qquad 3.4.1$$

where μ_t is the turbulent viscosity (ANSYS 2011). The isotropic stresses are added to static pressure, and $\bar{S}_{ij}$ is the rate-of-strain tensor defined by:

$$\bar{S}_{ij} = \frac{1}{2}\left(\frac{\partial \bar{u}_i}{\partial x_j} + \frac{\partial \bar{u}_j}{\partial x_j}\right) \qquad 3.4.2$$

A density-weighted filtering operator is introduced when compressible flows are required:

$$\widetilde{\Phi} = \frac{\overline{\rho\Phi}}{\bar{\rho}} \qquad 3.4.3$$

In the same form as Equation *3.4.1*, the Favre Filtered Navier Stokes equation results in a split stress tensor of:

$$\tau_{ij} = \tau_{ij} - \frac{1}{3}\tau_{kk}\delta_{ij} + \frac{1}{3}\tau_{kk}\delta_{ij} \qquad 3.4.4$$

which is split into a deviatoric and isotropic term (ANSYS 2011). Turbulent viscosity is solved for by the Wall-Adapting Local Eddy-Viscosity (WALE) model, and the eddy viscosity is modeled by:

$$\mu_t = \rho L_S^2 \frac{\left(S_{ij}^d S_{ij}^d\right)^{3/2}}{\left(\bar{S}_{ij}\bar{S}_{ij}\right)^{5/2} + \left(S_{ij}^d S_{ij}^d\right)^{5/4}} \qquad 3.4.5$$

where the WALE model defines L_s and S_{ij}^d as:

$$L_s = \min\left(kd, C_w V^{1/3}\right) \qquad 3.4.6$$

$$S_{ij}^d = \frac{1}{2}\left(\bar{g}_{ij}^2 + \bar{g}_{ij}^2\right) - \frac{1}{3}\delta_{ij}\bar{g}_{kk}^2 \qquad 3.4.7$$

$$\bar{g}_{ij} = \frac{\partial \bar{u}_i}{\partial x_j} \qquad 3.4.8$$

and the WALE constant, C_w, is 0.325 (ANSYS 2011). An advantage of the WALE model is its ability to correctly treat laminar zones within the domain due to returning zero turbulent viscosity for laminar flows (ANSYS 2011). This is in contrast to other models, such as the Smagorinsky-Lilly model, which will produce non-zero turbulent viscosity (ANSYS 2011).

3.5 Computational Aeroacoustics

Although the governing equations for CAA are the same as that of fluids, acoustical wave propagation has significantly less energy in comparison to the flows that cause it (ANSYS 2011). An oscillation of just 1 Pa results in a 94 dB sound wave, equivalent to the sound of a blender or passing motorcycle. As such, the predictions for far-field tonal noise use an acoustic analogy based on Lighthill's analogy. Ffowcs-Williams Hawkings (FW-H) is a time-domain integral formulation that adapts this analogy to compute sound signals or sound pressure at receiver locations from surface integrals (Fu and Vigevano 2022). This surface is defined as a source and can be a wall that is either permeable or impermeable (Li et al. 2020). Broadband and tonal noise can be predicted with the FH-W model, and it is dependent on the turbulence model and time scale of the transient flow (Zhong, Zhang, and Huang 2019). An important limitation of note is the assumption of sound propagation towards free space, meaning interior flows cannot use this model (ANSYS 2011). As only external aerodynamics is of concern in the present case, however, this issue is not of immediate concern.

The inhomogeneous wave equation used for FW-H is derived from manipulating the continuity and Navier-Stokes equations. The resultant monopole, dipole and quadrupole terms can be found by:

$$\frac{1}{a_0^3}\frac{\partial^2 p'}{\partial t^2} - \nabla^2 p' = \frac{\partial^2}{\partial x_i \partial x_j}\{T_{ij}H(f)\} \qquad 3.5.1$$

$$-\frac{\partial}{\partial x_i}\{[P_{ij}n_j + \rho u_i(u_n - v_n)\delta(f)]\}$$

$$+\frac{\partial}{\partial t}\{[\rho_0 v_n + \rho(u_n - v_n]\partial(f)\}$$

where *u* is the fluid velocity, *v* is the surface velocity, *p'* is the far-field sound pressure, $\delta(f)$ is the Dirac delta function and $H(f)$ is the Heaviside step function (ANSYS 2011). Conversely the Lighthill stress tensor can be found by:

$$T_{ij} = \rho u_i u_j + P_{ij} - a_0^2(\rho - \rho_0)\delta_{ij} \qquad 3.5.2$$

where a_0 is the far-field speed of sound and P_{ij} is the compressive stress tensor:

$$P_{ij} = p\delta_{ij} - \mu\left[\frac{\partial u_i}{\partial x_j} + \frac{\partial u_j}{\partial x_i} - \frac{2}{3}\frac{\partial u_k}{\partial x_k}\delta_{ij}\right] \quad 3.5.3$$

The wave Equation 3.5.1 can be integrated resulting in surface integrals and volume integrals (ANSYS 2011). While the volume integrals represent the quadrupole sources, the surface integrals account for acoustic monopole and dipole sources. The dipole is a function of fluctuating surface forces, while the monopole is a function of aspiration through the surface typically associated with permeable walls (Michel et al. 2009). Additionally, partial quadrupole sources are represented by the surface integral. ANSYS Fluent assumes negligible volume integrals, and results in the following:

$$p'(\vec{x},t) = p'_T(\vec{x},t) + p'_L(\vec{x},t) \quad 3.5.4$$

where thickness and loading terms respectively are given by:

$$4\pi p'_T(\vec{x},t) = \int_{f=0}\left[\frac{\rho_0\left(\dot{U}_n + U_{\dot{n}}\right)}{r(1-M_r)^3}\right]dS + \int_{f=0}\left[\frac{\rho_0 U_n\{r\dot{M}_r + a_0(M_r - M^2)\}}{r^2(1-M_r)^3}\right]d \quad 3.5.5$$

$$4\pi p'_L(\vec{x},t) = \frac{1}{a_0}\int_{f=0}\left[\frac{\dot{L}_r}{r(1-M_r)^2}\right]dS \quad 3.5.6$$

$$+\int_{f=0}\left[\frac{L_r - L_M}{r^2(1-M_r)^2}\right]dS$$

$$+\frac{1}{a_0}\int_{f=0}\left[\frac{L_r\{r\dot{M} + a_0(M_r - M^2)\}}{r^2(1-M_r)^3}\right]$$

and

$$U_i = v_i + \frac{\rho}{\rho_0}(u_i - v_i) \quad 3.5.7$$

$$L_i = P_{ij}\hat{n}_j + \rho u_i(u_n - v_n) \quad 3.5.8$$

with $f = 0$ mathematically representing the surface corresponding to the noise source and n_i being the unit vector towards the exterior region ($f > 0$) (ANSYS 2011).

3.6 Geometry and Boundary Conditions

As a NACA 0012 airfoil is to be used, the coordinates are found using the following definition to generate a 2D curve with a chord length of 1 m.

$$y = 0.6(0.2969\sqrt{x} - 0.1260x - 0.3516x^2 + 0.2843x^3 - 0.1015x^4) \qquad 3.6.1$$

This curve is scaled down by 0.3, resulting in a chord of 300 mm, and imported into SolidWorks where a domain can be created around the airfoil. A minimum distance between the surface of the airfoil and edge of the domain is maintained of at least 3 chord lengths to prevent boundary condition interference. The resultant domain can be seen in Figure 3.6.1 and has a frontal radius of 1 m with an overall length of 2.25 m. The span of the domain is 25.4% of the chord, or 0.0762 m. The span of the airfoil was determined as a multiple of the spanwise dimple spacing derived from literature (Ananthan et al. 2022; van Nesselrooij et al. 2016). A blunt trailing edge of 0.6 mm is also used to ease in structured meshing and to comply with Blakes Criteria for tonal noise. To improve mesh skewness at later steps, the inlet is rounded to better contour with the leading edge of the airfoil. To observe turbulent trailing edge noise, the boundary layer must be turbulent for a symmetrical airfoil at an AoA = 0° (Arce León et al. 2017). This is typically ensured by a BLT via a zig-zag strip shortly after the leading-edge (Rooks 2016). In real world applications, however, this is rarely done as introducing noise is inherently counterintuitive for most scenarios. As such no BLT is used to better simulate real world conditions.

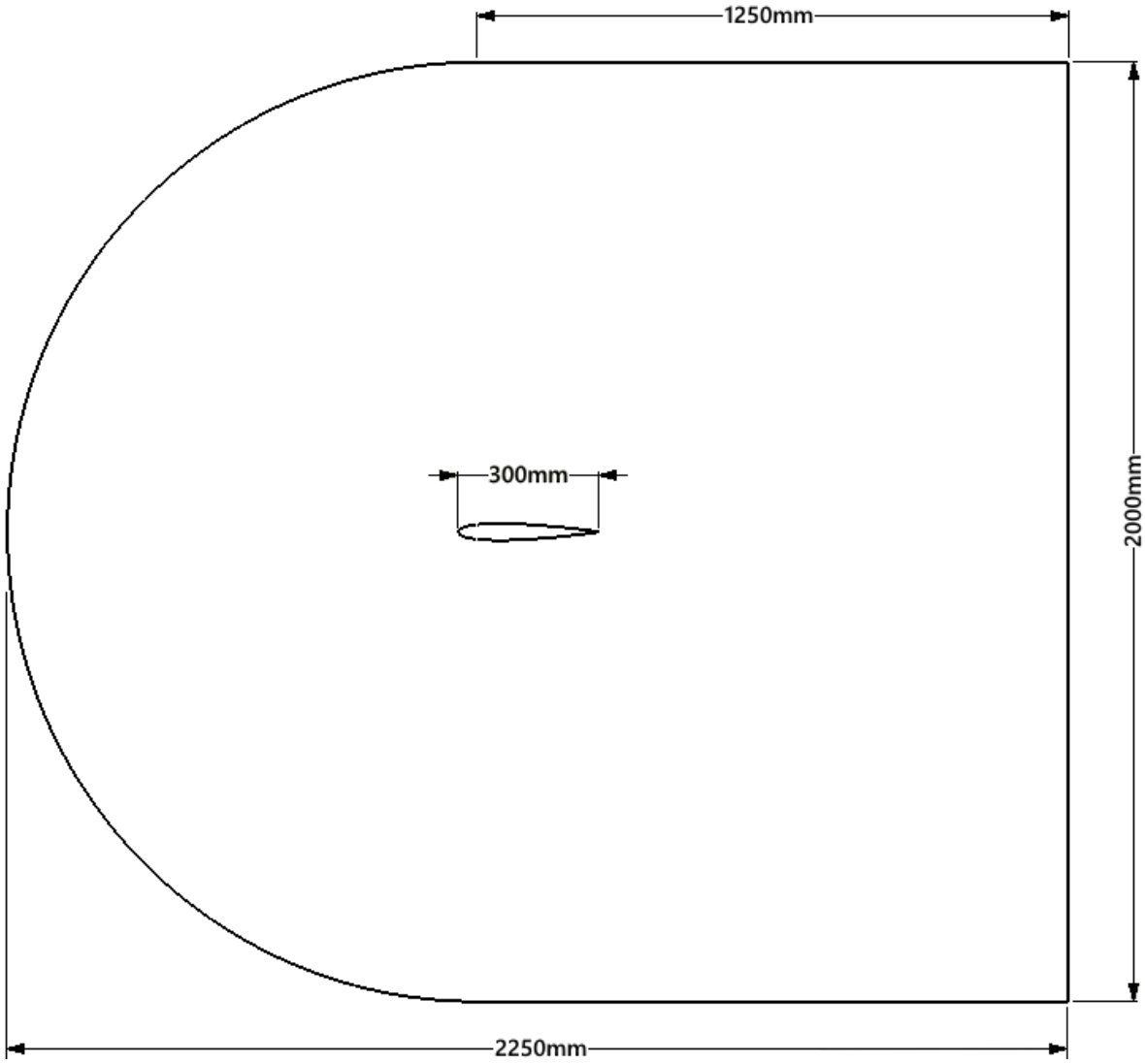

Figure 3.6.1: Fluid Domain for NACA 0012

After generating the domain, the clean airfoil is augmented with shallow spherical dimples. Only a spherical dimple is to be studied, with depth and array size to be altered. A preliminary parametric study is conducted with a depth to diameter ratio (d/D) of 2.5%, 3.3%, 5%, 7.5%, 10% and 15%, which is visualized in Figure 3.6.2. This is done on an array covering the latter 33% X/c of the airfoil, as an array was shown to be the most effective configuration by the authors in (van Nesselrooij et al. 2016). The trailing edge array closely follows the geometry used by the authors in (Ananthan et al. 2022) and is applied with the intent of reducing the trailing edge wake. The preliminary investigation utilizing RANS is used to analyze the flow

characteristics and aerodynamic performance of each d/D. The objective analysis for determining the aerodynamic performance is discussed in subsequent sections. Finally, array size is altered, with the latter 20%, 33% and 50% X/c of the airfoil taken by the array of dimples. As suggested by literature, an increase in surface area covered by shallow dimples increases their drag reduction effects (C.M. Tay 2011; van Campenhout et al. 2018). The parameters of the dimples implemented are derived from literature, and can be seen in Figure 3.6.3 and Table 3.6.1 with all measurements given in reference to the chord length (c) (van Nesselrooij et al. 2016; Ananthan et al. 2022). Spanwise and chordwise spacing of the dimples is maintained for each case at 6.35% $L_{Z/c}$ and 7.33% $L_{X/c,}$ respectively. The diameter and radius for each dimple's fillet is also maintained between depths, ensuring d/D and array size are the only variables altered.

a) 2.5% b) 3.3% c) 5% d) 7.5% e) 10% f) 15%

Figure 3.6.2: Comparison of Dimpled d/D of a) 2.5% b) 3.3% c) 5% d) 7.5% e) 10% f) 15%

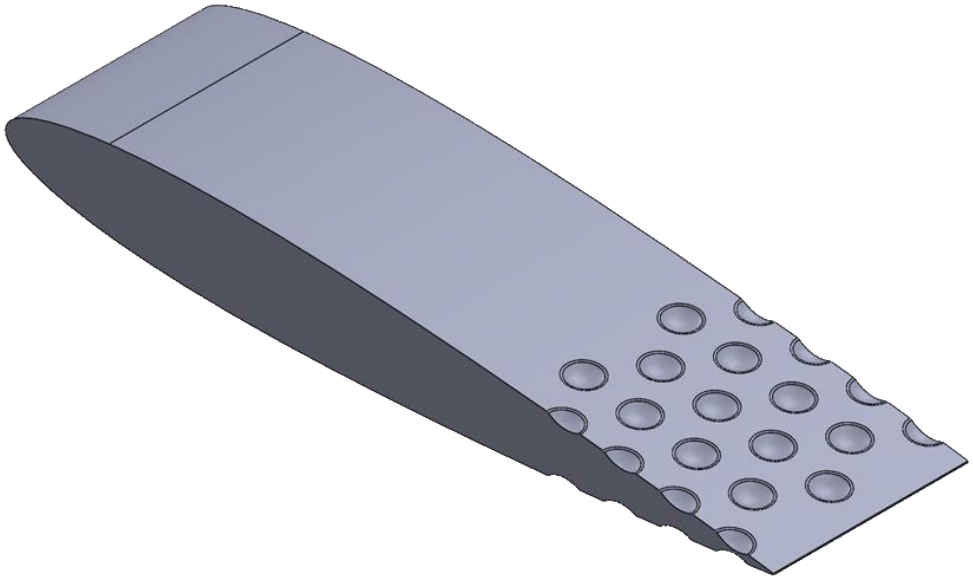

Figure 3.6.3: Dimple Array Orientation on the Airfoil with 15% d/D

Table 3.6.1: Adopted Dimple Geometry (van Nesselrooij et al. 2016; Ananthan et al. 2022)

Parameter	Dimensionless Value
Dimple Diameter, D/c	4.17%
Dimple Depth, d/D	2.5%, 3.3%, 5%, 7.5%, 10% and 15%
Chamfer Radius, r/c	0.5%
Log. Spacing, $L_{X/c}$	7.33%
Lat. spacing, $L_{Z/c}$	6.35%

The resultant airfoil profiles with increasing array coverage can be seen in Figure 3.6.4. For clarification, the dimple arrays are referred to by the percentage of the chord they occupy on the trailing portion of the airfoil. From left to right the arrays studied cover the latter 20%, 33% and 50% X/c of the airfoil on both upper and lower surfaces and are referred to as 20% DIM, 33% DIM and 50% DIM, respectively.

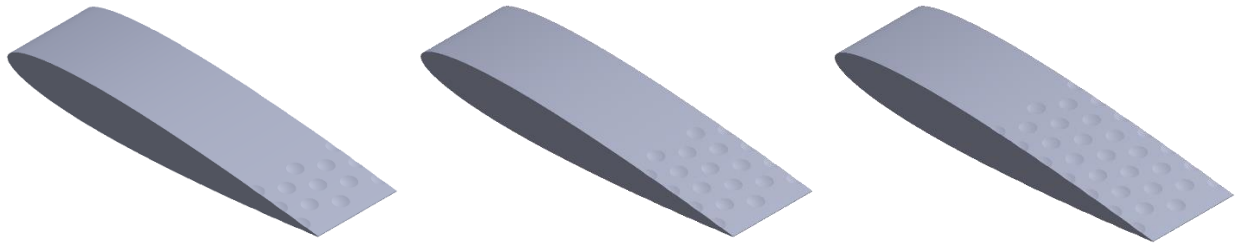

a) 20% DIM b) 33% DIM c) 50% DIM

Figure 3.6.4: Shallow Dimple Geometry on Latter a) 20% DIM b) 33% DIM and c) 50% DIM

Once the fluid domain is created for both clean and dimpled cases, it is meshed in ANSYS Meshing. A structured C-mesh for the airfoils is achieved through splitting the domain's faces to apply edge refinements in desired areas. A structured mesh is desired as it offers simplicity and efficiency for the solver, requiring a third of the memory when compared to an unstructured mesh of the same element count (Bern and Plassmann 2000). Unstructured meshes are more adaptable, however, and can be applied to more complex domains. Typically, unstructured meshes make use of triangular or tetrahedral elements while structured meshes make use of quadrilateral or hexahedral elements. Structured meshes can be objectively

defined as having all interior vertices being topologically alike, such as a grid (Bern and Plassmann 2000). The leading and trailing edge portions of the mesh are highlighted in Figure 3.6.5, where a grid-like pattern is easily distinguished. The mesh near the surface of the airfoil is refined and reduces to a thickness of 0.213 mm. The bias factor for this refinement, ratio of largest edge to smallest edge, is 125. This results in the outer extents of the domain having a maximum cell length of 26.625 mm. As the freestream areas are not as critical to model, more nodes can be placed on the boundary layer with this refinement. At all AoAs, the interior of each mesh maintains a structured composition as seen in Figure 3.6.6, which shows a cross section of the mesh at 90% X/c.

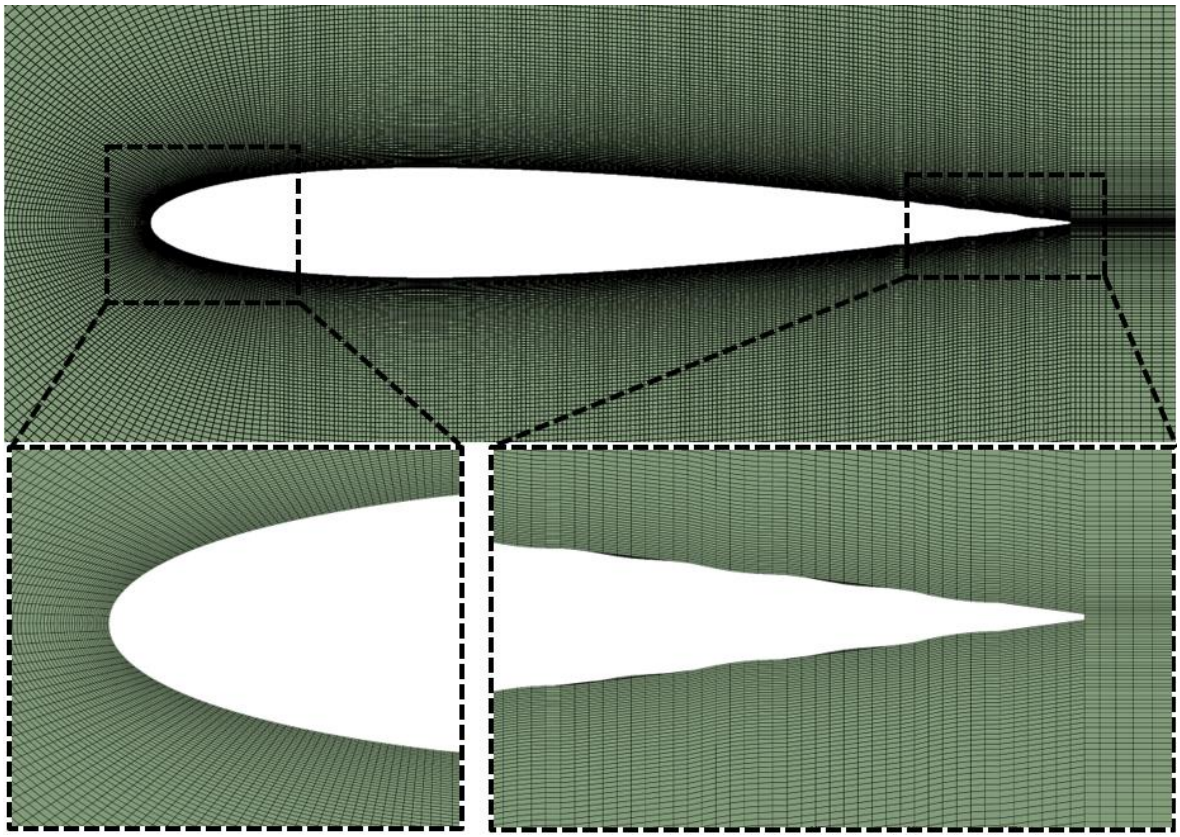

Figure 3.6.5: Mesh of Fluid Domain for NACA 0012 Airfoil in Clean and Trailing Edge DIM Arrays

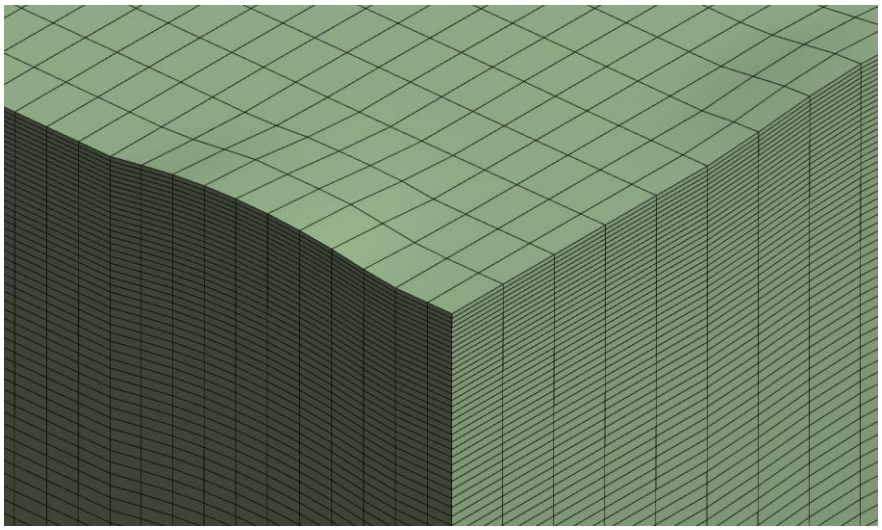

Figure 3.6.6: Interior Cross Section of Structured Mesh at 90% X/c

Mesh quality can be assessed with sqewness and orthogonality. Skewness refers to how close a cell is to its ideal shape. A rhombus, for insance, will have low skewness when compared to a rectangle. Orthogonality is related to the angle between the vector connecting two ajacent cell centers and the normal vector of the face shared by these two cells, which is visualized in Figure 3.6.7. Two rhombuses adjacent to each other will have a high orthogonality when compared to two rectangles adjacent to each other. An ideally shaped cell will have a skewness of 1 and an orthogonality of 0. The final meshes average a maximum skewness of 0.478 and a minimum orthogonality of 0.728, which is well within the acceptable range suggested by ANSYS for usage in Fluent (ANSYS 2011).

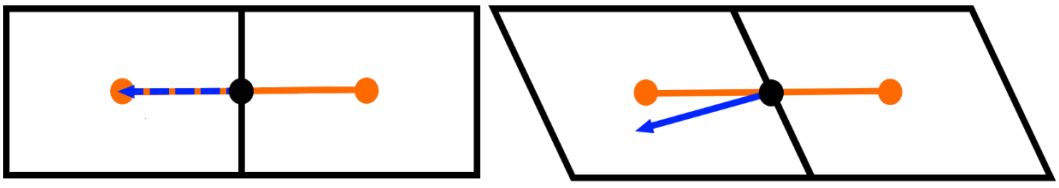

a) Non-orthogonal = 0 b) Non-orthogonal = 20

Figure 3.6.7: Representation of Orthogonality for a 2D Mesh Where a) Non-orthogonal = 0 and b) Non-orthogonal = 20

3.7 Aerodynamic Similarity Criteria

When comparing various works, it is important to maintain similarity criteria in order to ensure all parameters are properly scaled. These scaling factors are typically made in reference to a model and prototype and go beyond simply matching the Reynolds and Mach numbers (Weigand and Simon 2006). The first criteria is geometric similarity, which requires the model and prototype bodies to have a linear scaling factor in all three coordinate directions. By making use of Equation 3.6.1 the airfoil geometry can be derived, in particular the chord length for use in Table 3.6.1. By applying a scaling factor to Equation 3.6.1, geometric similarity can be neatly observed. Kinematic similarity, or the similarity of time scales, can be derived through the Froude Number relationship:

$$F_r = \frac{{U_{0p}}^2}{gL_p} = \frac{{U_{0m}}^2}{gL_m} \qquad 3.7.1$$

where U_{0p} is the freestream velocity for the prototype, U_{0m} is the freestream velocity for the model, and g is the acceleration due to gravity (Cathers 2021; Weigand and Simon 2006). The characteristic length, L_p and L_m, can be defined by the chord length for the prototype and model, respectively. From this, $F_r = 187.65$ for the present case. The third parameter is concerned with dynamic similarity, and yields a scaling of forces which can be determined by the relationship in Equation 3.7.2 (Cathers 2021).

$$F_p = F_m \left(\frac{\rho_{0p}}{\rho_{0m}}\right)\left(\frac{U_{0p}}{U_{om}}\right)^2\left(\frac{L_p}{L_m}\right)^2 \qquad 3.7.2$$

Lift and drag coefficients can also be used to provide insight when comparing the relative aerodynamic performance of a model to a prototype. Drag coefficient is found by the following equation:

$$C_d = \frac{F_x}{\frac{1}{2}\rho_0 U_0^2 A} \qquad 3.7.3$$

where F_x is force in the X direction, ρ_0 is the freestream fluid density, and A is the wing area. The force in the freestream direction, F_x, is found by integrating pressure on the airfoil surface in the X direction. For completeness, the lift coefficient can be found using Equation 3.7.4:

$$C_L = \frac{F_y}{\frac{1}{2}\rho_0 U_0^2 A} \qquad 3.7.4$$

where F_y is force in the Y direction, found by integrating the pressure on the airfoil surface in a similar manner to F_x.

3.8 Steady-State Setup

The RANS simulation is used for aerodynamic investigation of the airfoils and initialization of the LES simulations to follow. As discussed in Chapter 3, the two-equation k-ω SST turbulence model is used as it combines the near wall benefits of the k-ω model with the benefits of the k-ε in the freestream. Boundary conditions can be seen in Figure 3.8.1, with the inlet shown in red, outlet shown in blue and opening shown in green. A low Reynolds number of 4.8×10^5 is accomplished by an inlet velocity of 23.5 m/s given as a component to ensure a unified flow in the X direction. This also results in a $Re_D = 1.64 \times 10^4$ and a $Ma = 0.07$. Openings are used on the upper and lower faces of the domain to reduce any influence of wall effect, with a pressure outlet at the rear. As the velocity is far below where compressibility effects take place, and no aeroacoustic data is to be taken from the RANS simulations, a pressure-based solver is used to further reduce computational demands. Air is assumed to be at sea level with a density of 1.225 kg/m³ and a dynamic viscosity of 1.789×10^{-5} Pa·s.

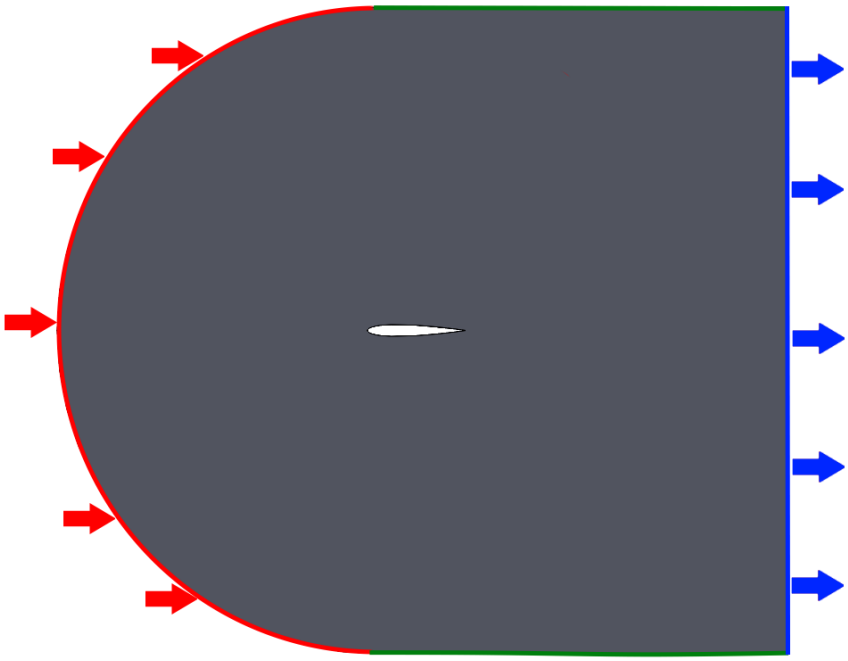

Figure 3.8.1: Boundary Conditions for NACA 0012 Cases

After the RANS cases converge, the results are processed using ANSYS Post. Conversely, the solution data is also exported as an interpolation. As the interpolated flow field is saved, not the direct solution data, it can be applied to a case with differing boundary conditions, mesh, and geometry. This export can then be used to initialize the transient simulation and reduce the time for flow to fully develop around the airfoil.

3.9 Transient and Aeroacoustic Setup

The LES model uses similar boundary conditions to the RANS model. A density-based solver is used, with the ideal gas law used for air density. The opening boundary condition is changed to a Pressure-Farfield to effectively approximate the true infinite-extent conditions when ideal gas law is applied. This boundary condition models free-stream conditions at infinity, reducing acoustic wave reflection, and it is only applicable when ideal gas law is used for fluid density (ANSYS 2011). Even though air can be assumed incompressible for aerodynamic purposes when $Ma < 0.3$, there can still be fluctuations in density of up to 5% (Dahl 1997). These fluctuations can be considered negligible for computation of the flow field but are

necessary for the acoustic field. If an acoustic wave of 140 dB is simulated, a 0.4% variation in density is expected (Dahl 1997). Thus, the compressibility effects should be modeled, even at such a low Mach number. The FW-H acoustics analogy is then applied, with the airfoil surface as the source. At an observer distance of 0.5 m, 24 receivers are set at 15° increments which can be seen in Figure 3.9.1. The coordinate locations for these points are presented in Table 3.9.1. All receivers are on the chordwise center plane of the airfoil (Z = 0), with point 1 being immediately aft of the trailing edge. Points are then numbered sequentially in a counterclockwise order. Point 19, for example, is 0.5 m below the airfoil while point 13 is directly ahead of the airfoil.

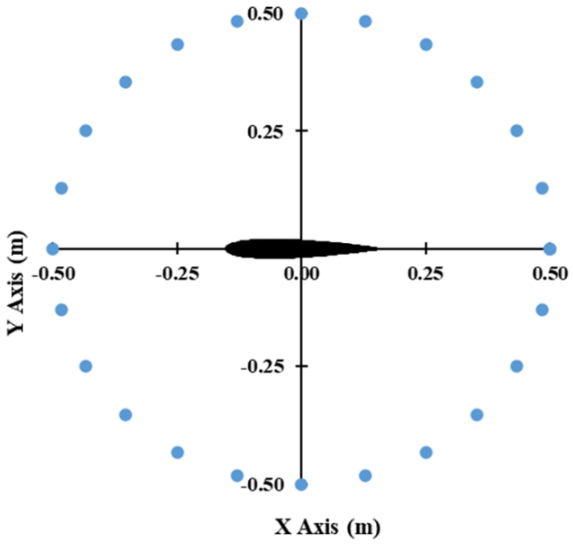

Figure 3.9.1: Receiver Locations Around the Airfoil Along the Center Chordwise Plane

Table 3.9.1: FW-H Receiver Coordinates

Point	θ (°)	X (m)	Y (m)
1	0	0.50	0.00
2	15	-0.38	0.33
3	30	0.08	-0.49
4	45	0.26	0.43
5	60	-0.48	-0.15
6	75	0.46	-0.19
7	90	-0.22	0.45
8	105	-0.12	-0.49
9	120	0.41	0.29
10	135	-0.50	0.04
11	150	0.35	-0.36
12	165	-0.03	0.50
13	180	-0.30	-0.40
14	195	0.49	0.11
15	210	-0.44	0.23
16	225	0.18	-0.47
17	240	0.16	0.47
18	255	-0.43	-0.25
19	270	0.49	-0.09
20	285	-0.32	0.39
21	300	-0.01	-0.50
22	315	0.33	0.37
23	330	-0.50	-0.07
24	345	0.42	-0.27

To ensure the flow does not surpass more than one cell per time-step, a Courant number of less than 1 is used to satisfy the Courant–Friedrichs–Lewy condition. A time-step of 1.25×10^{-5} seconds results in a courant number of 0.94. With 20000 time-steps, this allows for just under 3 flow passes. This was found to be sufficient for the flow field to fully develop with the RANS initialization. Only the last 0.0256 seconds are considered for acoustic analysis as a factor of 2^n time-steps are required for the fast Fourier transform.

The transient simulations are run on a Linux based system with 192 Intel Xeon Platinum 8168 cores with an average run time between 144-233 hours, depending on the configuration and other users of the system. Results are then imported to a local Windows machine for post processing within ANSYS Post.

3.10 Mesh Convergence Study

A mesh convergence study was conducted for the clean and a trailing edge dimpled case at an AoA = 6° with the RANS setup. This was done to ensure both lift and drag converge, as at an AoA = 0° a symmetrical airfoil is expected to produce zero lift. Five structured C-meshes are used for both clean and dimpled cases, with the coarsest meshes being 201,960 elements. The next case, refered to as coarse-medium, reduces element sizes to 75% of the coarse case. This reduction continues for the medium, medium-fine, and fine cases culminating in 5,456,160 elements for clean and dimpled meshes. The element count for each mesh can be seen in Table 3.10.1, where the estimated y^+ values can also be seen. Idealy a $y^+ < 1$ is used for LES to fully resolve the boundary layer, however this is not computationaly feasible given the three-demensional model and computer hardware limitation. Using the minimum cell length as the distance to the nearest node, the fine case has a y = 0.1766 mm. Skin friction is first estimated using Equation 3.10.1, which can then be used to compute the wall shear stress and friction velocity in Equations 3.10.2 and 3.10.3, respectively. Finally, Equation 3.1.4 is used to solve for the y^+ value given the wall to node distance. For the fine mesh, this results in a C_f = 4.275×10^{-3}, τ_w = 1.447, u_* = 1.087, and y^+ = 13.10.

$$C_f = [2log_{10}(Re) - 0.65]^{-2.3} for\ Re < 10^9 \quad 3.10.1$$

$$\tau_w = C_f \cdot \frac{1}{2}\rho U_0^2 \quad 3.10.2$$

$$u_* = \sqrt{\tau_w/\rho} \quad 3.10.3$$

Additionally, root-mean-square (RMS) residuals for all equations was set to 1×10^{-9}. This aggregates and normalizes the local imbalance of the continuity, momentum, turbulant kenetic energy and specificic dissapation rate equations for all elements. Residuals will decay to some small value, then stop changing as they have "leveled off" (ANSYS 2011). With limited computational capability, there must be a balance between the accuracy of results and time to solve. A comparison of said results can be seen in Figure 3.10.1, where lift and drag are compared for each convergence case tested.

Table 3.10.1: Mesh Refinement Comparison for Different Cases

Case	Estimated y^+	Clean Airfoil Element Count	Dimpled Airfoil Element Count
Coarse	33.92	201,960	201,960
Coarse-Med	27.46	656,640	656,640
Medium	19.32	1,617,120	1,617,120
Med-Fine	15.82	3,156,750	3,156,750
Fine	13.10	5,456,160	5,456,160

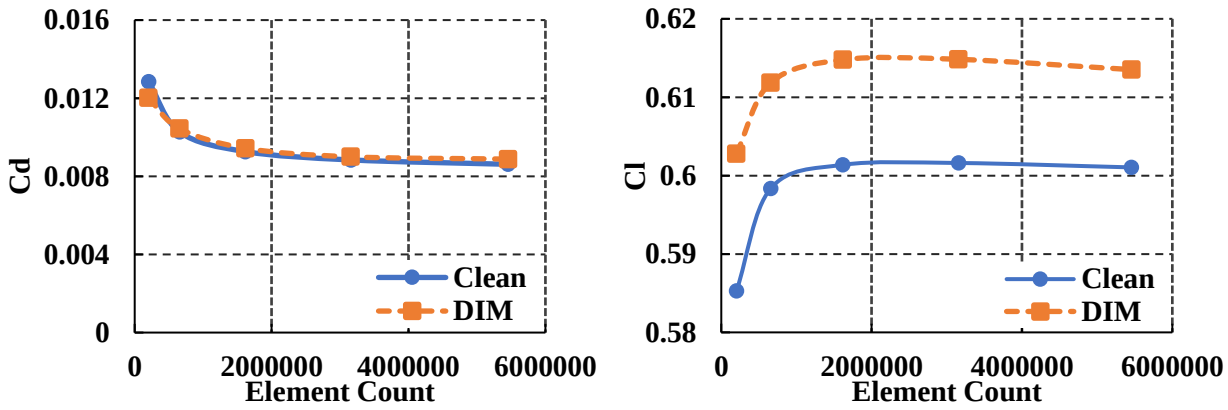

Figure 3.10.1: Convergence of Drag Coefficient (Left) and Lift Coefficient (Right) for Clean (Blue) and Trailing Edge DIM (Orange)

From the convergence study, an element count of 3.2 million is found to sufficiently detail the fluid flow around the airfoils. Increasing the mesh to the fine case for a change of 1.08% is deemed not worth the increase in computation required. The dimpled airfoil similarly results in a mesh with 3.2 million elements due to its identical meshing parameters. As such, all subsiquent meshes for differing AoAs and dimple configurations will use meshes made in the same manner.

3.11 Aerodynamic Validation

To validate the present NACA 0012 airfoil at a Re = 4.8×10^5, several studies at similar Reynolds numbers have been compiled. As with convergence, lift and drag are used for this purpose. As can be seen in Figure 3.11.1, there is significant discrepancy amongst literature. This could be due to experimental

uncertainty, differing flow regimes or slight geometry discrepancies such as a blunt trailing edge. Numerical studies are inherently defined by their turbulence model, which can drastically alter the near to post stall performance of an airfoil (Yousefi, Saleh, and Zahedi 2014). The k-ε model, for instance, often fails to accurately predict the post-stall region, while maintaining good accuracy in the pre-stall region (Yousefi, Saleh, and Zahedi 2014). The current study shows good agreement with X-Foil and the numerical results obtained by the authors in (Fatahian et al. 2020). When compared to the experimental from the authors in (Critzos, Heyson, and Boswinkle 1955; Jacobs and Sherman 1939), however, the current work tends to overpredict stalling behavior with a suggested stall (critical) AoA = 15°, much like comparable numerical studies and X-Foil. Testing only to an AoA = 6°, however, limits concern of this as the current model is shown to be accurate within this range especially.

a) Lift

b) Drag

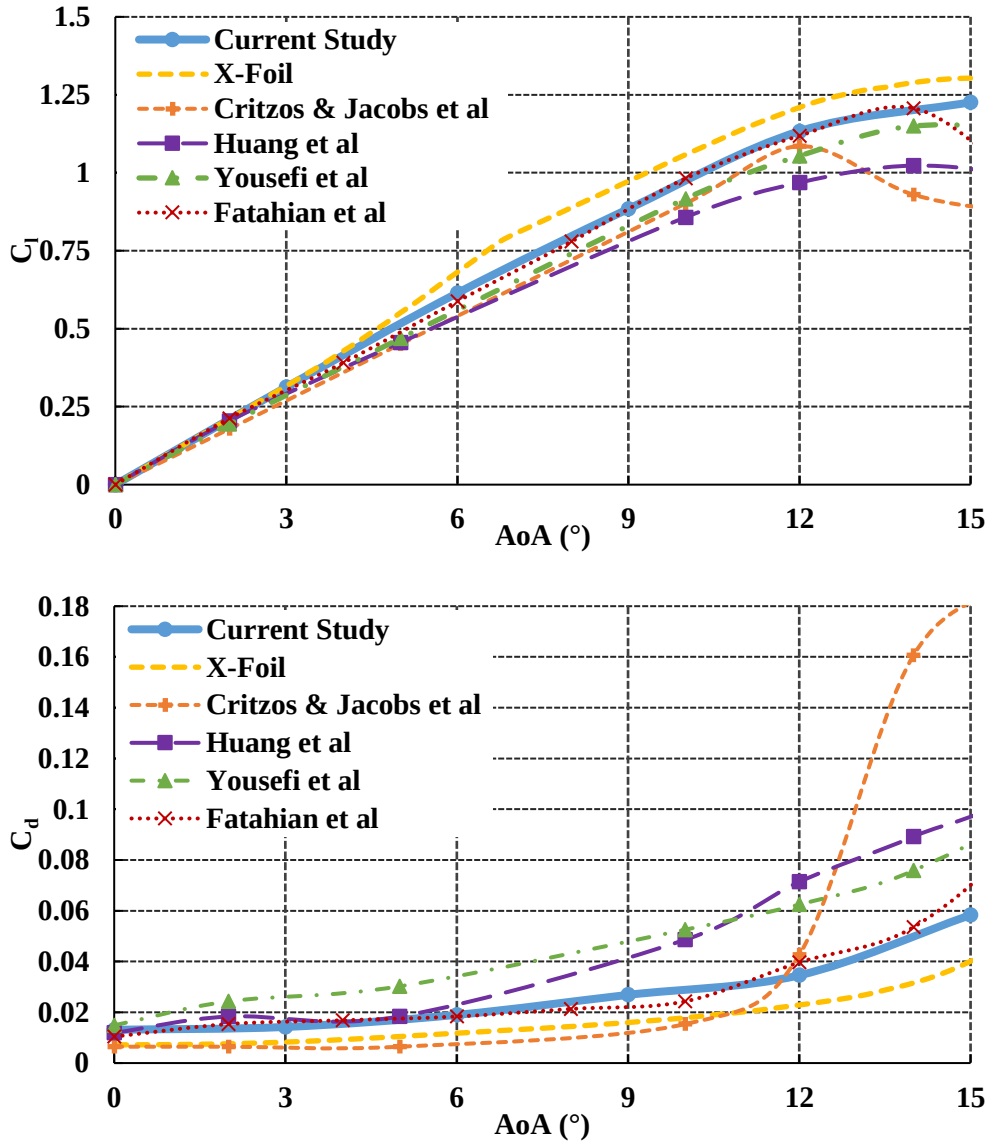

Figure 3.11.1: Comparison of Current Computational and Experimental a) Lift and b) Drag Results for a NACA 0012 (Huang et al. 2004; Yousefi, Saleh, and Zahedi 2014; Fatahian et al. 2020; Critzos, Heyson, and Boswinkle 1955)

Two models are of interest in the current work, however, and as such both must be validated. For this reason, an LES transient numerical simulation was conducted at the same AoAs as the previous validation. These simulations were conducted the same way as the rest of the study, being initialized via the RANS solution and allowed to run for just under 3 flow passes. The latter 0.1 seconds are then used for a time averaged solution to negate any effects of vortex shedding or other time-dependent flow. The results

of which can be seen in Figure 3.11.2, with the LES results directly compared to the RANS results. Until an AoA = 6° especially, both results show good agreement. At these lower AoAs, a drag difference of 9.98% is found on average. Lift is found to show little discrepancy between simulations at these lower AoAs at an average difference of 1.47%.

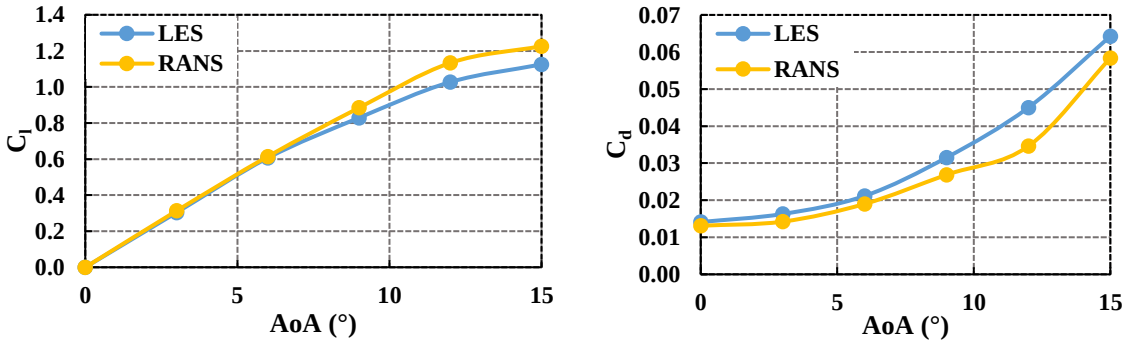

Figure 3.11.2: Comparison of Lift (right) and Drag (left) Between LES and RANS

3.12 Aeroacoustic Validation

Acoustic noise is the result of sound pressure waves propagating through a media. As such, any fluctuations in pressure are likely to increase noise propagation and can be expressed as a function of the turbulent boundary layer. Pressure information captured directly from each of the 24 probes within the computational domain is converted to a sound pressure level (SPL) using the following formula:

$$SPL = 20log\frac{p'}{p_{ref}} \qquad 3.12.1$$

where *p'* is the pressure fluctuation relative to resting pressure and $p_{ref} = 2 \times 10^{-5}\ Pa$. This reference pressure is the lowest audible limit of human hearing and corresponds to 0 dB. Decibel pressure levels are described over specified bands of frequencies, dividing each doubling of frequencies into thirds. This division is referred to as a 1/3 octave. Overall averaged sound pressure level (OASPL) can be calculated as the decibel equivalent of the root-square-sum of the 1/3 octave pressure and is a convenient portrayal of the

overall acoustic noise intensity. It is of note that OASPL is greater than any individual SPL value as it represents the intensity of the spectrum as a whole. Additionally, any averaged SPL mentioned is found by averaging the pressure before the use of Equation 3.12.1. This averaged pressure was then converted to decibels and was done to avoid misrepresentation caused by directly averaging logarithmically scaled values.

For validation purposes, two separate simulations with the current model were conducted, both at an AoA = 0° with differing Reynolds numbers as presented in Figure 3.12.1. The first case is for comparison against numerical results obtained by the authors in (Ananthan et al. 2022) at a Re = 4.2×10^5 with the same NACA 0012 airfoil. The second is at a Re = 5×10^5, which is compared against NACA 0012 experimental acoustic results (Al Tlua and Rocha 2021). It is of note that the Mach number between the current study and the experimental study are not identical, and some discrepancies may appear. It is also of note that Blake's criteria establishes a ratio $h/\delta^* > 0.3$ for tonal noise to occur, where h is the blunt trailing edge thickness at 0.6mm (Blake 2017). This yields 0.45 > 0.3 for the current study, and as such tonal noise is expected.

The authors in (Ananthan et al. 2022) show high frequencies, 5,000 Hz < f < 10,000 Hz, that are louder than the current numerical model. This can be caused by a lack of a BLT in the current study, which reduces the turbulence within the boundary layer. Taking this into account, the resultant trend appears to follow that found by the authors in (Ananthan et al. 2022), with a relatively flat response above 2,000 Hz. Lower frequencies, 100 Hz < f < 2,000 Hz, taper towards this flattening, with a steady decline in sound pressure. Increasing the Reynolds number shows much closer resemblance to the experimental results when no BLT was used (Al Tlua and Rocha 2021). Tonal noise, however, is present in the current study at 367 Hz when it is not in experimental literature. This could be caused by a variety of factors; however, the most probable cause is the blunt edge on the current model causing vortex shedding at this frequency. It is of note that the experimental study reported tonal noise at other configurations, with a consistent occurrence at 470 Hz regardless of the increased AoA, BLT usage or Reynolds number tested (Al Tlua and Rocha 2021). Additionally, minor change in OASPL was observed experimentally as AoA increased, with the

introduction of tonal noise being the most prominent alteration in noise emission (Al Tlua and Rocha 2021). Furthermore, referencing the work from the authors in (Paterson et al. 1973), more specifically Equation 2.6.2, a tonal frequency of 537.46 Hz is expected for this velocity and chord length. Neither of these two cases are found to show tonal noise at this frequency. As such, it can be concluded that the current study shows good agreement with literature.

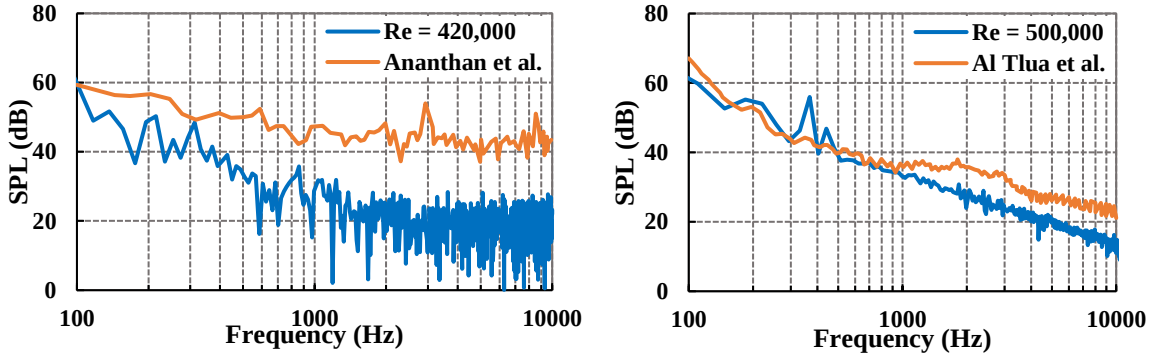

a) $Re = 4.2 \times 10^5$ b) $Re = 5 \times 10^5$

Figure 3.12.1: Acoustic Comparison Between Literature at a Re = a) 4.2 × 10^5 and b) 5 × 10^5

CHAPTER 4

RESULTS

The results presented are a comparison between the clean and trailing edge dimpled arrays. As such, the chapter is divided into four sections. A comparison of dimple depths with respect to the clean airfoil is first investigated. Aeroacoustics of these varying depths is then discussed. The optimal depth is then applied to an array of varying sizes, starting 20%, 33% and 50% X/c from the trailing edge. A similar discussion of these cases follows, first the aerodynamic section followed by the acoustic section of the shallow dimple arrays. Unless otherwise noted, all comparisons made are with respect to the clean NACA 0012 airfoil. As most flights take place well before stalling, an AoA = 0°, 3° and 6° are of primary importance, especially for cruising and landing aircraft. As such, these AoAs are primarily discussed.

4.1 Effect of Dimple Depth on Aerodynamics

As expected for a symmetrical airfoil, the NACA 0012 produces negligible lift at zero AoA. This is maintained regardless of dimple d/D as they are evenly applied to both upper and lower surfaces. Symmetrical dimple application results in equal alterations to the flow on either side of the airfoil, canceling out any potential benefits or drawbacks in terms of lift. Increasing to an AoA = 3° yields minor change between the dimpled and clean cases in terms of lift. A minor reduction in lift of 0.36% when compared to clean is found for the 2.5% deep dimple, with losses staying similar for the 3.3% d/D and 5% d/D. Once surpassing a 7.5% d/D, lift decreases by 0.52% with losses becoming more prominent as the depth increases. This culminates in a 0.93% loss at the 15% d/D. This hints at a transition point that defines a shallow dimple, further suggesting the significant flow differences within the dimples as depths increase as suggested by literature (C.M.J. Tay, Khoo, and Chew 2015; Etter 2007). A transition point can be seen in Figure 4.1.1, where lift is plotted as a function of d/D for both AoA = 3° and 6°. Further increasing to an AoA = 6° reduces these losses in lift, suggesting the increasing beneficial impact of dimples at higher AoA.

There is still a loss in lift, however, with the shallower cases averaging an almost negligible 0.10%. This loss climbs with dimple depth to 0.59% at a 15% d/D.

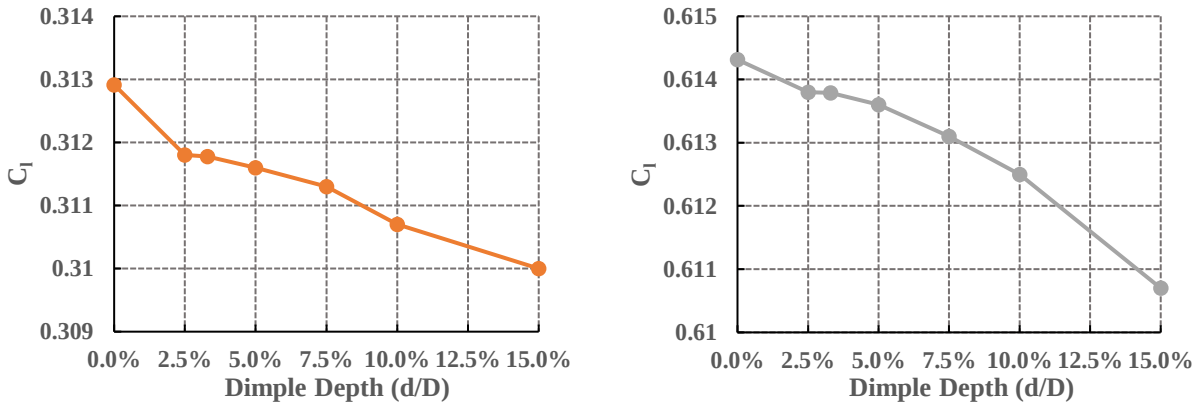

a) AoA = 3° b) AoA = 6°

Figure 4.1.1: Lift Coefficient as a Function of d/D for an a) AoA = 3° and b) AoA = 6°

Table 4.1.1: Lift Coefficient Comparison of Varying Dimple d/D

AoA (°)	Clean	2.5%	3.3%	5.0%	7.5%	10.0%	15.0%
0	4.18E-06	-8.54E-06	-1.82E-05	-1.01E-04	-1.02E-04	-9.56E-05	-9.37E-05
3	0.3129	0.3118	0.311777	0.3116	0.3113	0.3107	0.3100
6	0.6143	0.6138	0.6138	0.6136	0.6131	0.6138	0.6107

At an AoA = 0°, an increase in drag of 4.41% for the 2.5% d/D can be seen when compared to the clean case. This drag difference between the clean and dimpled cases stays relatively constant until the 7.5% d/D, at which point drag begins to steadily increase. This depth shows an increase of 6.09% when compared to the clean case. The deepest d/D assessed has an increase of 12.04%, a drastic increase from the shallowest three depths. Increasing to an AoA = 3° shows a similar trend, maintaining an approximate increase of 5% for the shallowest 3 depths. As with lift, drag alterations are significantly higher as d/D is increased beyond 7.5% d/D and can be visualized in Figure 4.1.2a. At these lower AoAs, no flow detachment is expected suggesting a negative pressure gradient mitigates the effectiveness of the shallow dimples as suggested by literature (P. R. Spalart et al. 2019). This gradient, however, begins to weaken as

AoA is increased which can be beneficial in increasing the dimples performance. This can be seen in Figure 4.1.2b, as an AoA = 6° yields a drag decrease across all depths apart from the 10% d/D and 15% d/D. Once again, the shallowest three depths show similar performance at an average reduction of 1.20%.

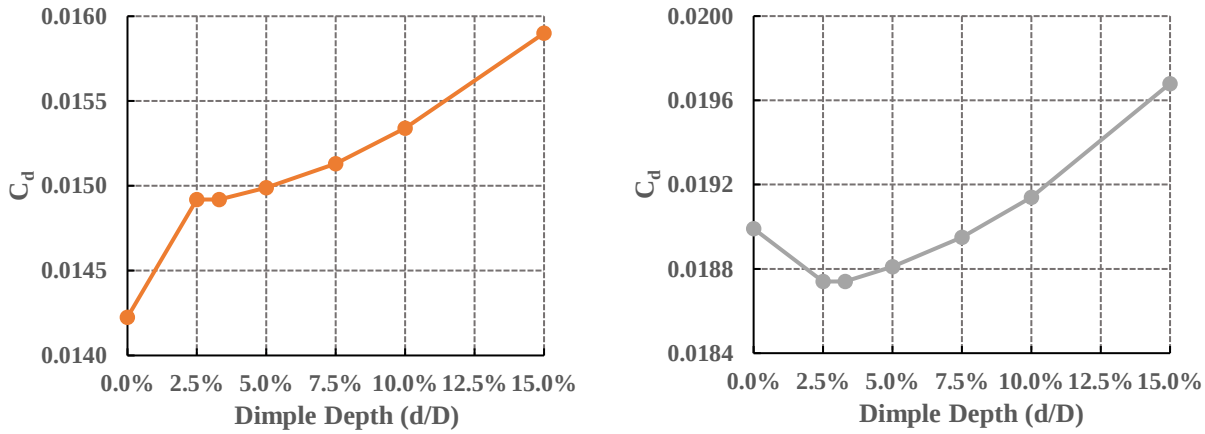

a) AoA = 3° b) AoA = 6°

Figure 4.1.2: Drag Coefficient as a Function of d/D for an a) AoA = 3° and b) AoA = 6°

Table 4.1.2: Drag Coefficient Comparison of Varying Dimple d/D

AoA (°)	Clean	2.5%	3.3%	5.0%	7.5%	10.0%	15.0%
0	0.01311	0.01369	0.01369	0.01376	0.01391	0.01412	0.01469
3	0.01423	0.01492	0.01492	0.01499	0.01513	0.01534	0.01590
6	0.01899	0.01874	0.01874	0.01876	0.01895	0.01874	0.01968

Flow separation was found to occur on all dimples with a d/D ≥ 7.5%. Skin friction of the upper surface is plotted in Figure 4.1.3, in which all depths at an AoA = 3° are compared, with the latter 30% of the airfoil emphasized. This value can be found with the following equation:

$$C_f = \frac{\tau_w}{0.5 \cdot \rho U_0^2} \qquad 4.1.1$$

where τ_w is the wall shear stress, ρ is the fluid density and U_0 is the freestream velocity. Skin friction drops sharply as the flow enters the dimple, with the deeper depths showing negative skin friction signifying flow reversal. This is the result of the flow being unable to effectively follow the contour of the dimples and will

likely affect shallower dimples if a higher Reynolds number is used. This also defines the ratio for a shallow dimple, as literature states a ratio of 10% is the transition d/D due to a change in flow structure (C.M.J. Tay, Khoo, and Chew 2015). Flow reversal on the surface denotes a 'tumbling' flow due to an adverse pressure gradient, and the formation of counter-rotating vortices increase boundary layer turbulence. The increase in vortices and overall turbulence is not desirable acoustically either, as flow fluctuations have now been introduced.

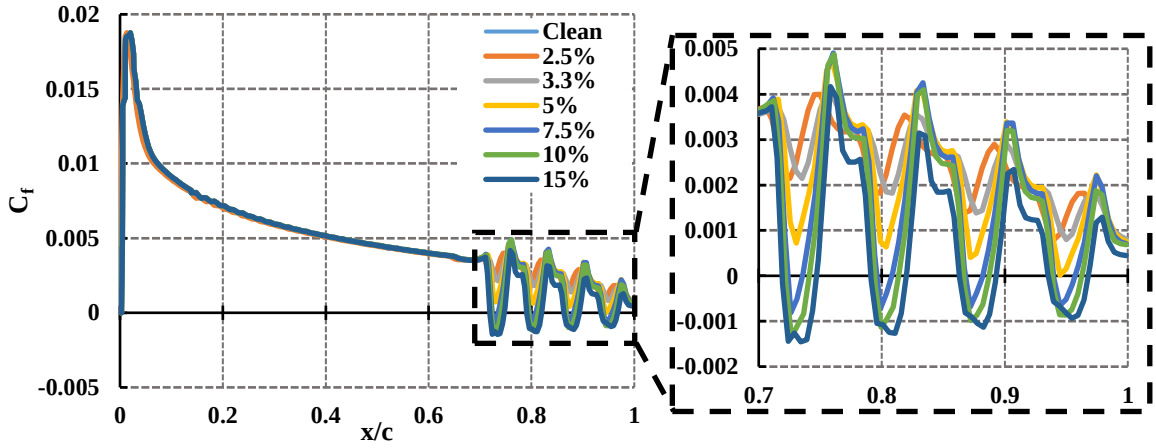

Figure 4.1.3: Skin Friction Comparison of Dimple Depths at an AoA = 3°

This alteration in performance once passing 7.5% d/D can be attributed to the differing flow structures caused by the shallow and deeper dimples. In Figure 4.1.4 a comparison of velocity vectors between the 5% d/D and 15% d/D can be seen, as these two cases exemplify the differences. The 5% d/D shows very steady patterns as the flow contours to the surface of the dimple. This necessitates the flow to decelerate upon entry and accelerate when exiting the dimple, which is reflected in the skin friction graphs. By contrast, the 15% dimple shows significantly more unstable, time dependent structures similar to the counter-rotating vortices described by literature (Liu and Li 2014). Flow circulation can be seen in Figure 4.1.4b on the 15% d/D, in contrast to the decelerating-accelerating of the 5% d/D. The transition of shallow dimples is shown to occur lower than the 10% suggested by literature, however, and is a symptom of the

drastically higher Reynolds number reducing the viscous effects of the fluid (C.M.J. Tay, Khoo, and Chew 2015). As such, the flow is unable to effectively stay attached to the dimple's contour.

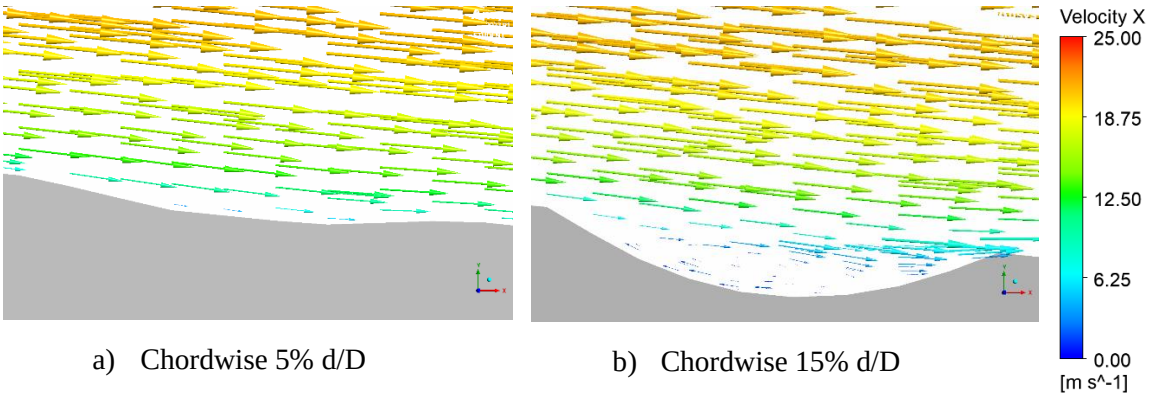

a) Chordwise 5% d/D b) Chordwise 15% d/D

Figure 4.1.4: Velocity Vector Fields for a) Chordwise 5% d/D and b) Chordwise 15% d/D

Turbulence induced by the dimples can be seen in Figure 4.1.5, with turbulence kinetic energy (TKE) being compared between the clean, 5% d/D and 15% d/D cases. TKE is the mean kinetic energy per unit mass of eddies in a turbulent flow, or the RMS of velocity fluctuations. This is directly solved for, represented by the *k* term in most RANS models. Comparison of the clean and 5% d/D cases shows trivial differences. As suggested by the velocity vectors in Figure 4.1.4, turbulence is generated by the deeper 15% d/D dimples, resulting in an increase in TKE within the dimples and the wake. As the turbulence is greater, the deeper dimples effectively pull energy from the freestream into the boundary layer. At moderate AoAs, however, this increased vorticity only serves to increase noise production. As noise is a function of turbulence, in essence increasing pressure oscillations, any increase in turbulence can increase acoustic emissions.

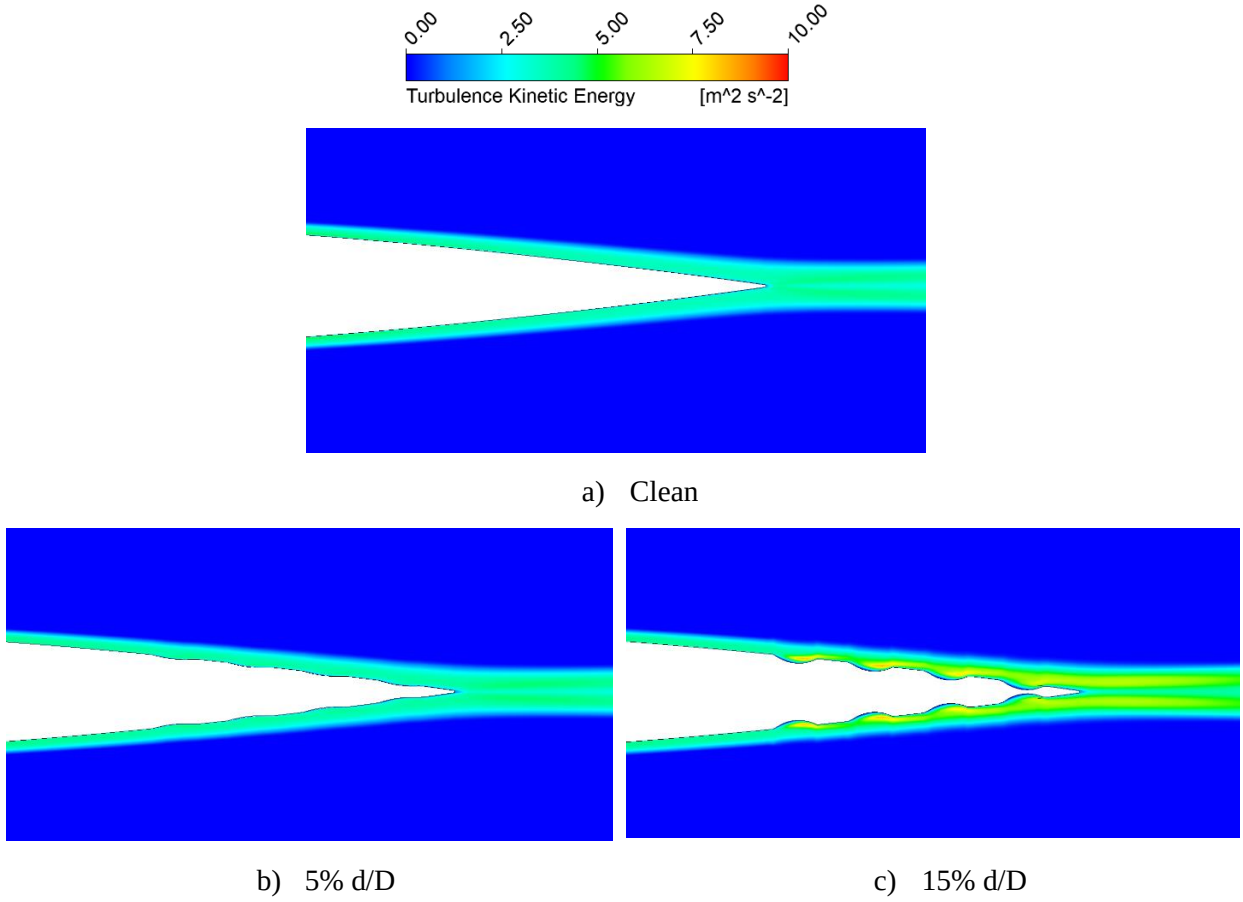

a) Clean

b) 5% d/D

c) 15% d/D

Figure 4.1.5: TKE Comparison of a) Clean, b) 5% d/D and c) 15% d/D

4.2 Effect of Dimple Depth on Aeroacoustics

From the aerodynamic analysis, it can be concluded that a d/D > 5% increases drag more than the allowed 5% of the success criterion. Additionally, the turbulence associated with deeper dimples acts counterintuitively towards the overall goal of noise reduction. As such, only 2.5% d/D, 3.3% d/D and 5% d/D are compared for their acoustic performance. For clarification, low frequencies refer to f < 2,000 Hz, mid frequencies refer to 2,000 Hz > f > 5,000 Hz, and high frequencies refer to f > 5,000 Hz. This notation is derived from the human ear's sensitivity to broadband noise from 2,000 Hz to 5,000 Hz (Gang, Zhengtao, and Pingguo 2019).

A comparison of the OASPL can be used to show noise emission directivity, as seen in Figure 4.2.1. Sound levels at each of the 24 receivers are plotted around the airfoil, where directions of importance are aft of and beneath the airfoil. The clean airfoil shows a radiation pattern like the type described by Blake in Figure 2.6.2. All three depths evaluated show close behavior when compared to each other, with the 5% d/D showing the greatest deviation of the three. The wake of the airfoil shows moderate decrease between 2.95 dB and 4.13 dB depending on the case. At this aft location, the 5% d/D shows the most reduction. This is likely due to the stronger oscillations caused by a deeper dimple, which is more effective at dispersing the turbulence at the trailing edge.

With an AoA = 0°, noise is reduced in all directions at approximately 7.5 dB for all depths. The 3.3% d/D shows slightly more reduction than the other two depths, being on average 1.07 dB quieter than the 2.5% d/D. This slight reduction is mostly directly above and beneath the airfoil with trailing edge noise showing a difference of less than 1 dB. Increasing to an AoA = 3°, the 3.3% d/D maintains its advantage when compared to the other depths. The 2.5% d/D shows reduced performance in front and behind the airfoil, suggesting the reduced oscillations caused by a shallower dimple begin to have a marginal effect on the trailing edge acoustics. Conversely, the 5% d/D shows slightly less reduction than the 3.3% d/D with a 1.39 dB difference between the two. Further increasing to an AoA = 6° yields an increase at 135° and 225° for the 5% d/D, at 71.79 dB and 69.31 dB, respectively. When compared to the clean case this is an increase of 7.20 dB and 4.79 dB, respectively. This is in addition to all around similar OASLP to the clean case, further showing the negative side effects of increasing dimple d/D. The 3.3% d/D, on the other hand, shows the best performance out of all the depths with a reduction of 4.51 dB beneath the airfoil. This comes at the cost of increased leading edge and trailing edge noise, especially when compared to the 2.5% d/D.

Table 4.2.1: OASLP Values at Select Locations Around Airfoil at AoA = 0° with Varying Dimple d/D

d/D	X = 0.5 m Y = 0 m (dB)	X = 0 m Y = 0.5 m (dB)	X = -0.5 m Y = 0 m (dB)	X = 0 m Y = -0.5 m (dB)
Clean	61.71	67.17	63.23	67.13
2.5%	58.76	59.75	60.11	59.43
3.3%	57.97	58.61	58.44	58.49
5.0%	57.58	59.75	58.95	59.88

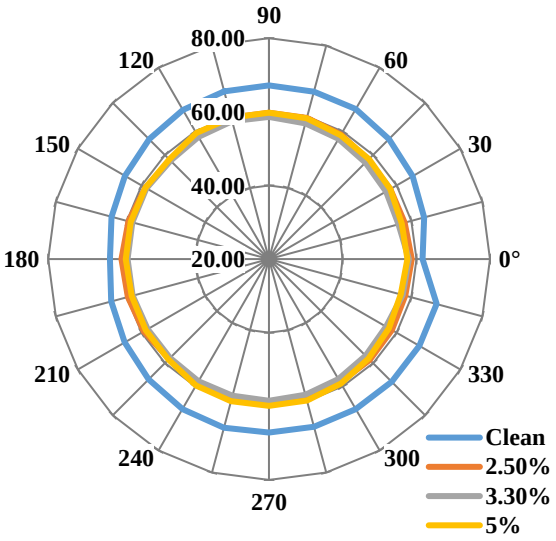

a) AoA = 0°

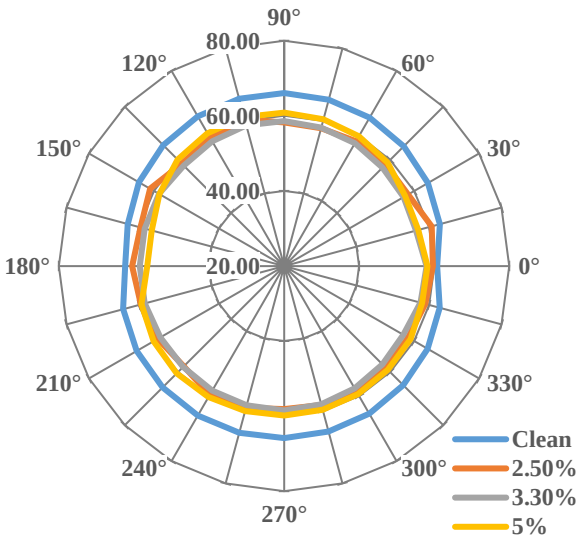

b) AoA = 3°

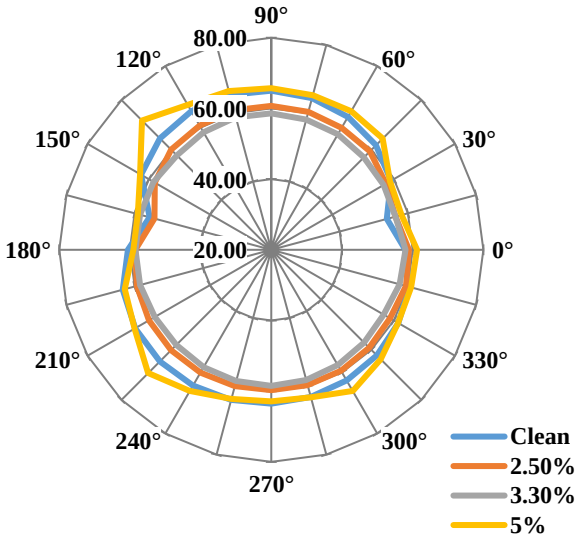

c) AoA = 6°

Figure 4.2.1: OASPL of Varying Dimple d/D at an a) AoA = 0° b) AoA = 3° and c) AoA = 6°

As a listener is unlikely to be above an oncoming aircraft, X = 0.5 m and Y = 0 m (directly behind), and X = 0 m and Y = -0.5 m (directly below) serve as a good median for comparing individual SPLs. These are presented in Figure 4.2.2 and Figure 4.2.3, respectively, however the trends observed aft of the airfoil are primarily discussed. Tonal noise is reduced at lower frequencies, contributing to the majority of noise reduction at an AoA = 0°. Significant improvements begin at approximately 800 Hz for the highest AoA, with a reduction in both broadband and tonal noise. As shown by the OASPL figures, the 3.3% d/D maintains the most reduction on average out of the three depths. The consequences of the eddy break-up are then visible above 7000 Hz when behind the airfoil. At these higher frequencies there is an increase in tonal noise. As the eddies are now of a finer scale, after being broken up by the dimples, the acoustic energy has been shifted towards these higher frequencies. This is still above the 2000-5000 Hz range where human hearing is most sensitive, however. Additionally, these higher frequencies are more easily dissipated. Dissipation can occur through propagation, as higher frequencies will use more of their energy when radiating away from the airfoil. Increasing the observer distance will reduce the impact on these high frequencies.

a) AoA = 0°

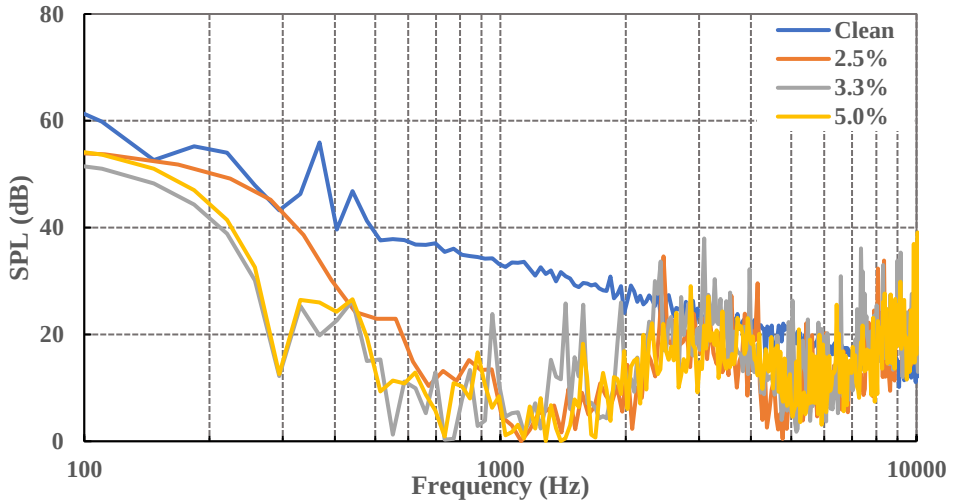

b) AoA = 3°

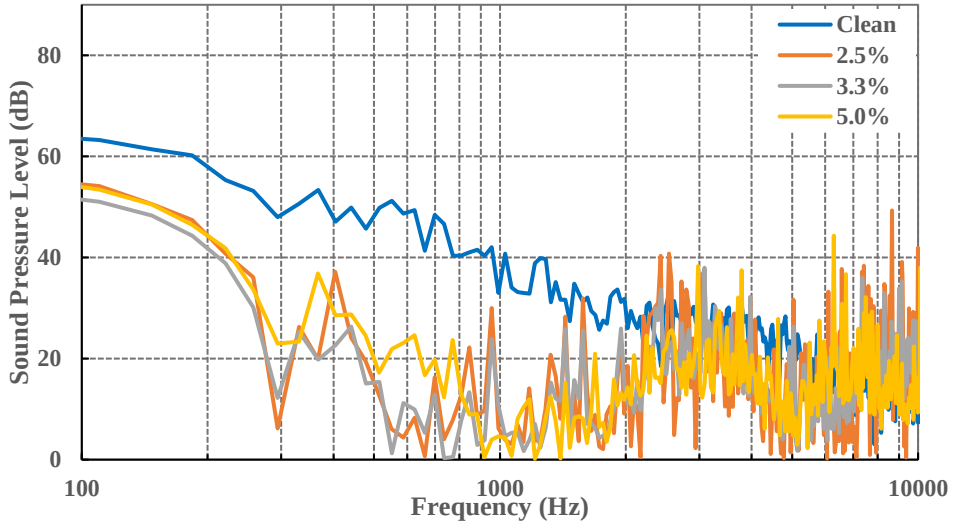

c) AoA = 6°

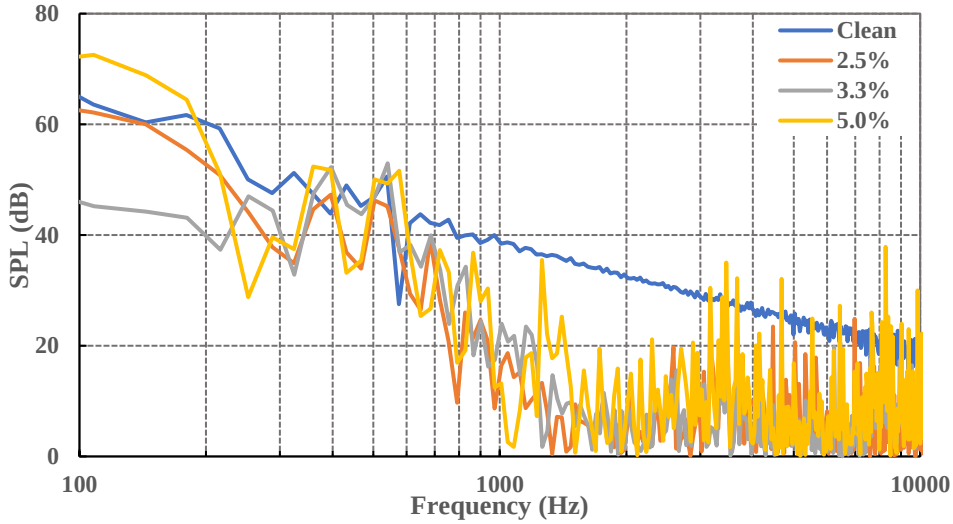

Figure 4.2.2: Sound Pressure Level at X = 0.5 m and Y = 0 m with Varying Dimple d/D at an a) AoA = 0° b) AoA = 3° and c) AoA = 6°

a) AoA = 0°

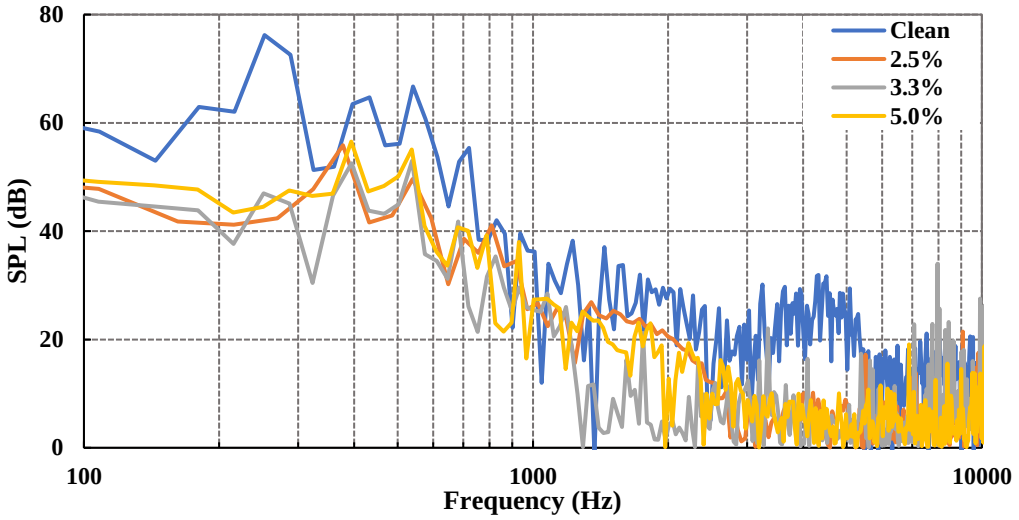

b) AoA = 3°

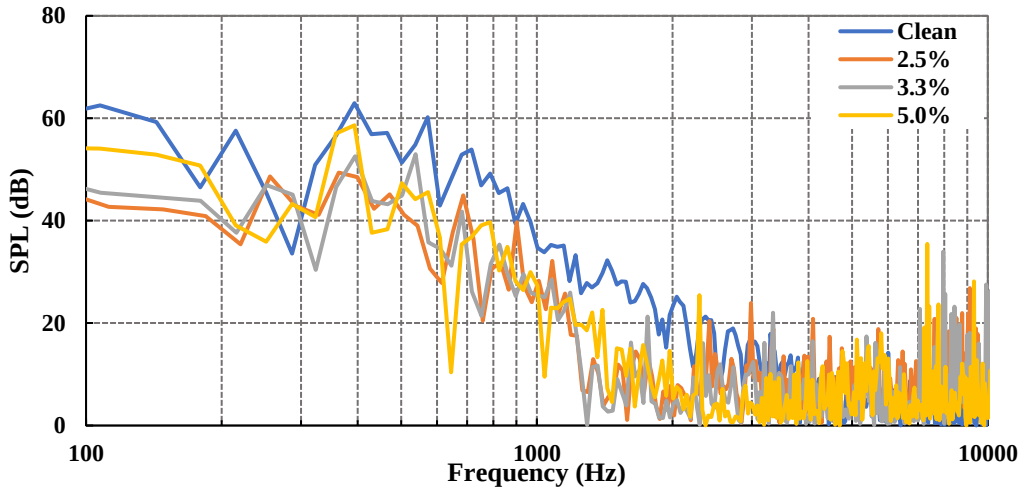

c) AoA = 6°

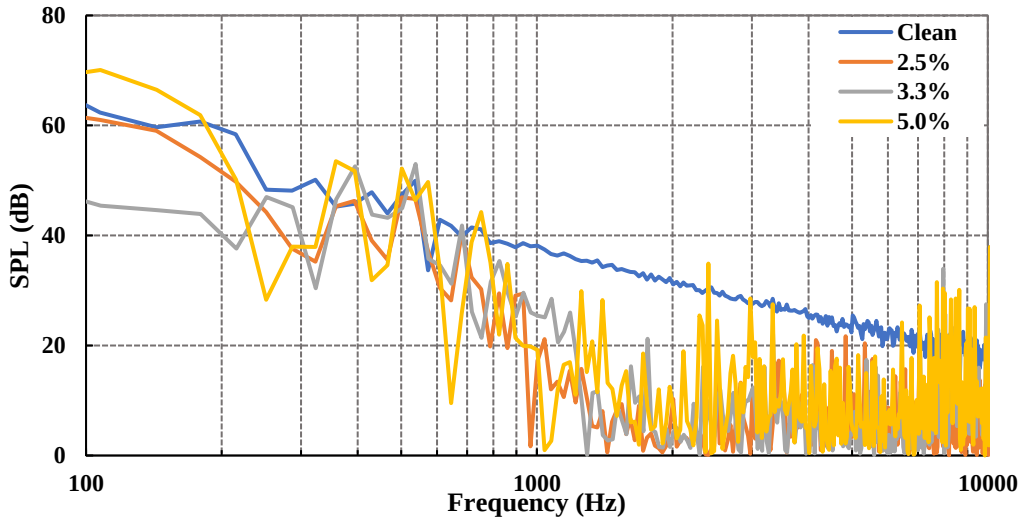

Figure 4.2.3: Sound Pressure Level X = 0 m and Y = -0.5 m Airfoil with Varying Dimple d/D at an a) AoA = 0° b) AoA = 3° and c) AoA = 6°

As the AoA increases, so does the effectiveness of the dimples. This can be seen aerodynamically, with a drag reduction at an AoA = 6° when compared to the penalty at an AoA = 0° and 3°. As such, their resultant oscillations begin to overpower the noise reduction caused by the eddy break-up as flow enters the dimples. Increasing the dimple d/D only serves to increase the oscillation magnitude, and subsequently the eddy break-up. As such, the mid to high frequencies are increased. These oscillations are needed, however, as they are the mechanism by which the eddies are broken up. This necessitates a balance in the boundary layer alteration, as the magnitude of the oscillations generated must be within a goldilocks zone. Due to this, a 3.3% d/D is the best depth ratio given the present conditions, as it showed the most reduction out of the three d/D tested.

4.3 Effect of Varying Array Size on Aerodynamics

As the 3.3% d/D was the optimum depth, varying the array size with this d/D is to be investigated. As mentioned in a previous section, arrays are defined by their starting location relative to the trailing edge of the airfoil. The investigated sizes begin 20% X/c, 33% X/c and 50% X/c from the trailing edge, which is visualized in Figure 4.3.1. Any notation of results is presented in this order as well. Subsequently, these cases are referred to as 20% DIM, 33% DIM and 50% DIM.

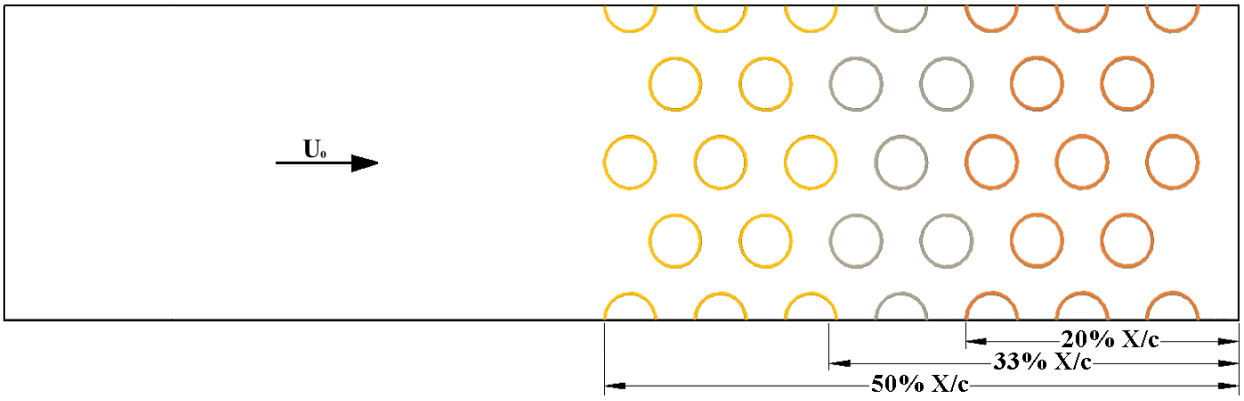

Figure 4.3.1: Comparison of Dimple Array Starting Location for 50% DIM (yellow) 33% DIM (grey) and 20% DIM (orange)

Directly comparing the lift between clean and dimpled cases yields no notable change at an AoA = 0° due to the symmetric airfoil and dimple application. Drag, however, increases with the array size implemented at 3.69%, 4.42% and 4.58%, respectively. This increase at 20% DIM is higher than the 1.9% reported by comparable literature, however the present cases do not make use of a BLT to force turbulent flow transition (Ananthan et al. 2022). As such, the dimples flow control effects are not as pronounced until an increase of AoA when the turbulent transition occurs earlier. Increasing to an AoA = 3°, as can be seen in Figure 4.3.2, yields a minor lift decrease of 0.11%, 0.36% and 0.59% for the respective cases, with drag increasing by 4.39%, 4.871% and 5.22%, respectively. Aerodynamic benefit is not seen until the AoA = 6°, where a slight drag reduction of 1.38%, 1.32% and 1.18% is seen for the respective cases. Lift is reduced, though the magnitude of this change is only 0.10% on average and as such is not considered significant. The application of dimples on both sides of the airfoil is the cause of such little lift impact, aside from their minimal flow effect due to the shallow depth. Any decrease in pressure on one side is roughly matched by the other. The flow across the dimples is symmetrical chordwise, but not spanwise. The foremost half a dimple has reduced pressure when compared to the aft half, which is visible in Figure 4.3.3. The equation for pressure coefficient is as follows:

$$C_p = \frac{p - p_0}{0.5 \cdot \rho U_0^2} \qquad 4.3.1$$

where p is local pressure, p_0 is freestream pressure, ρ is fluid density and U_o is the freestream velocity. As such, the increase in drag is caused by unsymmetrical pressure distribution within the dimples. Increasing the number of dimples increases this pressure disparity, resulting in an increase in drag. The favorable pressure gradient caused by a NACA 0012 likely plays a role in overpowering the drag reduction effects of the dimples and is also suggested by literature (van Nesselrooij et al. 2016; P. R. Spalart et al. 2019; C.M.J. Tay, Khoo, and Chew 2015).

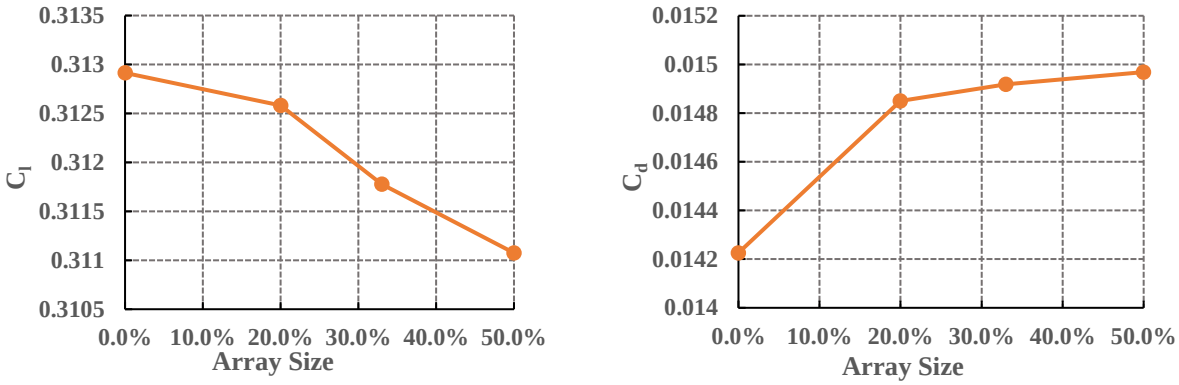

a) Lift at an AoA = 3° b) Drag at an AoA = 3°

Figure 4.3.2: Lift and Drag as a Function of Array Size for an AoA = 3°

Table 4.3.1: Lift and Drag Coefficients for all Cases

	Clean		20% DIM		33% DIM		50% DIM	
AoA (°)	C_l	C_d	C_l	C_d	C_l	C_d	C_l	C_d
0	4.18E-06	0.0131	3.26E-05	0.0136	-1.82E-05	0.0137	-4.22E-05	0.0137
3	0.313	0.0142	0.313	0.0149	0.312	0.0149	0.311	0.0150
6	0.614	0.0190	0.615	0.0187	0.614	0.0187	0.614	0.0188

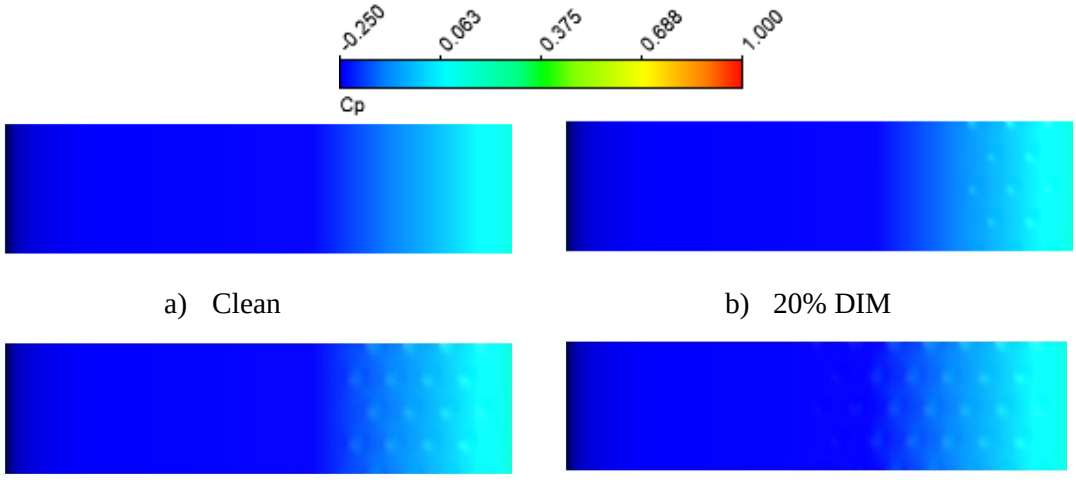

a) Clean b) 20% DIM

a) 33% DIM b) 50% DIM

Figure 4.3.3: Top-Down View of Pressure Coefficient on Airfoil Surface at an AoA = 3° for a) Clean b) 20% c) 33% and d) 50% DIM

In Figure 4.3.4, the average velocity of the flow around the airfoil can be seen. While at an AoA = 0°, the flow accelerates evenly on both upper and lower surfaces once past the leading edge. Aft of the airfoil is a small wake as the turbulent flow transition is late on a clean NACA 0012. As such, little turbulence can propagate to the trailing edge, and subsequently the wake. At an AoA = 0°, the flow is symmetrical as expected for a NACA 0012 airfoil. The trailing edge wake shows minor differences. It is not until Figure 4.3.5 that differences between the cases can be seen. Fluid upstream of the dimple must decelerate to enter the dimple, emerging out with a loss of momentum. This results in a thicker layer of slower moving fluid close to the surface of the airfoil. This matches closely with the authors in (Ananthan et al. 2022), though not as pronounced due to the increase in fluid velocity reducing viscous effects. As such, the fluid is less able to contour to the curvature of the dimples as well, though no flow separation occurs.

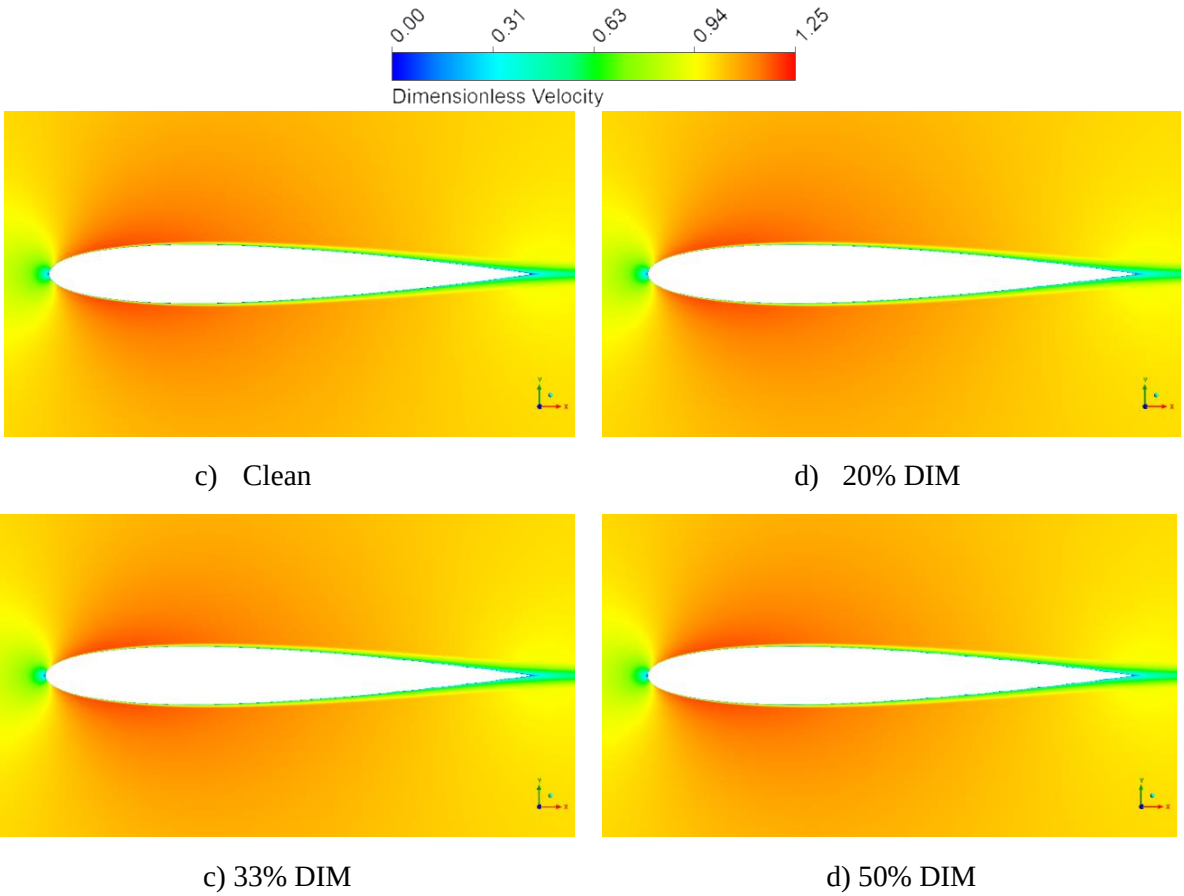

Figure 4.3.4: Time Averaged Velocity Flow Field Around a) Clean, b) 20% DIM, c) 33% DIM and c) 50% DIM

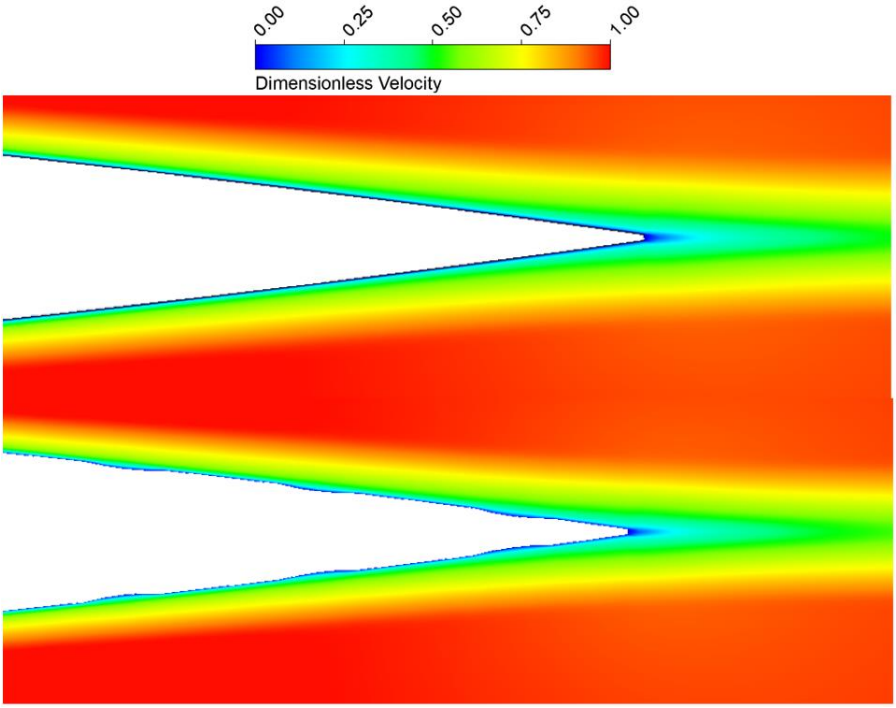

Figure 4.3.5: Trailing Edge Dimensionless Velocity Contour of Clean (Top) and 20% DIM (Bottom)

Increasing to an AoA = 3° shows the flow across the upper surface is faster than that of the flow across the bottom, which is reflected in the lift increases at these two AoAs. There is little overall differences in the velocity flow field that can be observed when comparing the clean and dimpled cases. With a positive AoA, the slower air across the bottom surface of the airfoil decreases Re_D and increases their effect in the near-wall flow. This is quickly overpowered by a strong favorable pressure gradient. As such, dimples located on the pressure side of an airfoil have marginal effects on the overall performance, especially considering the reduced importance of flow on this surface when compared to the suction side of an airfoil. The upper surface shows more alteration to the boundary layer when compared to the lower, though this difference is marginal. Further increasing to an AoA = 6°, it increases the relative curvature the air must contour to over the upper surface. As such, velocity discrepancy between the upper and lower surface is greater, increasing the turbulent wake as the two flows must mix.

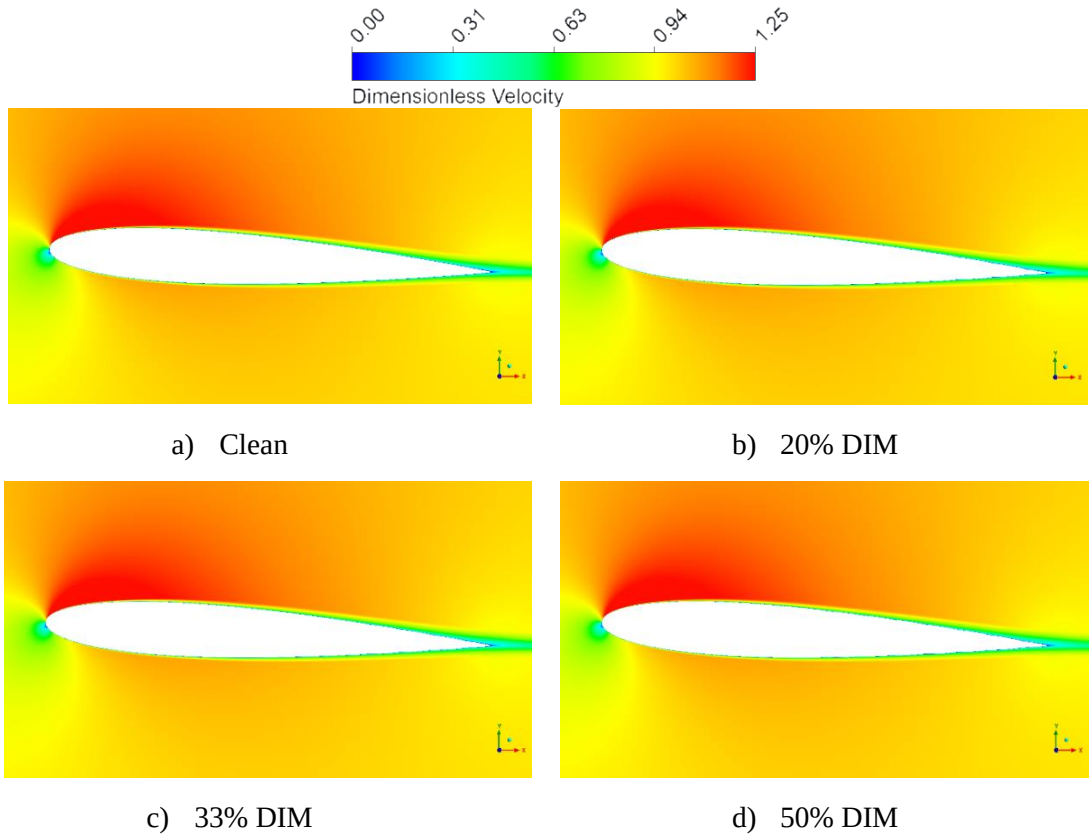

a) Clean

b) 20% DIM

c) 33% DIM

d) 50% DIM

Figure 4.3.6: Dimensionless Velocity at an AoA = 3° for a) Clean, b) 20% DIM, c) 33% DIM and c) 50% DIM

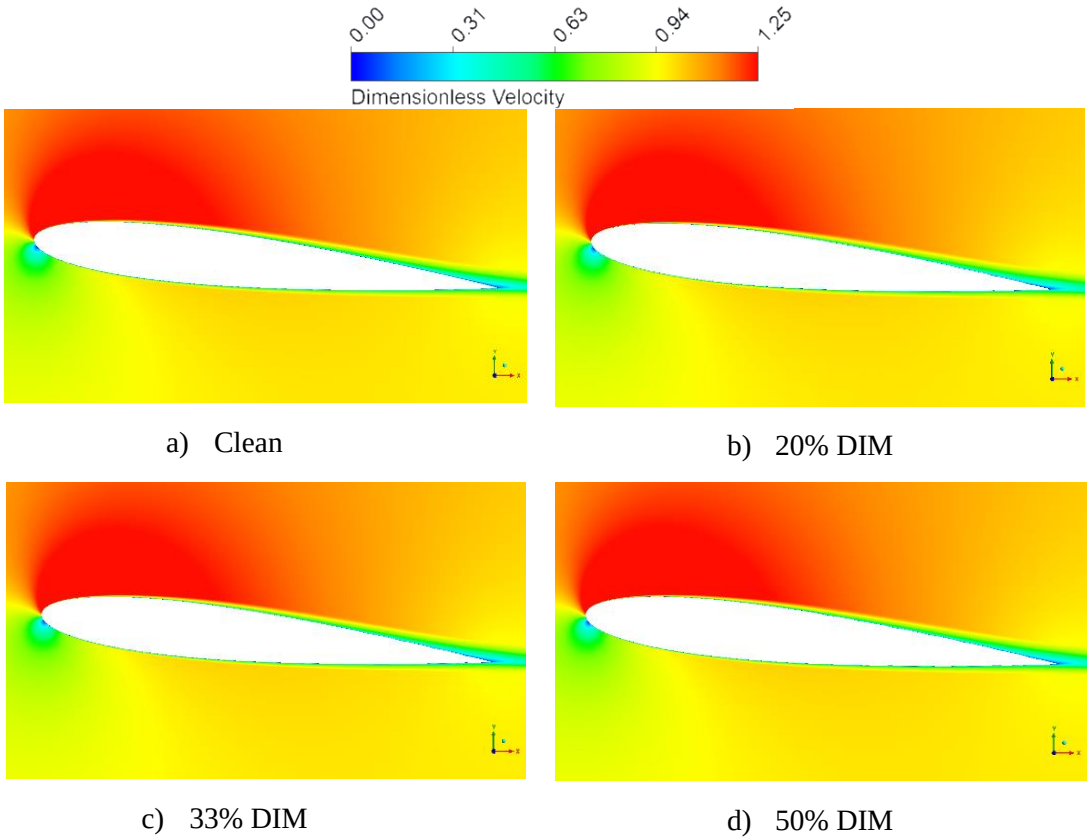

a) Clean

b) 20% DIM

c) 33% DIM

d) 50% DIM

Figure 4.3.7: Dimensionless Velocity at an AoA = 6° for a) Clean, b) 20% DIM, c) 33% DIM and c) 50% DIM

The deceleration-acceleration is visible when comparing the skin friction of the airfoils. For completeness, and comparative sake, the clean airfoil's skin friction is shown in Figure 4.3.8. This, however, closely matches the skin friction before and along the chord line in-between dimples, and as such is not added to the overall comparison to improve clarity.

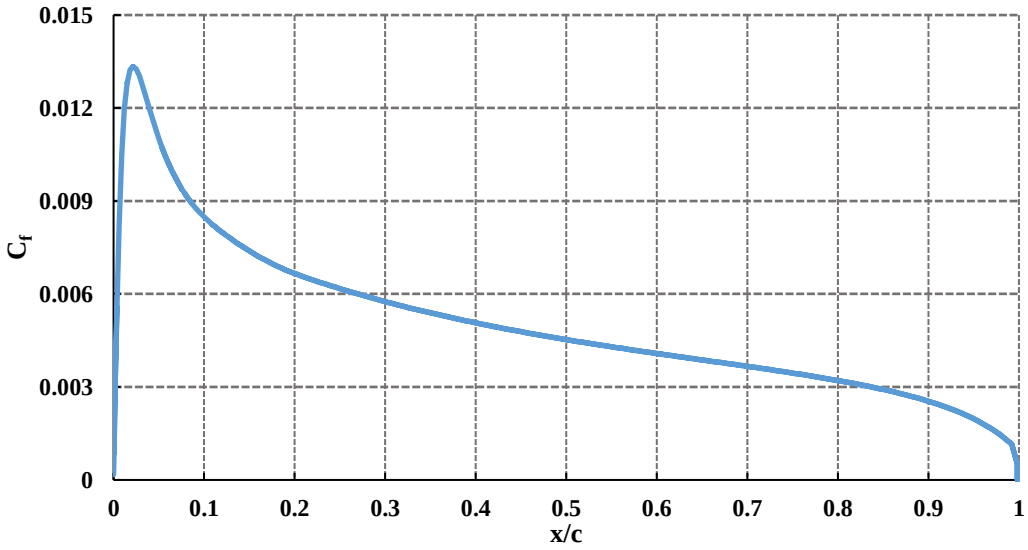

Figure 4.3.8: Skin Friction Plot for Clean Airfoil at an AoA = 0°

Skin friction is shown in three chordwise profiles along the airfoils. From left to right the middle row, between rows and center row are all visualized in Figure 4.3.9. For each case, these three profiles are plotted for the upper surface of the airfoil only.

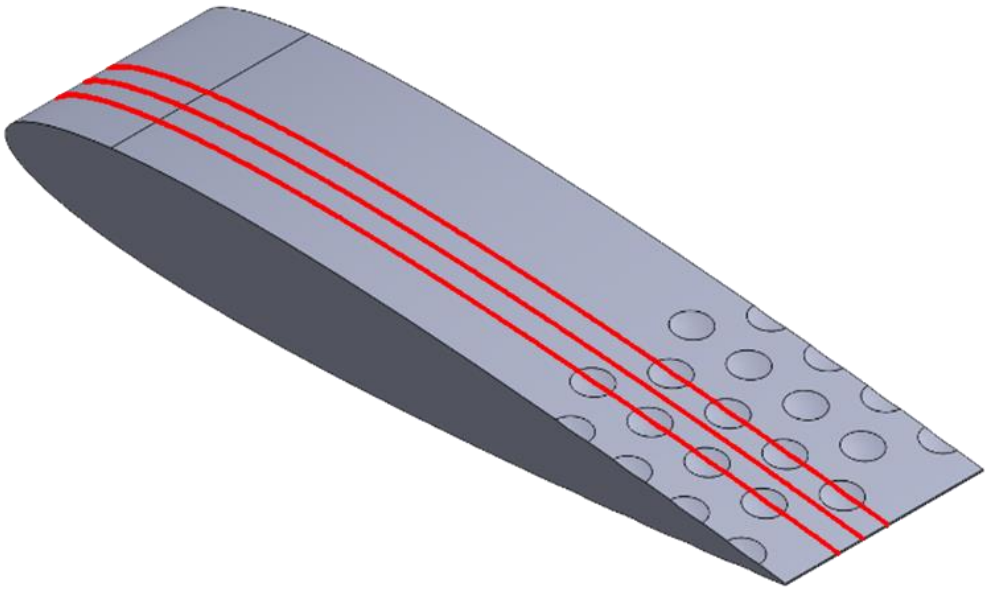

Figure 4.3.9: Chordwise Profile Locations on the 33% DIM Airfoil

From Figure 4.3.10, a notable decrease in skin friction occurs as the flow enters a dimple, correlating to a decrease in velocity. Conversely, a sharp increase in skin friction as the fluid begins to exit the dimple signifies an acceleration of the fluid. This deceleration-acceleration behavior matches that reported by the authors in (van Campenhout et al. 2018), even at a higher Reynolds number. Additionally, a net loss of skin friction occurs when compared to the clean case.

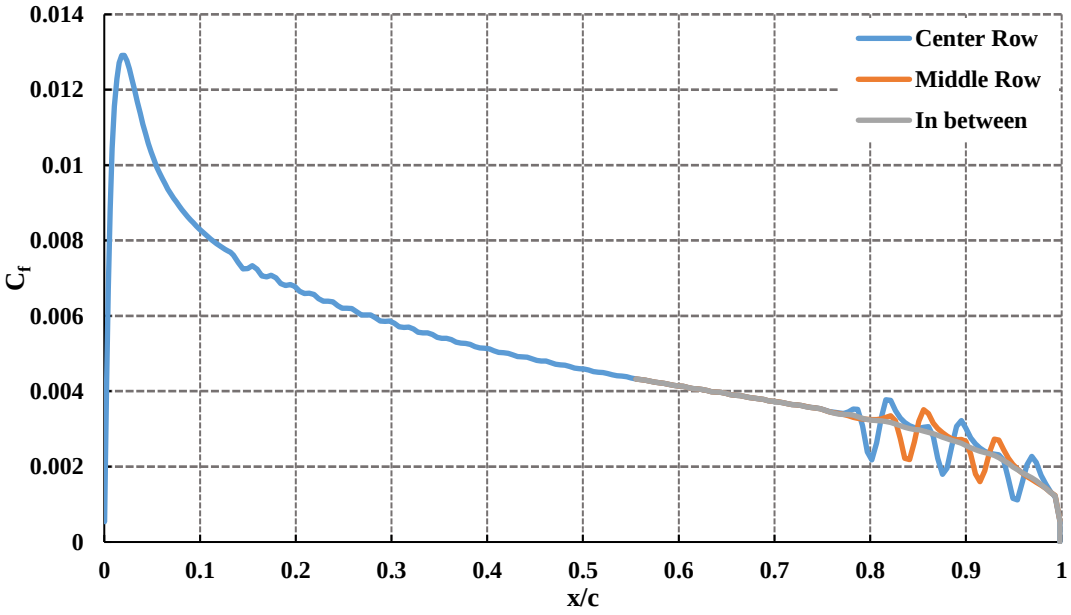

Figure 4.3.10: Skin Friction Plot for 20% DIM at an AoA = 0°

Near identical behavior is seen in the other dimpled cases, with their respective sections highlighted in Figure 4.3.11. This deceleration-acceleration phenomenon is crucial for the drag and noise reduction mechanisms as it allows for the converging-diverging flow across the dimple. The magnitude of skin friction oscillation can be seen to decrease as the number of dimples increases, suggesting diminishing effects. This is notable due to several authors concluding that more surface coverage of shallow dimples leads to more drag reduction on flat plates (van Nesselrooij et al. 2016; C.M. Tay 2011; C.M.J. Tay, Khoo, and Chew 2015).

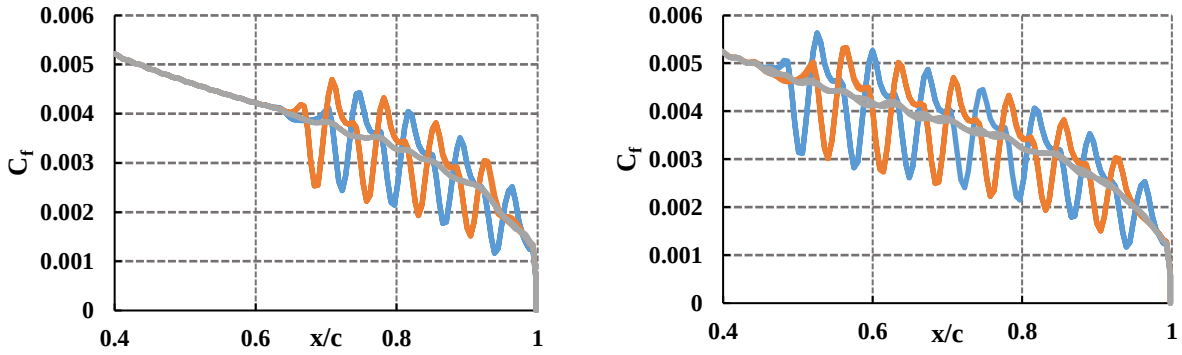

Figure 4.3.11: Skin Friction Plots for 33% DIM (Left) and 50% DIM (Right)

The oscillations can be further visualized with streamlines colored to the velocity in the Z direction in Figure 4.3.12. Here the spanwise oscillations can be seen extending past the trailing edge into the wake. Logically, the cases with more dimples produce stronger oscillations that persist at least 70% X/c past the trailing edge. While potentially aerodynamically beneficial, this is likely not beneficial for aeroacoustics. As velocity oscillates, so will pressure causing sound to be propagated. These oscillations can be beneficial, however, in reducing the peaks of chordwise velocity oscillations (Ananthan et al. 2022). Additionally, larger structures with the scale of the dimple or smaller can enter the dimple to be broken up. This break-up will result in higher frequency eddies persisting, shifting the energy to higher frequencies.

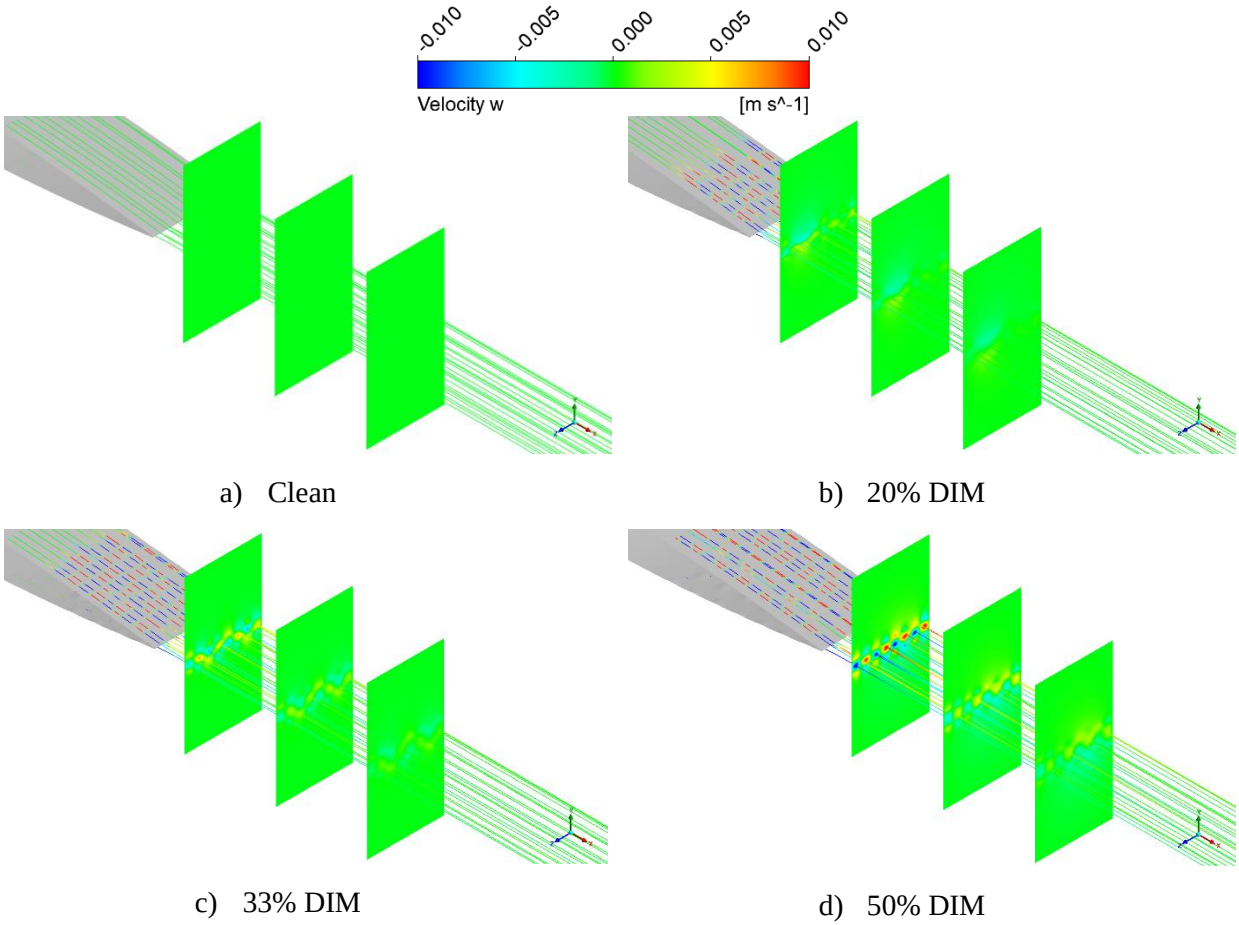

a) Clean

b) 20% DIM

c) 33% DIM

d) 50% DIM

Figure 4.3.12: Streamlines Along Upper Surface and Spanwise Velocity 0.1c, 0.4c and 0.7c from the Trailing Edge

The spanwise shear input by these oscillations into the fluid can be observed from the wall shear on the airfoil. The wall shear in the z direction is plotted on the surface of the airfoil in Figure 4.3.13. As expected, the clean airfoil shows no spanwise changes as little spanwise flows occur for a near-infinite airfoil. The 50% DIM array shows the most spanwise shear, though this decreases steadily again showing the reduced effects of more dimples. Exciting the fluid in this lateral direction is an analog to active wall oscillation or riblets (C.M. Tay 2011).

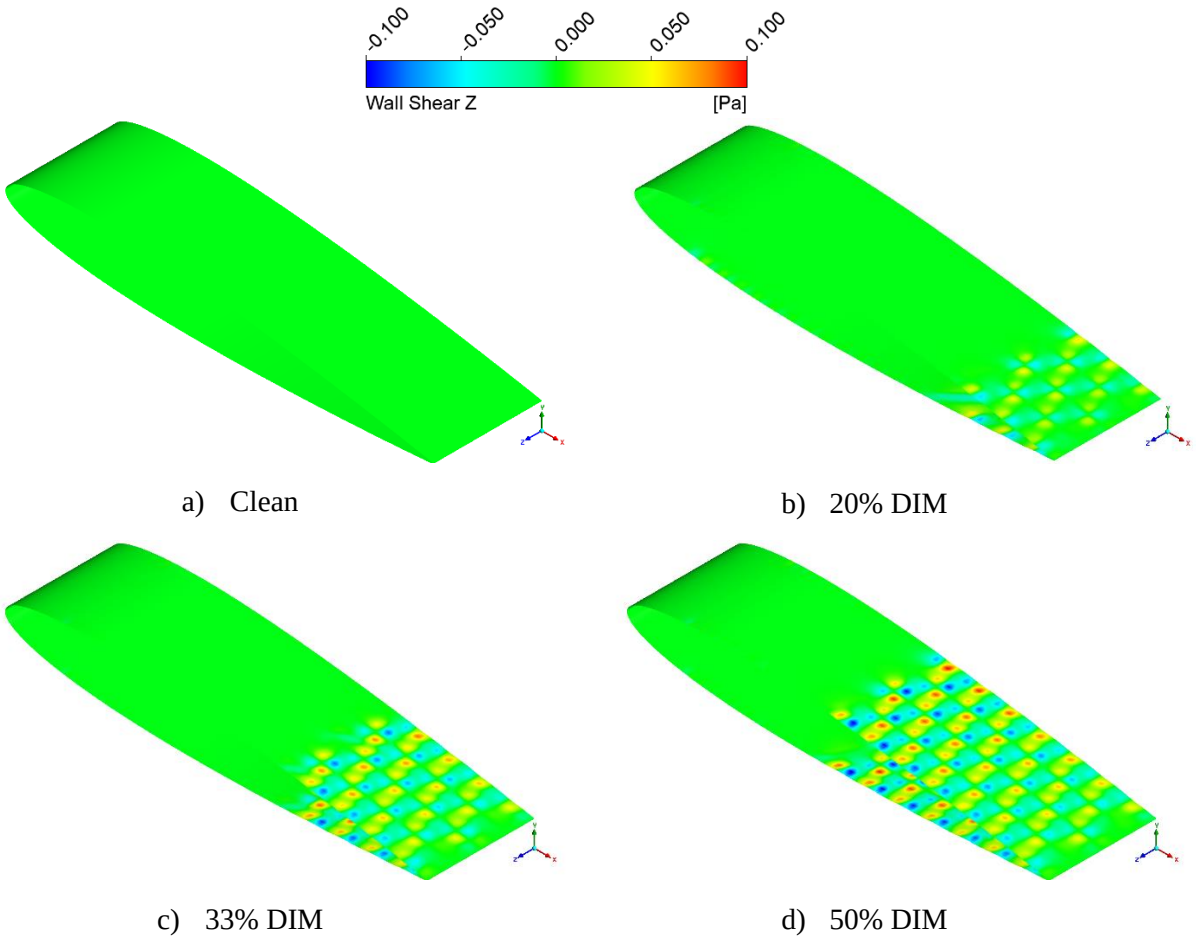

a) Clean b) 20% DIM

c) 33% DIM d) 50% DIM

Figure 4.3.13: Wall Shear in the Z Direction at an AoA = 0° on a) Clean b) 20% DIM c) 33% DIM and d) 50% DIM Arrays

No reversed flow is observed in the streamlines in Figure 4.3.14, further confirming the assumptions made from observing skin friction. The shallowness limits the flow reversal due to maintaining a higher velocity across its surface than a dimpled vortex generator. Reduced oscillation magnitude is seen when compared to deeper dimples from comparable literature (van Campenhout et al. 2018; van Nesselrooij et al. 2016). Vorticity is related to the curl of the velocity field, and as both velocity and its gradient are small so is vorticity (Lee et al. 2021). As such, vorticity generation is not significant, resulting in less drag during pre-stall AoAs when compared to vortex generators (Fouatih et al. 2016). This also results in a near steady flow behavior across the dimples, which can simplify computational demands as a transient simulation is not critical (Etter 2007). Similarly, the converging-diverging pattern induces spanwise shear

into the near-wall boundary layer which can play a role in reducing Reynolds stresses (Etter 2007). By inducing shear into the fluid, the lower portion of the boundary layer becomes a 'fluid dynamic ball bearing' (Kiknadze et al. 2006). The magnitude of these oscillations is minuscule, however, and rapidly decreases with height as it is quickly overpowered by the freestream and pressure gradients as seen in Figure 4.1.4a.

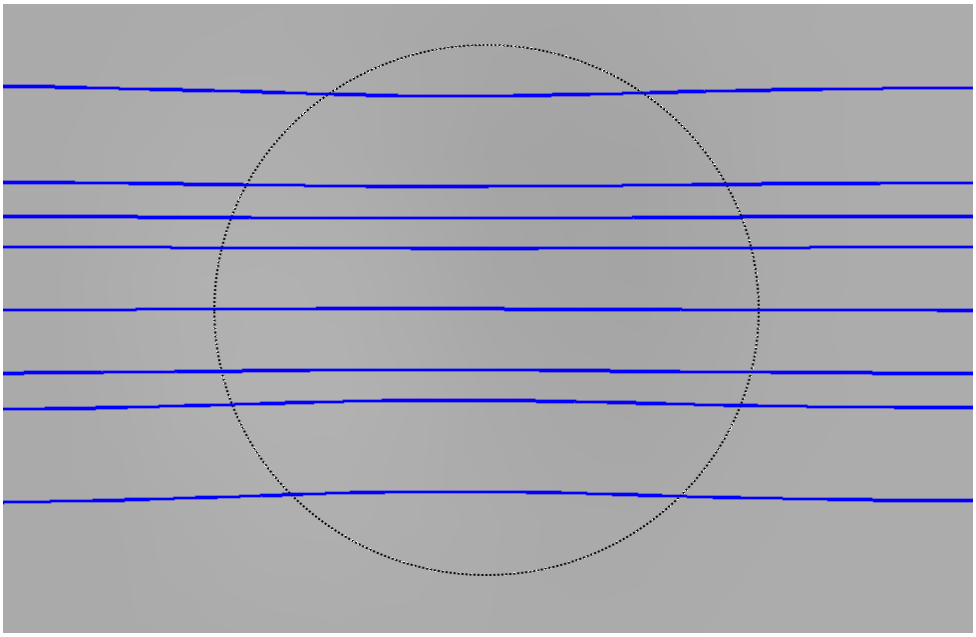

Figure 4.3.14: Top-Down View of Streamlines Across a Single Dimple at an AoA = 0°

To better view the turbulent structure break-up caused by the dimples, the isosurface of Q-Criterion can be used as seen in Figure 4.3.15. Q-Criterion define areas where the vorticity magnitude is greater than the strain rate, as can be seen in Equation 4.3.2:

$$Q = \frac{1}{2}(\|\Omega\|^2 - \|S\|^2) \qquad 4.3.2$$

where Ω is the rotation rate, or vorticity tensor, and S is the strain rate tensor. Q-Criterion can be used to visualize vortical structures and are normalized to dimensionless velocity. Eddies with a scale of the dimples or smaller can be seen decelerating in and accelerating out of the dimples, further showing the importance of this effect. This action breaks up the eddies into finer structures visible at the trailing edge of the dimpled case.

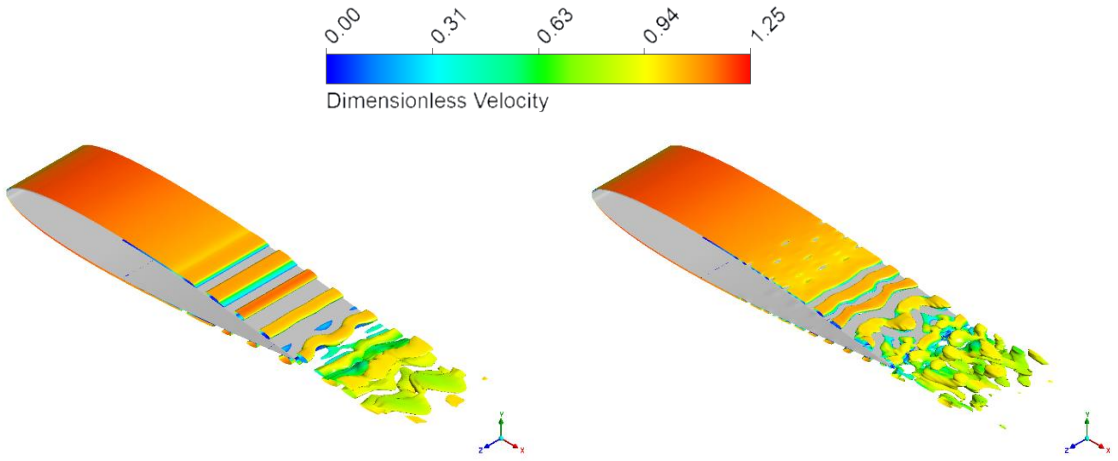

a) Clean b) 50% DIM

Figure 4.3.15: Instantaneous Isosurface of Q-Criterion Normalized to Dimensionless Velocity of Clean (Left) and 50% DIM (Right) at an AoA = 0°

When increasing to an AoA = 3°, turbulent transition can be seen to begin at approximately 22% on the clean airfoil in Figure 4.3.16 where the isosurface of Q-criterion is normalized to dimensionless velocity. Further upstream effects can be seen, delaying the start of this transition to as much as 45% in the 50% DIM array. The dimples break up the larger structures which will have significant impact on the acoustic propagation of the turbulent boundary layer. At the trailing edge especially, finer structures are visible with decreasing scale as more dimples are implemented. The 20% DIM in particular maintains spanwise coherence in several vortical structures immediately aft of the trailing edge, which are broken up by the 30% DIM and 50% DIM arrays.

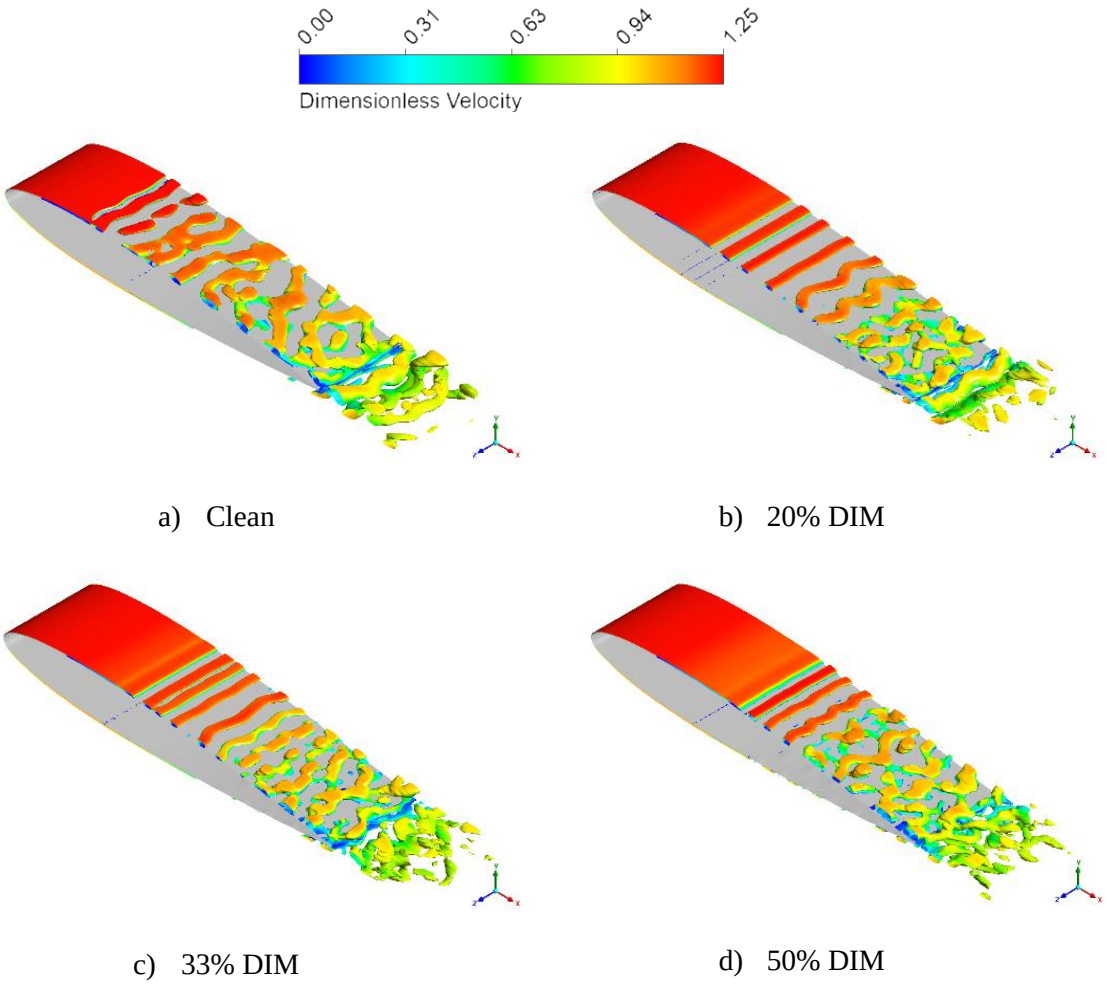

a) Clean

b) 20% DIM

c) 33% DIM

d) 50% DIM

Figure 4.3.16: Isosurface of Q-Criterion at an AoA = 3° on a) Clean b) 20% DIM c) 33% DIM and d) 50% DIM Arrays

4.4 Effect of Varying Array Size on Aeroacoustics

As the resulting flow field has been analyzed, the results for far-field acoustics can be considered. When comparing OASPL for all cases at an AoA = 0°, a reduction of approximately 7 dB is seen at X = 0 m and Y = $\mp$0.5 m. Again, symmetrical values are found here due to the airfoil chosen and application of dimples on either side. In the wake, X = 0.5 m and Y = 0 m, a decrease of 3.74 dB for the 33% DIM array is visible. This was the best performing array size in most cases, regardless of AoA as it can be seen in Figure 4.4.1. At an AoA = 3°, the 20% DIM and 33% DIM arrays are the only arrays that show a notable

decrease in acoustics. The 20% DIM array is not as effective at mitigating acoustic emissions, however, when compared to the 30% DIM array. The 50% DIM, on the other hand, shows nearly the same performance acoustically when compared to the clean case at this AoA. This is likely caused by the increased disturbance of the boundary layer as observed in the previous section, causing more noise propagation. This could also explain the reduced effectiveness of the 20% DIM array at this AoA, in essence not providing enough disturbances reduces the eddy break-up and has marginal effect acoustically. At an AoA = 6°, however, shows a reduction in all DIM arrays with the 50% DIM array yielding the most at 7.35 dB on average.

Table 4.4.1: OASLP Values at Select Receiver Locations at an AoA = 0° with Varying Array Size

Case	X = 0.5 m Y = 0 m (dB)	X = 0 m Y = 0.5 m (dB)	X = -0.5 m Y = 0 m (dB)	X = 0 m Y = -0.5 m (dB)
Clean	61.71	67.17	63.23	67.13
20% DIM	58.48	60.27	60.11	60.29
33% DIM	57.97	58.61	58.44	58.49
50% DIM	60.93	57.23	58.95	57.32

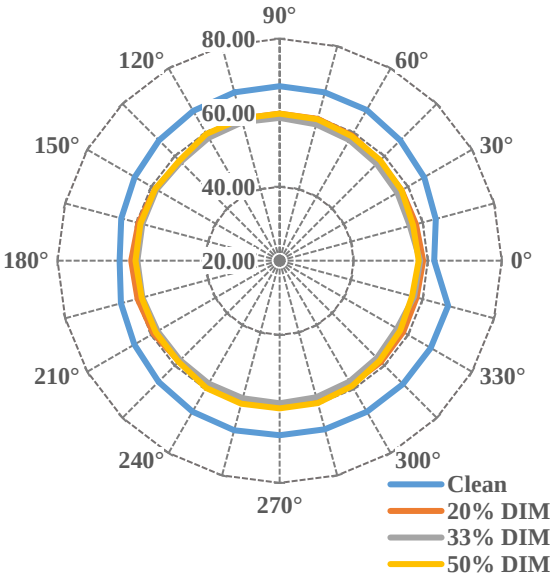

a) AoA = 0°

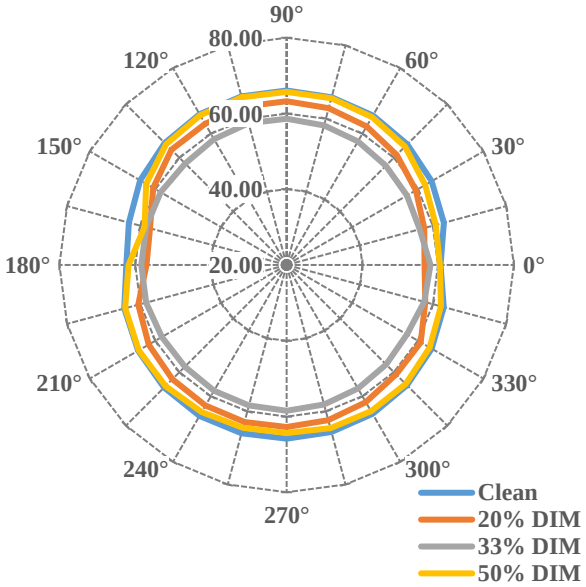

b) AoA = 3°

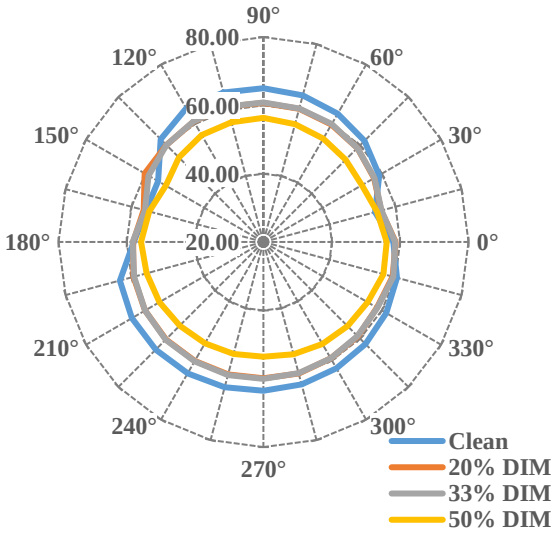

c) AoA = 6°

Figure 4.4.1: OASPL of Varying Dimple Array Sizes at an a) AoA = 0° b) AoA = 3° and c) AoA = 6°

To further visualize the aeroacoustic impact of the shallow dimples, the SPLs are plotted in Figure 4.4.2 and Figure 4.4.3 for X = 0.5 m and Y = 0 m (directly behind), and X = 0 m and Y = -0.5 m (directly below), respectively. Given the satisfaction of Blake's criteria, tonal noise for the clean airfoil is expected. A prominent frequency at 367 Hz is visible in Figure 4.4.2 which is directly behind the airfoil. At this location, the highest fluctuations in pressure caused by the vortex shedding are expected as it is immediately within the wake of the airfoil. The eddy break-up can be seen shifting energy towards higher frequencies, which is visible in all SPLs. The 50% DIM array shows increased efficiency in shifting these eddies towards higher frequencies at an AoA of 0°. Efficiency of this shift reduces as AoA increases when compared to the other depths. This can be seen as the 20% DIM and 33% DIM arrays overtake the 50% DIM array from 2,000 Hz to 5,000 Hz aft of the airfoil. The 20% DIM array is not as effective in reducing the low frequencies, however, and as such the 33% DIM array is the favored configuration.

a) AoA = 0°

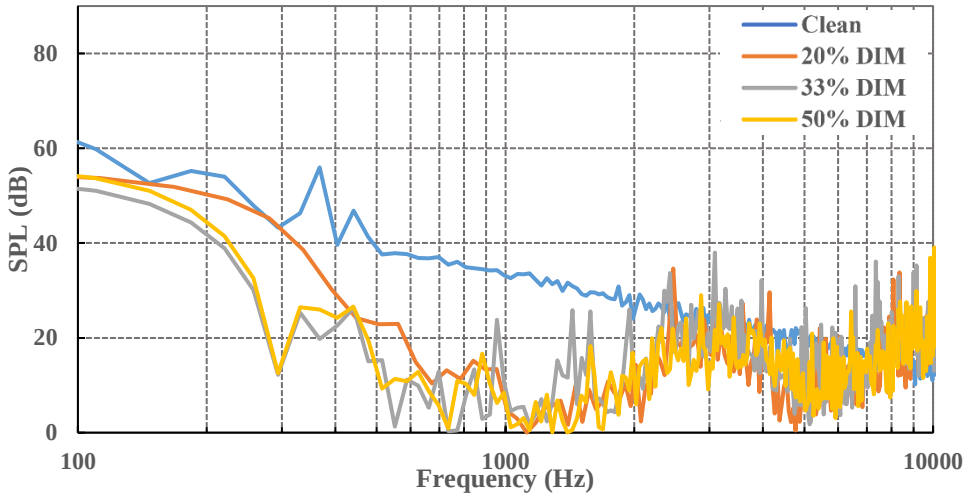

b) AoA = 3°

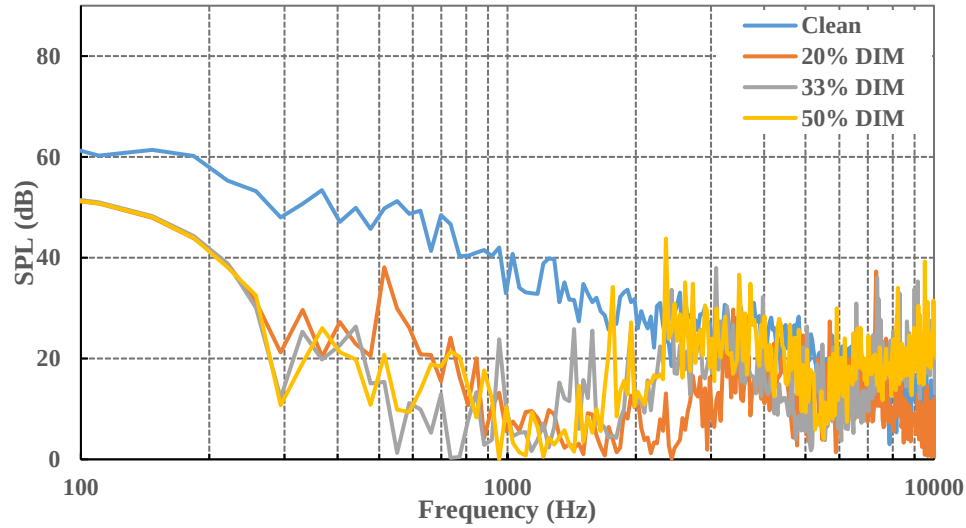

c) AoA = 6°

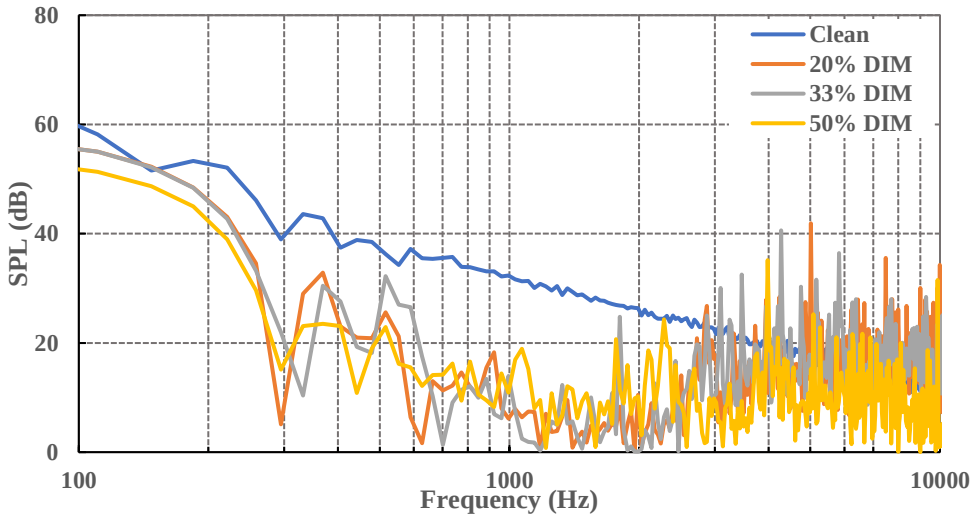

Figure 4.4.2: Sound Pressure Level X = 0.5 m and Y = 0 m with Varying Array Size at an a) AoA = 0° b) AoA = 3° and c) AoA = 6°

a) AoA = 0°

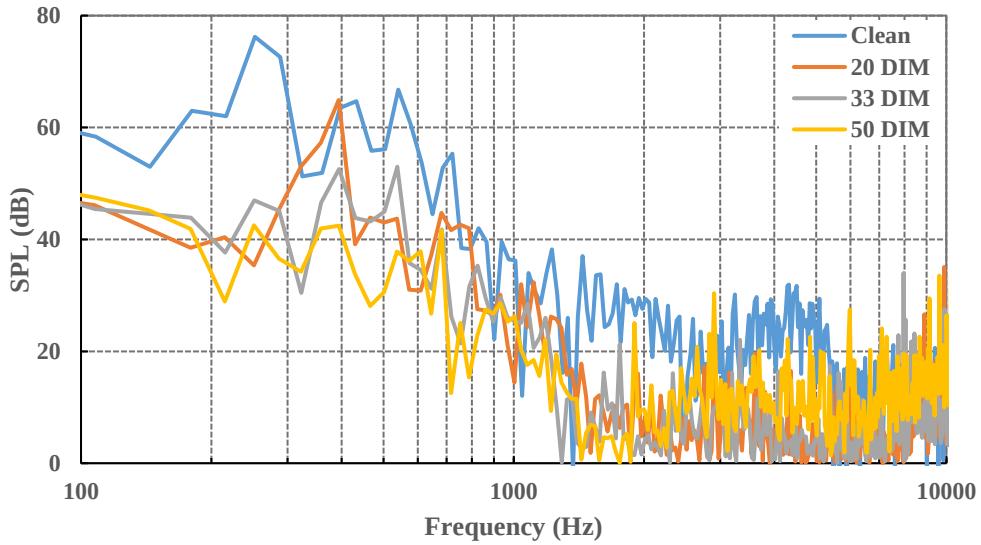

b) AoA = 3°

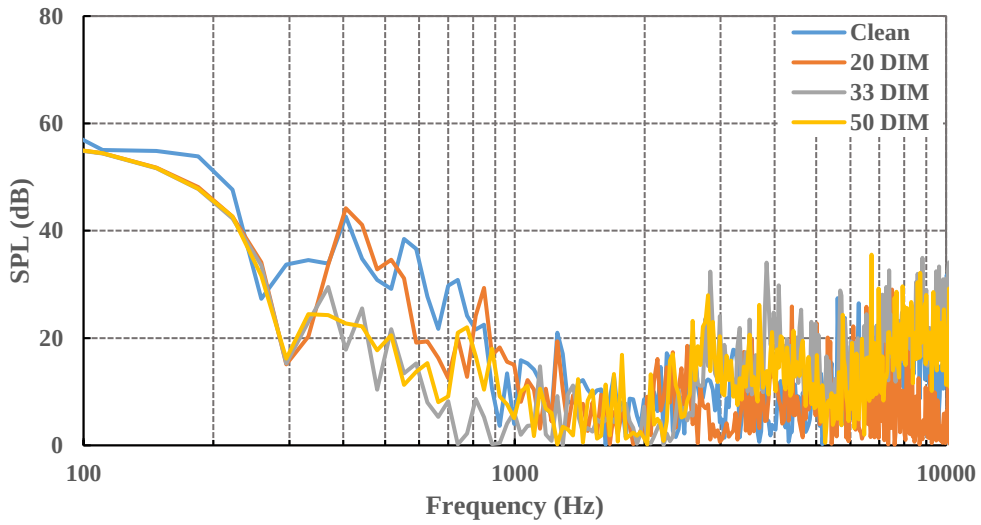

c) AoA = 6°

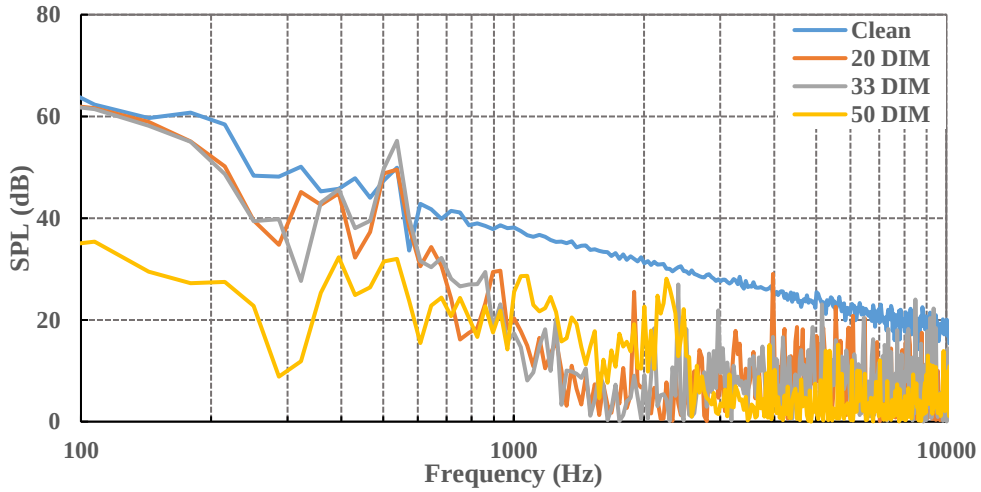

Figure 4.4.3: Sound Pressure Level X = 0 m and Y = -0.5 m with Varying Array Size at an a) AoA = 0° b) AoA = 3° and c) AoA = 6°

CHAPTER 5

CONCLUSION

The aerodynamic and aeroacoustic impact of very shallow dimple arrays on the upper and lower surfaces of an airfoil was investigated. At a $Re = 4.8 \times 10^5$, marginal aerodynamic penalties were found. A maximum drag reduction of 1.31% was found for a 3.3% d/D dimple array covering the latter 33% X/c of a NACA 0012 airfoil at an AoA = 6°. Flow across the airfoil in the chordwise direction was found to decelerate into the dimples and accelerate out. This causes a converging diverging pattern which induces spanwise fluctuations in the flow producing an effect like that of riblets or wall oscillations. Spanwise coherence is broken up by these oscillations, and eddies with a scale smaller than the dimple diameter are dispersed. As suggested by literature, these oscillations produce a 'fluid dynamic ball bearing' effect on the flow traveling above reducing friction drag (Kiknadze et al. 2006). However, pressure drag increases due to the unsymmetrical pressure within the dimples. The reduction in friction drag, however, limits the impact of this increase. As these shallow dimples are significantly easier for manufacturing and maintenance, especially when compared to riblets, this method of shallow dimples shows potential as a means of drag reduction.

Acoustically, significant reductions were achieved with the implementation of shallow dimples. The boundary layer is likely not fully resolved, due to computational limitations, which reduces the effectiveness of this assessment. The spanwise oscillations caused by shallow dimples have drastically less aeroacoustic penalties when compared to the vortex generators of literature (Kolkman et al. 2018). An optimal d/D of 3.3% was determined, as any deeper produced stronger oscillations and eddy break-up than desired. The shallowest depth, 2.5% d/D, showed slightly worse acoustic performance when compared to the 3.3% d/D at an average difference of 1.14 dB. The 5% d/D was found to have marginal noise reduction at an AoA = 6°, resulting in the 3.3% d/D being favored. Conversely varying the array size was found to have a similar effect, necessitating a balance between flow alteration and eddy break-up. The 20% DIM

array showed the least aerodynamic impact, but also the least acoustic impact. The 50% DIM array increased noise propagation when compared to a clean airfoil at an AoA = 3°, making this configuration less enticing when compared to the constant OASPL reduction of the 33% DIM array.

Based off the presented work, an array covering the latter 33% of the airfoil with a 3.3% d/D ratio is optimal for reducing the aeroacoustic noise propagation. This decision is made to fulfill the criteria of a 5 dB OASPL reduction with less than a 5% increase in drag. All AoAs evaluated satisfied this criterion, with an average drag increase of 2.66% and an average OASPL reduction of 5.75 dB. Areas below the airfoil showed the most improvement, with as much as 6.84 dB in OASPL reduction at X = 0 m and $Y = -0.5$ m. Trailing edge wake noise was also reduced by as much as 3.74 dB. As such, an array of shallow dimples on the trailing edge of an airfoil can be an effective means for reducing aeroacoustic noise emission.

5.1 Future Recommendations

Although a slight improvement in drag was observed at an AoA = 6°, this can be further improved through optimization of the dimple geometry. Only six depths were assessed, with the 3.3% d/D showing the most favorable performance. This d/D, however, may not yield optimal performance, as observed by the drag penalty at an AoA = 0° and 3°. This is supported by literature, where a 2.5% < d/D < 10% is referenced (van Campenhout et al. 2018; van Nesselrooij et al. 2016; P. R. Spalart et al. 2019). Although a deeper dimple will lead to an increase in drag at moderate AoA, their more significant vorticity generation will improve near and post stall performance, which could also be investigated. This is supported by literature as well, where counter rotating vortices are observed within a deeper dimple (Etter 2007). Deepening the dimples will likely reduce the aeroacoustic benefits at moderate AoA as increasing the turbulent boundary layer is inherently counterintuitive to reducing noise from a turbulent boundary layer. Alternatively, the dimple arrangement on the surface could be altered as well. The present configuration was used with the assumption of best performance, as demonstrated by a variety of differing arrangements

on a flat plate (van Nesselrooij et al. 2016). Dimple radius will also alter the performance as suggested by literature (P. R. Spalart et al. 2019).

Another area of improvement is mesh refinement, particularly the y^+ value. While a structured mesh was used with low skewness and high orthogonality, it may not have been sufficient for the solver to fully resolve the boundary layer due to the low element count. This is critical as the turbulent boundary layer is the dominate source of aeroacoustic noise at lower AoAs. The two boundary layers merging at the trailing edge is critical to model, and as such any inaccuracies in the initial boundary layer formation will propagate downstream. Improvement of this sort will require significantly more elements, increasing runtime and computational power, which was the primary reasoning behind the current mesh. Therefore, a significant increase in computational power and runtime is required before the mesh can be refined.

Alternatively, a hybrid LES/RANS solver could be utilized. Detached Eddy Simulation (DES) has shown potential in aeroacoustic research (Michel et al. 2009). As the boundary layer is effectively an unsteady RANS model, the solver is not as dependent on the mesh fineness near the skin of the airfoil when compared to LES or DNS. A purely unsteady RANS simulation, however, has not been shown to accurately predict the aeroacoustic effects needed for such an investigation (Allen and Mendonca 2005). Therefore, either LES or DES should be used in future aeroacoustic studies.

REFERENCES

Al Tlua, Basim, and Joana Rocha. 2021. "Experimental investigation of NACA-0012 airfoil instability noise with sawtooth trailing edges." *Wind Engineering* 46 (3): 972-982. https://doi.org/10.1177/0309524x211060548.

Allen, Richard, and Fred Mendonca. 2005. "RANS and DES Turbulence Model Predictions of Noise on the M219 Cavity at M=0.85." *International Journal of Aeroacoustics*. https://doi.org/10.1260/1475472053730039.

Ananthan, V. B., R. A. D. Akkermans, T. Hu, P. Q. Liu, and N. Rathje. 2022. "Trailing-edge noise reduction potential of a locally applied shallow dimpled surface." *Journal of Sound and Vibration* 525. https://doi.org/10.1016/j.jsv.2022.116745.

Anderson, John. 2017. *Fundementals of Aerodynamics, Sixth Edition*. New York, NY: McGraw-Hill.

Anderson, John D. 2016. *Introduction to Flight, Eighth Edition*. New York, NY: McGraw-Hill.

ANSYS. 2011. *ANSYS FLUENT Theory Guide*. Canonsburg, PA: ANSYS, Inc. https://www.afs.enea.it/project/neptunius/docs/fluent/html/th/main_pre.htm.

Arbey, H., and J. Bataile. 1983. "Noise generated by airfoil profiles placed in a uniform laminar flow." https://doi.org/10.1017/S0022112083003201.

Arce León, Carlos, Roberto Merino-Martínez, Daniele Ragni, Francesco Avallone, Fulvio Scarano, Stefan Pröbsting, Mirjam Snellen, Dick G. Simons, and Jesper Madsen. 2017. "Effect of trailing edge serration-flow misalignment on airfoil noise emissions." *Journal of Sound and Vibration* 405: 19-33. https://doi.org/10.1016/j.jsv.2017.05.035.

Arcondoulis, Elias, Con J. Doolan, Anthony C. Zander, Laura A. Brooks, and Yu Liu. 2019. "An investigation of airfoil dual acoustic feedback mechanisms at low-to-moderate Reynolds number." *Journal of Sound and Vibration* 460. https://doi.org/10.1016/j.jsv.2019.114887.

Baldacchino, D, M Manolesos, C Ferreira, A Gonzalez Salcedo, M Aparicio, T Chaviaropoulos, K Diakakis, L Florentie, N R. Garc´ıa, G Papadakis, N N. Sørensen, N Timmer, N Troldborg, S Voutsinas, and A van Zuijlen. 2016. "Experimental benchmark and code validation for airfoils equipped with passive vortex generators." https://doi.org/10.1088/1742-6596/753/2/022002.

Baldacchino, Daniel, Carlos Ferreira, Delphine De Tavernier, W. A. Timmer, and G. J. W. van Bussel. 2018. "Experimental parameter study for passive vortex generators on a 30% thick airfoil." *Wind Energy* 21 (9): 745-765. https://doi.org/10.1002/we.2191.

Bappa, Mohammed. 2015. "Aerodynamic Sumilation of Vehicle Bodywork Design." Master's thesis, Teesside University. https://doi.org/10.13140/RG.2.2.16171.46884.

Bern, Marshall, and Paul Plassmann. 2000. "Mesh Generation." *Handbook of Computational Geometry*: 291-332. https://doi.org/10.1016/b978-044482537-7/50007-3.

Blake, William K. 2017. "Mechanics of Flow-Induced Sound and Vibration." *Mechanics of Flow-Induced Sound and Vibration* 1. https://doi.org/10.1016/b978-0-12-809273-6.00007-5.

Brooks, Thomas F., and Michael A. Marcolini. 1986. "Airfoil tip vortex formation noise." *AIAA Journal* 24 (2): 246-252. https://doi.org/10.2514/3.9252.

Cao, Huijing, Mingming Zhang, Chang Cai, and Ziliang Zhang. 2020. "Flow topology and noise modeling of trailing edge serrations." *Applied Acoustics* 168. https://doi.org/10.1016/j.apacoust.2020.107423.

Cao, Huijing, Teng Zhou, Liangwen Qi, and Mingming Zhang. 2022. "An experimental study of tonal noise from a wind turbine airfoil with flat plate serrations." *Applied Acoustics* 191. https://doi.org/10.1016/j.apacoust.2022.108664.

Cathers, Evan. 2021. "Comparative Analysis of Winglet Efficiency on Supercritical Versus Traditionally Cambered Airfoils." Master's Thesis, Georgia Southern University. https://digitalcommons.georgiasouthern.edu/cgi/viewcontent.cgi?article=3630&context=etd.

Chaitanya, Paruchuri, Phillip Joseph, Tze Pei Chong, Matthew Priddin, and Lorna Ayton. 2020. "On the noise reduction mechanisms of porous aerofoil leading edges." *Journal of Sound and Vibration* 485. https://doi.org/10.1016/j.jsv.2020.115574.

Chan, C.I., and R.C. Chin. 2021. "Investigation of the influence of miniature vortex generators on the large-scale motions of a turbulent boundary layer." *Journal of Fluid Mechanics*. https://doi.org/10.1017/jfm.2021.1013

Chen, Guoyong, Xiaoquan Yang, Xiaolong Tang, Jue Ding, and Peifen Weng. 2022. "Effects of slat track on the flow and acoustic field of high-lift devices." *Aerospace Science and Technology* 126. https://doi.org/10.1016/j.ast.2022.107626.

Choudhari, Meelan M., and David P. Lockard. 2015. "Assessment of Slat Noise Predictions for 30P30N High-Lift Configuration from BANC-III Workshop." 21st AIAA/CEAS Aeroacoustics Conference, Dallas, TX. https://doi.org/10.2514/6.2015-2844.

Critzos, Chris C., Harry H. Heyson, and Robert W. Boswinkle. 1955. "Aerodynamic Charecteristics of NACA 0012 Airfoil Section at Angles of Attach from 0° to 180°." https://ntrs.nasa.gov/citations/19930084501.

D'Alessandro, Valerio, Giacomo Clementi, Luca Giammichele, and Renato Ricci. 2019. "Assessment of the dimples as passive boundary layer control technique for laminar airfoils operating at wind turbine blades root region typical Reynolds numbers." *Energy* 170: 102-111. https://doi.org/10.1016/j.energy.2018.12.070.

Dahl, Kristian Skriver. 1997. "Aeroacoustic Computation of Low Mach Number Flow." Master's thesis, Technical University of Denmark. https://www.osti.gov/etdeweb/servlets/purl/426848.

De Tavernier, D., C. Ferreira, A. Viré, B. LeBlanc, and S. Bernardy. 2021. "Controlling dynamic stall using vortex generators on a wind turbine airfoil." *Renewable Energy* 172: 1194-1211. https://doi.org/10.1016/j.renene.2021.03.019.

Dean, B., and B. Bhushan. 2010. "Shark-skin surfaces for fluid-drag reduction in turbulent flow: a review." *Philos Trans A Math Phys Eng Sci* 368 (1929): 4775-806. https://doi.org/10.1098/rsta.2010.0201.

Dobrzynski, Werner. 2010. "Almost 40 Years of Airframe Noise Research: What Did We Achieve?" *Journal of Aircraft* 47 (2): 353-367. https://doi.org/10.2514/1.44457.

Du, Yiqing, V. Symeonidis, and G. E. Karniadakis. 2002. "Drag reduction in wall-bounded turbulence via a transverse travelling wave." *Journal of Fluid Mechanics* 457: 1-34. https://doi.org/10.1017/s0022112001007613.

Duell, Edward, Joel Walter, Steve Arnette, and Joseph Yen. 2004. "Boundary Layer Noise in Aeroacoustic Wind Tunnels." 42nd AIAA Aerospace Sciences Meeting and Exhibit, Reno, Nevada https://doi.org/10.2514/6.2004-1028.

Duell, Edward, Joseph Yen, Steven Arnette, and Joel Walter. 2002. "Recent Advances in Large Scale Aeroacoustic Wind Tunnels." 8th AIAA/CEAS Aeroacoustics Conference & Exhibit, Breckenridge, Colorado. https://doi.org/10.2514/6.2004-1028.

EPA. 2020. "Sound Emission Standards and Limitations for Property Line Noise Sources." https://pcb.illinois.gov/documents/dsweb/Get/Document-12261/.

Etter, Robert B. 2007. "CFD Investigation of Effect of Depth to Diameter Ratio on Dimple Flow // Computational fluid dynamics investigation of effect of depth to diameter ratio on dimple flow dynamics." Master's Thesis, Department of Aeronautics and Astronautics, Air Force Institute of Technology. https://scholar.afit.edu/etd/2938/.

FAA. 2023. "Noise Standards: Aircraft Type and Airworthiness Certification." https://www.ecfr.gov/current/title-14/chapter-I/subchapter-C/part-36.

Fatahian, Esmaeel, Ali Lohrasbi Nichkoohi, Hesamoddin Salarian, and Jahanfar Khaleghinia. 2020. "Effects of the hinge position and suction on flow separation and aerodynamic performance of the NACA

0012 airfoil." *Journal of the Brazilian Society of Mechanical Sciences and Engineering* 42 (2). https://doi.org/10.1007/s40430-020-2170-4.

Fink, M., and D. Bailey. 1980. "Model tests of airframe noise reduction concepts." 6th Aeroacoustics Conference, Hartford, CT. https://doi.org/10.2514/6.1980-979.

Fouatih, Omar Madani, Marc Medale, Omar Imine, and Bachir Imine. 2016. "Design optimization of the aerodynamic passive flow control on NACA 4415 airfoil using vortex generators." *European Journal of Mechanics - B/Fluids* 56: 82-96. https://doi.org/10.1016/j.euromechflu.2015.11.006.

Fu, Jinbin, and Luigi Vigevano. 2022. "Aeroacoustic modeling of helicopter transonic rotor noise." *Aerospace Science and Technology* 122. https://doi.org/10.1016/j.ast.2022.107430.

Gang, Li, Zhang Zhengtao, and Zou Pingguo. 2019. "Numerical study on noise reduction of wind turbine blade vortex generator." IOP Conference Series: Earth and Environmental Science, Bristol, England. https://doi.org/10.1088/1755-1315/358/2/022026.

Gersten, K. 1985. "The turbulent Couette flow from asymptotic theory viewpoint." Flow of Real Fluids, Berlin, Germany. https://doi.org/10.1007/3-540-15989-4_86.

Geyer, Thomas F., and Danielle J. Moreau. 2021. "A study of the effect of airfoil thickness on the tonal noise generation of finite, wall-mounted airfoils." *Aerospace Science and Technology* 115. https://doi.org/10.1016/j.ast.2021.106768.

Hattori, H., T. Umehara, and Y. Nagano. 2013. "Comparative Study of DNS, LES and Hybrid LES/RANS of Turbulent Boundary Layer with Heat Transfer Over 2d Hill." *Flow, Turbulence and Combustion* 90 (3): 491-510. https://doi.org/10.1007/s10494-013-9450-3.

Heine, B., K. Mulleners, A. Gardner, and H. Mai. 2009. "On the effects of leading edge vortex generators on an OA209 airfoil." ONERA-DLR Aerospace Symposium. https://core.ac.uk/download/pdf/11138215.pdf.

Huang, L., P. G. Huang, R. P. LeBeau, and T. Hauser. 2004. "Numerical Study of Blowing and Suction Control Mechanism on NACA0012 Airfoil." *Journal of Aircraft* 41 (5): 1005-1013. https://doi.org/10.2514/1.2255.

Jacobs, Eastman N., and Albert Sherman. 1939. "Airfoil Section Charecteristics as Affected by Variaitions of the Reynolds Number." https://ntrs.nasa.gov/citations/19930091662.

Jahanmiri, Mohsenn. 2010. *Active Flow Control: A Review.* Chalmers Univeristy of Technology (Göteborg, Sweden). https://publications.lib.chalmers.se/records/fulltext/local_131464.pdf.

Kight, C. R., and J. P. Swaddle. 2011. "How and why environmental noise impacts animals: an integrative, mechanistic review." *Ecol Lett* 14 (10): 1052-61. https://doi.org/10.1111/j.1461-0248.2011.01664.x.

Kiknadze, G. I., A. Gachechiladze, V. G. Oleinikov, and V. V. Alekseev. 2006. "Mechanisms of the Self-Organization of Tornado-Like Jets Flowing Past Three-Dimensional Concave Reliefs." *Heat Transfer Research* https://doi.org/10.1615/HeatTransRes.v37.i6.10.

Klei, Christine E., Rainer M. Buffo, and Eike Stumf. 2014. "Effects of Wing Tip Shaping on Noise Generation." International Congress on Noise Control Engineering, Aachen, Germany. https://acoustics.asn.au/conference_proceedings/INTERNOISE2014/papers/p283.pdf.

Kolkman, Dennis, Leandro D. de Santana, Cornelis H. Venner, Arne v Garrel, Carlos Arce León, and Martinus P. Sanders. 2018. "Experimental Characterization of Vortex Generators Induced Noise of Wind Turbines." 2018 AIAA/CEAS Aeroacoustics Conference. https://doi.org/10.2514/6.2018-2800.

Lee, Seongkyu, Lorna Ayton, Franck Bertagnolio, Stephane Moreau, Tze Pei Chong, and Phillip Joseph. 2021. "Turbulent boundary layer trailing-edge noise: Theory, computation, experiment, and application." *Progress in Aerospace Sciences* 126. https://doi.org/10.1016/j.paerosci.2021.100737.

Li, Zhiyong, Tingting Tang, Yu Liu, Elias J. G. Arcondoulis, and Yannian Yang. 2020. "Numerical study of aerodynamic and aeroacoustic characteristics of flow over porous coated cylinders: Effects of porous properties." *Aerospace Science and Technology* 105. https://doi.org/10.1016/j.ast.2020.106042.

Lienhart, Hermann, Michael Breuer, and Cagatay Köksoy. 2008. "Drag reduction by dimples? – A complementary experimental/numerical investigation." *International Journal of Heat and Fluid Flow* 29 (3): 783-791. https://doi.org/10.1016/j.ijheatfluidflow.2008.02.001.

Liu, Jing, and Jie Li. 2014. "Numerical Prediction of Flow Structure and Heat Enhancement with Different Dimple Depth." *Applied Mechanics and Materials* 574: 147-153. https://doi.org/10.4028/www.scientific.net/AMM.574.147.

Lowson, Martin V., Steven P. Fiddes, and Emma C. Nash. 1994. "Laminar Boundary Layer Aeroacoustic Instabilities." 32nd Aerospace Sciences Meeting & Exhibit, Reno, NV. https://doi.org/10.2514/6.1994-358.

Lu, Frank, Qin Li, Yusi Shih, Adam Pierce, and Chaoqun Liu. 2011. "Review of Micro Vortex Generators in High-Speed Flow." 49th AIAA Aerospace Sciences Meeting including the New Horizons Forum and Aerospace Exposition, Orlando, FL. https://doi.org/10.2514/6.2011-31.

Mai, Holger, Guido Dietz, Wolfgang Geißler, Kai Richter, Johannes Bosbach, Hugues Richard, and Klaus de Groot. 2008. "Dynamic Stall Control by Leading Edge Vortex Generators." *Journal of the American Helicopter Society* 53 (1). https://doi.org/10.4050/jahs.53.26.

Manolesos, M., G. Papadakis, and S. G. Voutsinas. 2020. "Revisiting the assumptions and implementation details of the BAY model for vortex generator flows." *Renewable Energy* 146: 1249-1261. https://doi.org/10.1016/j.renene.2019.07.063.

Mathias, Donovan, John Pye, and Brian Cantwell. 1998. "Correlation of wingtip noise with mean flow parameters." 16th AIAA Applied Aerodynamics Conference, Albuquerque, NM. https://doi.org/10.2514/6.1998-2738.

Mayer, Yannick D., Benshuai Lyu, Hasan Kamliya Jawahar, and Mahdi Azarpeyvand. 2019. "A semi-analytical noise prediction model for airfoils with serrated trailing edges." *Renewable Energy* 143: 679-691. https://doi.org/10.1016/j.renene.2019.04.132.

Menter, F. R. 1994. "Two-equation eddy-viscosity turbulence models for engineering applications." *AIAA Journal* 32 (8): 1598-1605. https://doi.org/10.2514/3.12149.

Michel, U., D. Eschricht, B. Greschner, T. Knacke, C. Mockett, and F. Thiele. 2009. "Advanced DES Methods and Their Application to Aeroacoustics " Notes on Numerical Fluid Mechanics and Multidisciplinary Design, Gdansk, Poland. https://doi.org/10.1007/978-3-642-14168-3_5.

Moghaddam, Tohid, and Nafiseh Banazadeh Neishabouri. 2017. "On the Active and Passive Flow Separation Control Techniques over Airfoils." IOP Conf. Series: Materials Science and Engineering https://doi.org/10.1088/1757-899X/248/1/012009.

Moreau, Danielle, Thomas Geyer, Con J. Doolan, and Ennes Sarradj. 2017. "Camber Effects on the Tonal Noise and Flow Characteristics of a Wall-mounted Finite Airfoil." 23rd AIAA/CEAS Aeroacoustics Conference, Denver, CO. https://doi.org/10.2514/6.2017-3172.

Moreau, Danielle J., and Con J. Doolan. 2016. "Tonal noise production from a wall-mounted finite airfoil." *Journal of Sound and Vibration* 363: 199-224. https://doi.org/10.1016/j.jsv.2015.11.021.

Moreau, Danielle J., Zebb Prime, Ric Porteous, Con J. Doolan, and Vincent Valeau. 2014. "Flow-induced noise of a wall-mounted finite airfoil at low-to-moderate Reynolds number." *Journal of Sound and Vibration* 333 (25): 6924-6941. https://doi.org/10.1016/j.jsv.2014.08.005.

Murayama, Mitsuhiro, Kazuomi Yamamoto, Takehisa Takaishi, Yasushi Ito, Hiroki Ura, Yuzuru Yokokawa, Kentaro Tanaka, and Tohru Hirai. 2017. "Airframe Noise Reduction of Flap Side-edge Using Vortex

Generators." 23rd AIAA/CEAS Aeroacoustics Conference, Denver, CO. https://doi.org/10.2514/6.2017-4030.

Nagy, Attila Balázs, Jan Delfs, and Gareth J. Bennett. 2022. "Aeroacoustics research in Europe: The CEAS-ASC report on 2020 & 2021 highlights." *Journal of Sound and Vibration* 534. https://doi.org/10.1016/j.jsv.2022.117002.

Nash, Emma C., Martin V. Lowso, and Alan McAlpine. 1999. "Boundary-layer instability noise on aerofoils." *Journal of Fluid Mechanics*. https://doi.org/10.1017/S002211209800367X.

Neves, A. F., N. J. Lawson, C. J. Bennett, B. Khanal, and R. I. Hoff. 2020. "Unsteady aerodynamics analysis and modelling of a Slingsby Firefly aircraft: Detached-Eddy Simulation model and flight test validation." *Aerospace Science and Technology* 106. https://doi.org/10.1016/j.ast.2020.106179.

Oerlemans, Stefan, Murray Fisher, Thierry Maeder, and Klaus Kögler. 2009. "Reduction of Wind Turbine Noise Using Optimized Airfoils and Trailing-Edge Serrations." *AIAA Journal* 47 (6): 1470-1481. https://doi.org/10.2514/1.38888.

Panaras, Argyris G., and Frank K. Lu. 2015. "Micro-vortex generators for shock wave/boundary layer interactions." *Progress in Aerospace Sciences* 74: 16-47. https://doi.org/10.1016/j.paerosci.2014.12.006.

Panda, J. P., and Hari Vijayan Warrior. 2021. "Mechanics of drag reduction of an axisymmetric body of revolution with shallow dimples." https://doi.org/10.13140/RG.2.2.16763.03361.

Pascioni, Kyle A., and Louis N. Cattafesta. 2014. "An Experimental Investigation of the 30P30N Multi-Element High-Lift Airfoil." 20th AIAA/CEAS Aeroacoustics Conference, Atlanta, GA. https://doi.org/10.2514/6.2014-3062.

Paterson, Robert W., Paul G. Vogt, Martin R. Fink, and C. Lee Munch. 1973. "Vortex Noise of Isolated Airfoils." *Journal of Aircraft* 10 (5): 296-302. https://doi.org/10.2514/3.60229.

Perry, M.L., and T.J. Mueller. 1986. "The Influence of Leading and Trailing Edge Flaps on the Performance of a Low Reynolds Number Airfoil." 4th Applied Aerodynamics Conference, San Diego, CA. https://doi.org/10.2514/6.1986-1787.

---. 1987. "Leading- and trailing-edge flaps on a low Reynolds number airfoil." *Journal of Aircraft* 24 (9): 653-659. https://doi.org/10.2514/3.45491.

Powell, Allan. 1964. "Theory of Vortex Sound." *The Journal of the Acoustical Society of America* 36. https://doi.org/10.1121/1.1918931.

Prandtl, Ludwig. 1928. *Motion of Fluids with Very Little Viscosity.* (University of North Texas Libraries: National Advisory Committee for Aeronautics). https://ntrs.nasa.gov/citations/19930090813.

Pröbsting, S., J. Serpieri, and F. Scarano. 2014. "Experimental investigation of aerofoil tonal noise generation." *Journal of Fluid Mechanics* 747: 656-687. https://doi.org/10.1017/jfm.2014.156.

Ramprasadh, C., and V. Devanandh. 2015. "A CFD Study on Leading Edge Wing Surface Modification of a Low Aspect Ratio Flying Wing to Improve Lift Performance." *International Journal of Micro Air Vehicles* 7 (3): 361-373. https://doi.org/10.1260/1756-8293.7.3.361.

Reed, Helen L. 1981. "The Tollmien-Schlichting Instability of Laminar Viscous Flows." PhD diss., Engineering Mechanics, Virginia Polytechnic Institute and State University. https://vtechworks.lib.vt.edu/bitstream/handle/10919/74834/LD5655.V856_1981.R443.pdf?sequence=1&isAllowed=y.

Rooks, Jaap. 2016. "Computational aeroacoustic analysis of trailing edge noise: A Direct Numerical Simulation using the Lattice Boltzmann Method." Master's thesis, Delft University of Technology. https://repository.tudelft.nl/islandora/object/uuid:d64b13d7-5473-4063-80c7-e5c49b8c3d04/datastream/OBJ/download.

Rubio Carpio, Alejandro, Roberto Merino Martínez, Francesco Avallone, Daniele Ragni, Mirjam Snellen, and Sybrand van der Zwaag. 2019. "Experimental characterization of the turbulent boundary layer

over a porous trailing edge for noise abatement." *Journal of Sound and Vibration* 443: 537-558. https://doi.org/10.1016/j.jsv.2018.12.010.

Schumacher, Karn L., Con J. Doolan, and Richard M. Kelso. 2014. "The effect of a cavity on airfoil tones." *Journal of Sound and Vibration* 333 (7): 1913-1931. https://doi.org/10.1016/j.jsv.2013.11.046.

Serdar GenÇ, Mustafa, Kemal Koca, and Halil Hakan AÇIkel. 2019. "Investigation of pre-stall flow control on wind turbine blade airfoil using roughness element." *Energy* 176: 320-334. https://doi.org/10.1016/j.energy.2019.03.179.

Serdar Genç, Mustafa, Kemal Koca, Hacımurat Demir, and Halil Hakan Açıkel. 2020. "Traditional and New Types of Passive Flow Control Techniques to Pave the Way for High Maneuverability and Low Structural Weight for UAVs and MAVs." *Autonomous Vehicles*. https://doi.org/10.5772/intechopen.90552.

Silvani, Matteo Paolo. 2021. "Dimples as a drag reduction technique: a preliminary DNS approach." Master's Thesis, Politecnico di Milano. https://home.aero.polimi.it/quadrio/it/Tesi/silvani/tesi-silvani.pdf.

Simon, Bernhard Jochen. 2017. "Active Cancellation of Tollmien-Schlichting Waves under Varying Inflow Conditions for In-Flight Application." Ph.D Dis., Fachschaft Maschinenbau TU Darmstadt. https://tuprints.ulb.tu-darmstadt.de/id/eprint/6161.

Soundharya, V, Anil B A, Venu Gopal S, and Gowreesh S S. 2016. "Aerodynamic Analysis of Dimple effect on Airfoil." *International Journal of Engineering and Advanced Technology*. https://www.ijeat.org/wp-content/uploads/papers/v5i4/D4544045416.pdf.

Spalart, P. R., M. Shur, M. Strelets, A. Travin, K. B. Paschal, and S. P. Wilkinson. 2019. "Experimental and numerical study of the turbulent boundary layer over shallow dimples." *International Journal of Heat and Fluid Flow* 78. https://doi.org/10.1016/j.ijheatfluidflow.2019.108438.

Spalart, P.R., M.L. Shur, M.Kh. Strelets, and A.K. Travin. 2015. "Direct Simulation and RANS Modelling of a Vortex Generator Flow." *Flow, Turbulence and Combustion* 95. https://doi.org/10.1007/s10494-015-9610-8.

Tam, Christopher K. W. 1974. "Discrete tones of isolated airfoils." *Acoustical Society of America* 55. https://doi.org/10.1121/1.1914682.

Tay, C. M. 2011. "Determining the Effect of Dimples on Drag in a Turbulent Channel Flow." 49th AIAA Aerospace Sciences Meeting, Orlando, FL. https://doi.org/10.2514/6.2011-682.

Tay, C. M. J., B. C. Khoo, and Y. T. Chew. 2015. "Mechanics of drag reduction by shallow dimples in channel flow." *Physics of Fluids* 27 (3). https://doi.org/10.1063/1.4915069.

Tousi, N. M., J. M. Bergadà, and F. Mellibovsky. 2022. "Large Eddy Simulation of optimal Synthetic Jet Actuation on a SD7003 airfoil in post-stall conditions." *Aerospace Science and Technology* 127. https://doi.org/10.1016/j.ast.2022.107679.

Tousi, N. M., M. Coma, J. M. Bergadà, J. Pons-Prats, F. Mellibovsky, and G. Bugeda. 2021. "Active flow control optimisation on SD7003 airfoil at pre and post-stall angles of attack using synthetic jets." *Applied Mathematical Modelling* 98: 435-464. https://doi.org/10.1016/j.apm.2021.05.016.

van Campenhout, Olaf W., Michiel van Nesselrooij, Leo L. Veldhuis, Bas van Oudheusden, and Ferry Schrijer. 2018. "An experimental investigation into the flow mechanics of dimpled surfaces in turbulent boundary layers." 2018 AIAA Aerospace Sciences Meeting, Kissimmee, FL. https://doi.org/10.2514/6.2018-2062.

van Nesselrooij, M., L. L. M. Veldhuis, B. W. van Oudheusden, and F. F. J. Schrijer. 2016. "Drag reduction by means of dimpled surfaces in turbulent boundary layers." *Experiments in Fluids* 57 (9). https://doi.org/10.1007/s00348-016-2230-9.

Veldhuis, L.L.M., and E. Vervoort. 2009. "Drag Effect of a Dented Surface in a Turbulent Flow." 27th AIAA Applied Aerodynamics Conference, San Antonio, TX. http://doi.org/10.2514/6.2009-3950.

Weigand, B., and V. Simon. 2006. "Laws of similarity in fluid mechanics." *WIT Transactions on State of the Art in Science and Engineering*: 20-35. https://www.witpress.com/Secure/elibrary/papers/1845640012/1845640012102FU1.pdf.

Xie, Yin, Yu Rao, Yuli Cheng, and Wei Tian. 2022. "Investigation into the laminar separation control of airfoils at low Reynolds numbers by dimple vortex generators." *Aerospace Science and Technology* 129. https://doi.org/10.1016/j.ast.2022.107841.

Yakeno, Aiko, Yosuke Hasegawa, and Nobuhide Kasagi. 2014. "Modification of quasi-streamwise vortical structure in a drag-reduced turbulent channel flow with spanwise wall oscillation." *Physics of Fluids* 26 (8). https://doi.org/10.1063/1.4893903.

Ye, Qingqing, Francesco Avallone, Wouter van der Velden, and Damiano Casalino. 2020. "Effect of Vortex Generators on NREL Wind Turbine: Aerodynamic Performance and Far-Field Noise." *Journal of Physics: Conference Series* 1618. https://doi.org/10.1088/1742-6596/1618/5/052077.

Yousefi, Kianoosh, Reza Saleh, and Peyman Zahedi. 2014. "Numerical study of blowing and suction slot geometry optimization on NACA 0012 airfoil." *Journal of Mechanical Science and Technology* 28 (4): 1297-1310. https://doi.org/10.1007/s12206-014-0119-1.

Zhong, Siyang, Xin Zhang, and Xun Huang. 2019. "A comparison of acoustic far-field prediction methods for turbulent flows." *International Journal of Aeroacoustics* 18 (6-7): 579-595. https://doi.org/10.1177/1475472x19871525.

Zhu, Chengyong, Jie Chen, Yingning Qiu, and Tongguang Wang. 2021. "Numerical investigation into rotational augmentation with passive vortex generators on the NREL Phase VI blade." *Energy* 223. https://doi.org/10.1016/j.energy.2021.120089.

Zhu, Chengyong, Jie Chen, Jianghai Wu, and Tongguang Wang. 2019. "Dynamic stall control of the wind turbine airfoil via single-row and double-row passive vortex generators." *Energy* 189. https://doi.org/10.1016/j.energy.2019.116272.

Zhu, Chengyong, Yingning Qiu, Yanhui Feng, Tongguang Wang, and Hui Li. 2022. "Combined effect of passive vortex generators and leading-edge roughness on dynamic stall of the wind turbine airfoil." *Energy Conversion and Management* 251. https://doi.org/10.1016/j.enconman.2021.115015.

APPENDIX

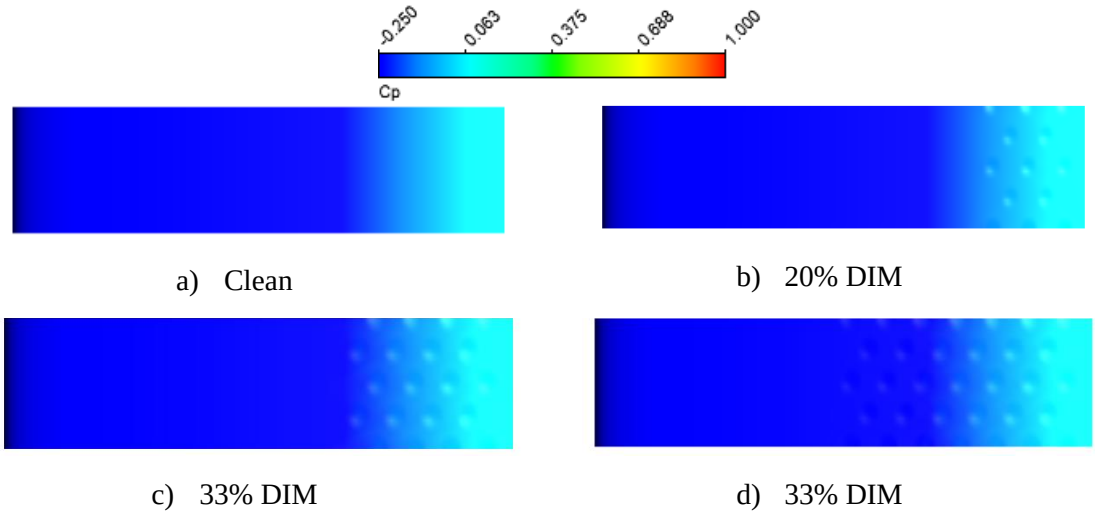

a) Clean b) 20% DIM

c) 33% DIM d) 33% DIM

Figure 5.1.1: Pressure Coefficient on Airfoil Surface at an AoA = 6° on a) Clean b) 20% DIM c) 33% DIM and d) 50% DIM Arrays

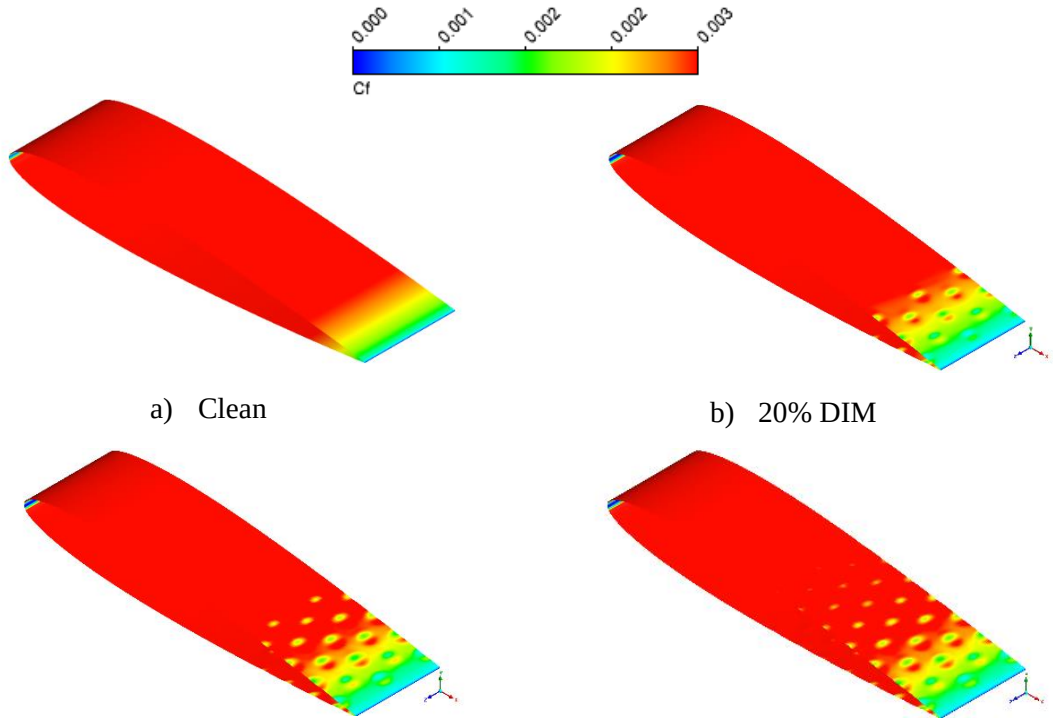

a) Clean b) 20% DIM

c) 33% DIM d) 50% DIM

Figure 5.1.2: Skin Friction on Airfoil Surface at an AoA = 3° on a) Clean b) 20% DIM c) 33% DIM and d) 50% DIM Arrays

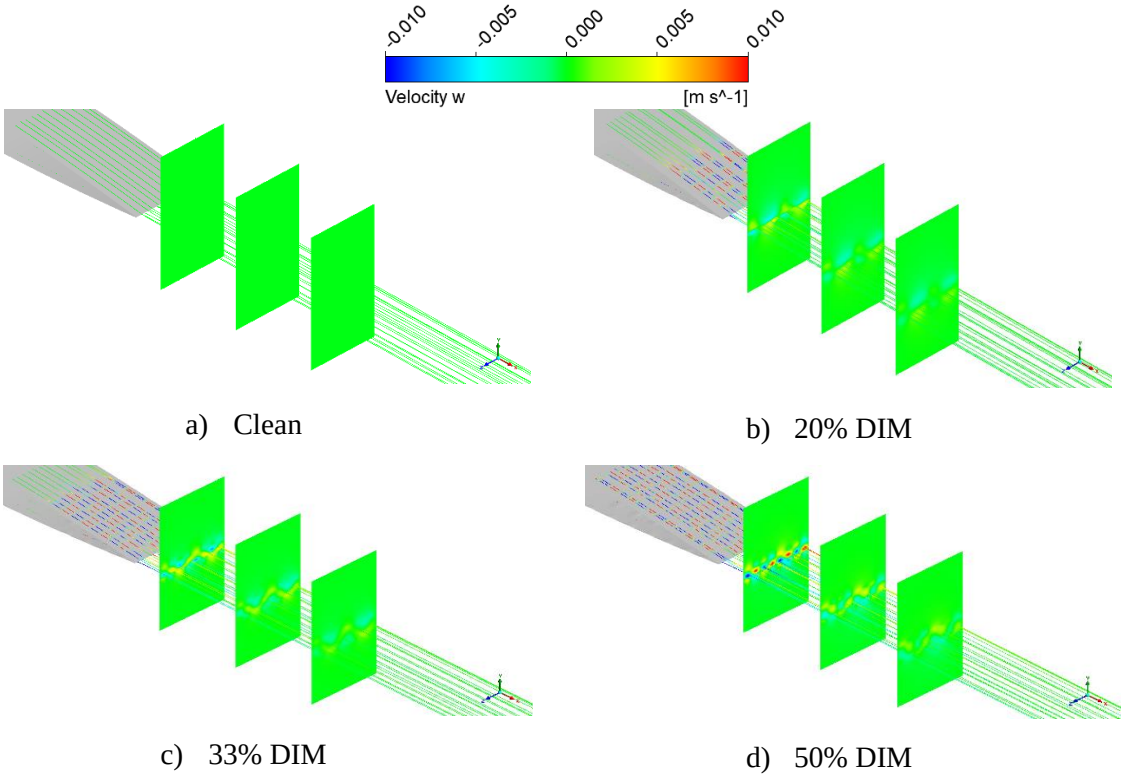

a) Clean

b) 20% DIM

c) 33% DIM

d) 50% DIM

Figure 5.1.3: Spanwise Velocity Streamlines at an AoA = 3° on a) Clean b) 20% DIM c) 33% DIM and d) 50% DIM Arrays

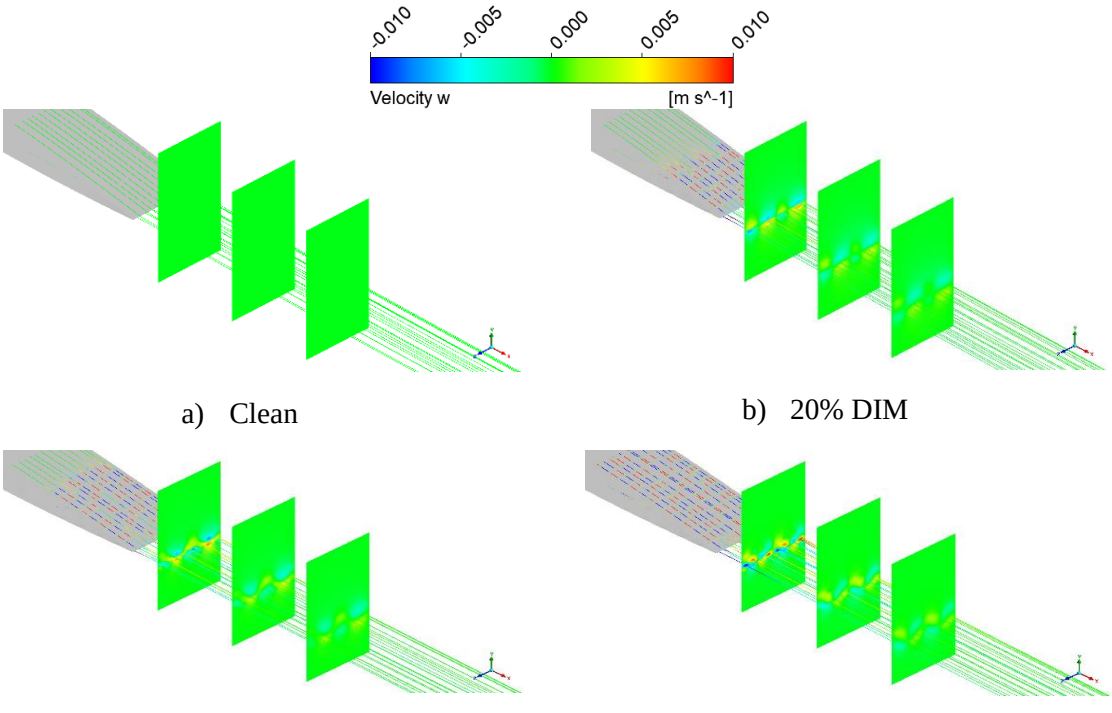

a) Clean

b) 20% DIM

c) 33% DIM

d) 50% DIM

Figure 5.1.4: Spanwise Velocity Streamlines at an AoA = 6° on a) Clean b) 20% DIM c) 33% DIM and d) 50% DIM Arrays

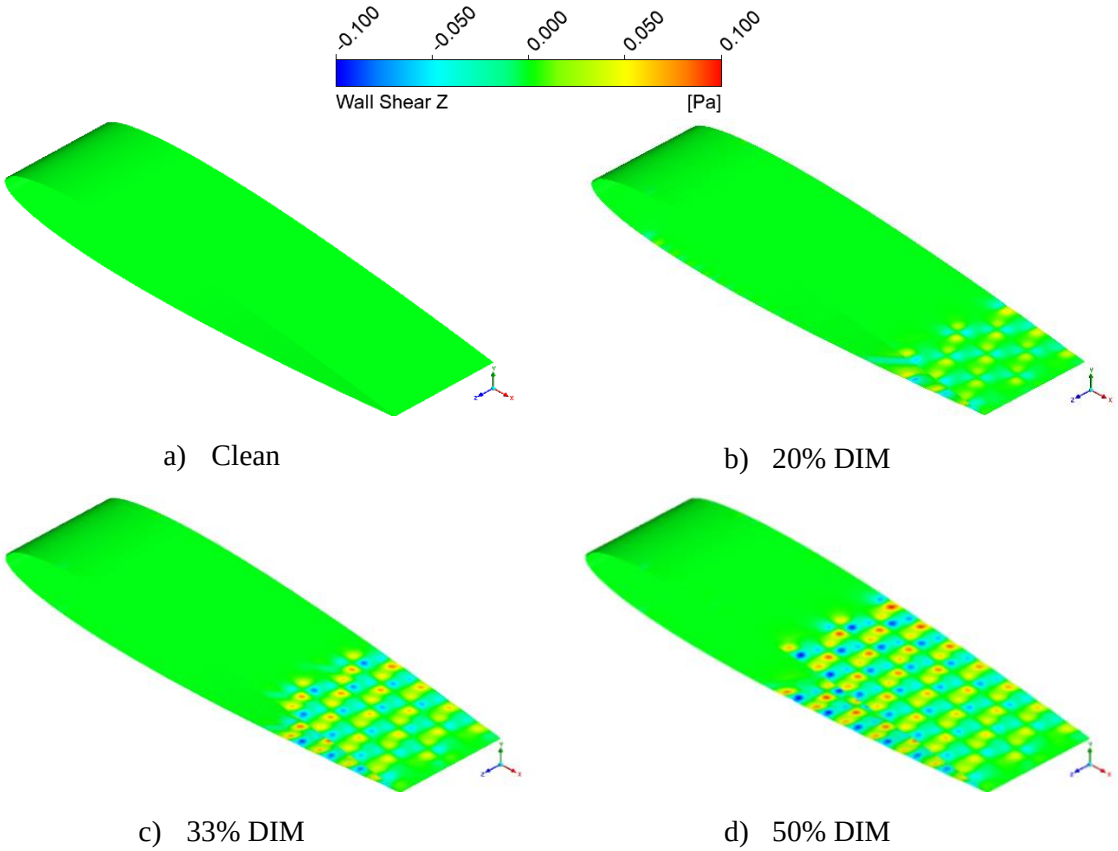

a) Clean

b) 20% DIM

c) 33% DIM

d) 50% DIM

Figure 5.1.5: Wall Shear z on Airfoil Surface at an AoA= 3° on a) Clean b) 20% DIM c) 33% DIM and d) 50% DIM Arrays

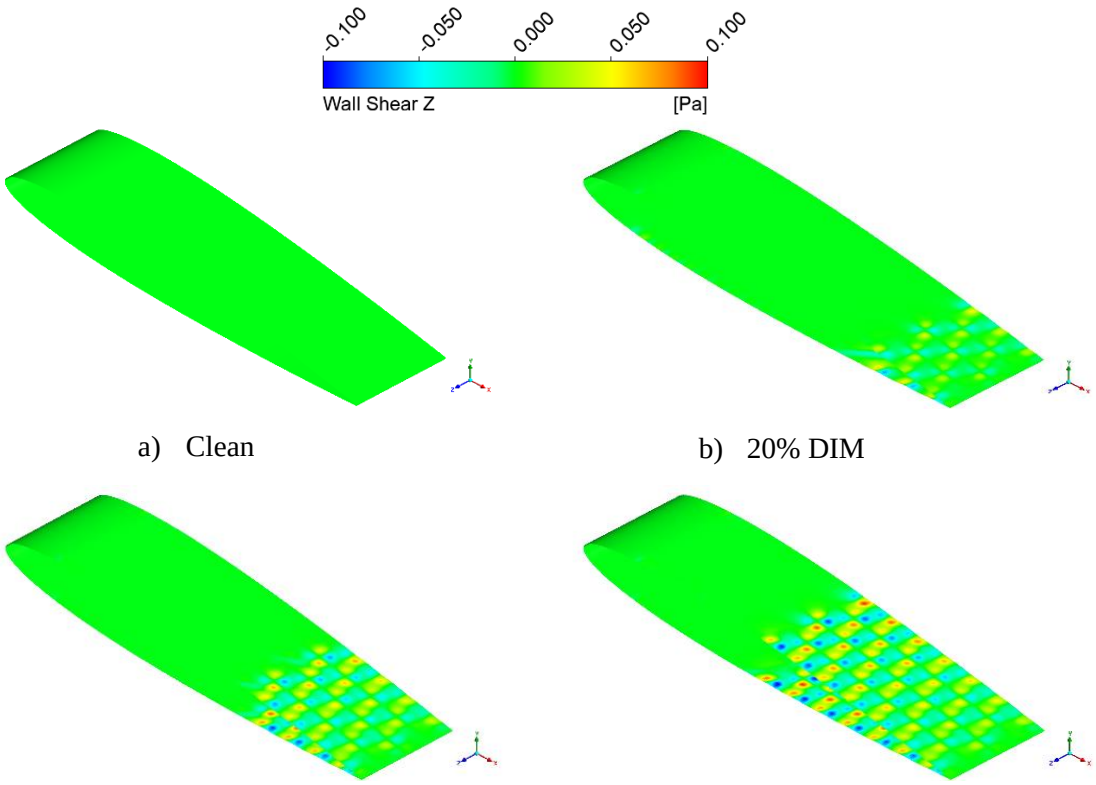

a) Clean

b) 20% DIM

c) 33% DIM

d) 50% DIM

Figure 5.1.6: Wall Shear on Airfoil Surface at 6° on a) Clean b) 20% DIM c) 33% DIM and d) 50% DIM Arrays